

# Argonne National Laboratory

## REACTOR DEVELOPMENT PROGRAM PROGRESS REPORT

February 1970

The facilities of Argonne National Laboratory are owned by the United States Government. Under the terms of a contract (W-31-109-Eng-38) between the U. S. Atomic Energy Commission, Argonne Universities Association and The University of Chicago, the University employs the staff and operates the Laboratory in accordance with policies and programs formulated, approved and reviewed by the Association.

#### MEMBERS OF ARGONNE UNIVERSITIES ASSOCIATION

The University of Arizona  
Carnegie-Mellon University  
Case Western Reserve University  
The University of Chicago  
University of Cincinnati  
Illinois Institute of Technology  
University of Illinois  
Indiana University  
Iowa State University  
The University of Iowa

Kansas State University  
The University of Kansas  
Loyola University  
Marquette University  
Michigan State University  
The University of Michigan  
University of Minnesota  
University of Missouri  
Northwestern University  
University of Notre Dame

The Ohio State University  
Ohio University  
The Pennsylvania State University  
Purdue University  
Saint Louis University  
Southern Illinois University  
University of Texas  
Washington University  
Wayne State University  
The University of Wisconsin

#### LEGAL NOTICE

This report was prepared as an account of Government sponsored work. Neither the United States, nor the Commission, nor any person acting on behalf of the Commission:

A. Makes any warranty or representation, expressed or implied, with respect to the accuracy, completeness, or usefulness of the information contained in this report, or that the use of any information, apparatus, method, or process disclosed in this report may not infringe privately owned rights; or

B. Assumes any liabilities with respect to the use of, or for damages resulting from the use of any information, apparatus, method, or process disclosed in this report.

As used in the above, "person acting on behalf of the Commission" includes any employee or contractor of the Commission, or employee of such contractor, to the extent that such employee or contractor of the Commission, or employee of such contractor prepares, disseminates, or provides access to, any information pursuant to his employment or contract with the Commission, or his employment with such contractor.

Printed in the United States of America

Available from

Clearinghouse for Federal Scientific and Technical Information  
National Bureau of Standards, U. S. Department of Commerce  
Springfield, Virginia 22151

Price: Printed Copy \$3.00; Microfiche \$0.65



ARGONNE NATIONAL LABORATORY  
9700 South Cass Avenue  
Argonne, Illinois 60439

REACTOR DEVELOPMENT PROGRAM  
PROGRESS REPORT

February 1970

Robert B. Duffield, Laboratory Director  
Alfred Amorosi, Assistant Laboratory Director

Division

Director

|                             |               |
|-----------------------------|---------------|
| Applied Physics             | R. Avery      |
| Chemical Engineering        | R. C. Vogel   |
| EBR-II Project              | M. Levenson   |
| Engineering and Technology  | S. A. Davis   |
| Materials Science           | P. G. Shewmon |
| Reactor Analysis and Safety | W. R. Simmons |

Report coordinated by  
A. Glassner and V. G. Trice, Jr.

Issued March 30, 1970

## FOREWORD

The Reactor Development Program Progress Report, issued monthly, is intended to be a means of reporting those items of significant technical progress which have occurred in both the specific reactor projects and the general engineering research and development programs. The report is organized in accordance with budget activities in a way which, it is hoped, gives the clearest, most logical overall view of progress. Since the intent is to report only items of significant progress, not all activities are reported each month. In order to issue this report as soon as possible after the end of the month editorial work must necessarily be limited. Also, since this is an informal progress report, the results and data presented should be understood to be preliminary and subject to change unless otherwise stated.

The issuance of these reports is not intended to constitute publication in any sense of the word. Final results either will be submitted for publication in regular professional journals or will be published in the form of ANL topical reports.

The last six reports issued  
in this series are:

|                |          |
|----------------|----------|
| August 1969    | ANL-7606 |
| September 1969 | ANL-7618 |
| October 1969   | ANL-7632 |
| November 1969  | ANL-7640 |
| December 1969  | ANL-7655 |
| January 1970   | ANL-7661 |

## REACTOR DEVELOPMENT PROGRAM

### Highlights of Project Activities for February 1970

#### EBR-II

The reactor was operated for 1334 MWd between January 21 and February 20, inclusive, bringing its cumulative operational total to 32,361 MWd.

Of the 12 samples of different metals in materials-surveillance subassembly SURV-2, only beryllium copper and tantalum lost appreciable weight during irradiation exposure to sodium in EBR-II. The densities of tantalum, T-1 tool steel, and Type 304 stainless steel apparently were reduced during exposure.

#### ZPR-3

Calculation of the relative U-238 capture rates in a central unit cell of Assembly 54 has been completed and is in fair agreement with measurements.

The integral capture-to-fission ratio of Pu-239 obtained at the center of Assembly 57 in a high-intensity irradiation has been found to be  $0.363 \pm 0.024$ .

The central fast-neutron-spectrum data from Assembly 58 has been analyzed. Analysis of experiments in Assembly 59 has been completed.

Assembly 60, a U-235 version of a homogenized 91-element EBR-II loading with asymmetric top and bottom axial reflectors, has been made critical and measurements begun.

#### ZPR-6

The experiments with the 4000-liter U-235 core, Assembly 6A, have been completed, and the data are being analyzed. Measurements made include: the central reactivity worths of a number of materials in a sodium-bearing and sodium-free environment, the radial and axial variation of sodium-void coefficient, capture and fission rates in U-238 and U-235 at various locations, and material buckling. The critical mass of this assembly was 1798 kg.

## ZPR-9

The reflector of the FTR-3 core, Assembly 26, was modified by removing nickel from the earlier reflector loading and adding a peripheral zone of stainless steel and sodium. The neutron spectrum in this new reference configuration has been measured, and all control and safety rods have been calibrated.

## ZPPR

The radial variation of the rates of B-10 capture, U-238 fission, Pu-239 fission, and Na-23 capture have been calculated for ZPPR/FTR-2 with and without fuel stored in the shield. Qualitative agreement between calculated and experimental data was generally satisfactory.

Fuel loading for the 2600-liter demonstration-plant critical assembly, ZPPR Assembly 2, has begun, and the automatic control system for the ZPPR Doppler measurements has been checked out.

# TABLE OF CONTENTS

|   | <u>Page</u> |
|---|-------------|
| I. LIQUID METAL FAST BREEDER REACTORS--CIVILIAN       | 1           |
| A. Physics Development--LMFBR                         | 1           |
| 1. Theoretical Reactor Physics                        | 1           |
| 2. Experimental Reactor Physics                       | 16          |
| 3. ZPR-6 and -9 Operations and Analysis               | 26          |
| 4. ZPR-3 and ZPPR Operations and Analysis             | 30          |
| B. Component Development--LMFBR                       | 40          |
| 1. Instrumentation and Control                        | 40          |
| 2. Fuel Handling, Vessels, and Internals              | 46          |
| C. Sodium Technology                                  | 47          |
| 1. Purification of Sodium                             | 47          |
| 2. On-line Monitors                                   | 48          |
| 3. Sampling   | 49          |
| 4. Fission Product Behavior and Control               | 50          |
| D. EBR-II--Research and Development                   | 51          |
| 1. Equipment--Fuel Related                            | 51          |
| 2. New Subassemblies and Experimental Support         | 51          |
| 3. Instrumented Subassemblies                         | 53          |
| 4. Coolant Chemistry                                  | 57          |
| 5. Experimental Irradiation and Testing               | 58          |
| 6. Materials-Coolant Compatibility                    | 60          |
| 7. Reactor Analysis, Testing, and Methods Development | 66          |
| 8. Driver Fuel Development                            | 86          |
| 9. Operation with Failed Fuel                         | 89          |
| 10. Physics Mock-up Studies                           | 91          |
| E. EBR-II--Fuel Fabrication                           | 92          |
| 1. Cold Line Operations                               | 92          |
| F. EBR-II--Operations                                 | 93          |
| 1. Reactor Plant                                      | 93          |
| 2. Fuel Cycle Facility                                | 94          |
| PUBLICATIONS  | 97          |

## TABLE OF CONTENTS

|  | <u>Page</u> |
|--|-------------|
| II. OTHER FAST REACTORS--OTHER FAST BREEDER<br>REACTORS--FUEL DEVELOPMENT                    | 98          |
| A. Irradiation Effects, Mechanical Properties, and<br>Fabrication                            | 98          |
| 1. Swelling in the Dimple Region of Subassembly XA08   | 98          |
| 2. Mechanical Properties of Cladding Materials   | 99          |
| 3. Surface Defects as Failure Sites in Type 304<br>Seamless Stainless Steel Fuel-clad Tubing | 99          |
| III. GENERAL REACTOR TECHNOLOGY  | 101         |
| A. Applied and Reactor Physics Development   | 101         |
| 1. Theoretical Reactor Physics--Research and<br>Development                                  | 101         |
| B. Reactor Fuels and Materials Development   | 105         |
| 1. Fuels and Claddings--Research and Development   | 105         |
| 2. Radiation Damage on Structural Materials--<br>Research and Development                    | 115         |
| 3. Techniques of Fabrication and Testing--Research<br>and Development                        | 116         |
| 4. Engineering Properties of Reactor Materials--<br>Research and Development                 | 120         |
| C. Engineering Development--Research and Development   | 123         |
| 1. Instrumentation and Control   | 123         |
| 2. Heat Transfer and Fluid Flow  | 126         |
| 3. Engineering Mechanics   | 127         |
| D. Chemistry and Chemical Separations  | 130         |
| 1. Fuel Cycle Technology--Research and Development   | 130         |
| 2. General Chemistry and Chemical Engineering--<br>Research and Development                  | 133         |
| PUBLICATIONS   | 136         |

## TABLE OF CONTENTS

|  | <u>Page</u> |
|--|-------------|
| IV. NUCLEAR SAFETY RESEARCH AND DEVELOPMENT  | 137         |
| A. LMFBR Safety--Research and Development  | 137         |
| 1. Reactor Control and Stability   | 137         |
| 2. Coolant Dynamics  | 138         |
| 3. Violent Boiling   | 140         |
| B. Engineered Safety Features--Safety Features Technology--<br>Research and Development--Containment | 141         |
| 1. Hydrodynamic Response to High-Energy Excursion  | 141         |
| PUBLICATION  | 143         |



# TABLE OF CONTENTS

|     |                            |
|-----|----------------------------|
| 1   | INTRODUCTION               |
| 2   | 1. PURPOSE AND SCOPE       |
| 3   | 2. REFERENCES              |
| 4   | 3. DEFINITIONS             |
| 5   | 4. SCOPE OF THE STUDY      |
| 6   | 5. LIMITATIONS             |
| 7   | 6. SUMMARY OF FINDINGS     |
| 8   | 7. CONCLUSIONS             |
| 9   | 8. RECOMMENDATIONS         |
| 10  | 9. APPENDICES              |
| 11  | 10. BIBLIOGRAPHY           |
| 12  | 11. INDEX                  |
| 13  | 12. GLOSSARY               |
| 14  | 13. LIST OF FIGURES        |
| 15  | 14. LIST OF TABLES         |
| 16  | 15. LIST OF ABBREVIATIONS  |
| 17  | 16. LIST OF SYMBOLS        |
| 18  | 17. LIST OF EQUATIONS      |
| 19  | 18. LIST OF REFERENCES     |
| 20  | 19. LIST OF FIGURES        |
| 21  | 20. LIST OF TABLES         |
| 22  | 21. LIST OF ABBREVIATIONS  |
| 23  | 22. LIST OF SYMBOLS        |
| 24  | 23. LIST OF EQUATIONS      |
| 25  | 24. LIST OF REFERENCES     |
| 26  | 25. LIST OF FIGURES        |
| 27  | 26. LIST OF TABLES         |
| 28  | 27. LIST OF ABBREVIATIONS  |
| 29  | 28. LIST OF SYMBOLS        |
| 30  | 29. LIST OF EQUATIONS      |
| 31  | 30. LIST OF REFERENCES     |
| 32  | 31. LIST OF FIGURES        |
| 33  | 32. LIST OF TABLES         |
| 34  | 33. LIST OF ABBREVIATIONS  |
| 35  | 34. LIST OF SYMBOLS        |
| 36  | 35. LIST OF EQUATIONS      |
| 37  | 36. LIST OF REFERENCES     |
| 38  | 37. LIST OF FIGURES        |
| 39  | 38. LIST OF TABLES         |
| 40  | 39. LIST OF ABBREVIATIONS  |
| 41  | 40. LIST OF SYMBOLS        |
| 42  | 41. LIST OF EQUATIONS      |
| 43  | 42. LIST OF REFERENCES     |
| 44  | 43. LIST OF FIGURES        |
| 45  | 44. LIST OF TABLES         |
| 46  | 45. LIST OF ABBREVIATIONS  |
| 47  | 46. LIST OF SYMBOLS        |
| 48  | 47. LIST OF EQUATIONS      |
| 49  | 48. LIST OF REFERENCES     |
| 50  | 49. LIST OF FIGURES        |
| 51  | 50. LIST OF TABLES         |
| 52  | 51. LIST OF ABBREVIATIONS  |
| 53  | 52. LIST OF SYMBOLS        |
| 54  | 53. LIST OF EQUATIONS      |
| 55  | 54. LIST OF REFERENCES     |
| 56  | 55. LIST OF FIGURES        |
| 57  | 56. LIST OF TABLES         |
| 58  | 57. LIST OF ABBREVIATIONS  |
| 59  | 58. LIST OF SYMBOLS        |
| 60  | 59. LIST OF EQUATIONS      |
| 61  | 60. LIST OF REFERENCES     |
| 62  | 61. LIST OF FIGURES        |
| 63  | 62. LIST OF TABLES         |
| 64  | 63. LIST OF ABBREVIATIONS  |
| 65  | 64. LIST OF SYMBOLS        |
| 66  | 65. LIST OF EQUATIONS      |
| 67  | 66. LIST OF REFERENCES     |
| 68  | 67. LIST OF FIGURES        |
| 69  | 68. LIST OF TABLES         |
| 70  | 69. LIST OF ABBREVIATIONS  |
| 71  | 70. LIST OF SYMBOLS        |
| 72  | 71. LIST OF EQUATIONS      |
| 73  | 72. LIST OF REFERENCES     |
| 74  | 73. LIST OF FIGURES        |
| 75  | 74. LIST OF TABLES         |
| 76  | 75. LIST OF ABBREVIATIONS  |
| 77  | 76. LIST OF SYMBOLS        |
| 78  | 77. LIST OF EQUATIONS      |
| 79  | 78. LIST OF REFERENCES     |
| 80  | 79. LIST OF FIGURES        |
| 81  | 80. LIST OF TABLES         |
| 82  | 81. LIST OF ABBREVIATIONS  |
| 83  | 82. LIST OF SYMBOLS        |
| 84  | 83. LIST OF EQUATIONS      |
| 85  | 84. LIST OF REFERENCES     |
| 86  | 85. LIST OF FIGURES        |
| 87  | 86. LIST OF TABLES         |
| 88  | 87. LIST OF ABBREVIATIONS  |
| 89  | 88. LIST OF SYMBOLS        |
| 90  | 89. LIST OF EQUATIONS      |
| 91  | 90. LIST OF REFERENCES     |
| 92  | 91. LIST OF FIGURES        |
| 93  | 92. LIST OF TABLES         |
| 94  | 93. LIST OF ABBREVIATIONS  |
| 95  | 94. LIST OF SYMBOLS        |
| 96  | 95. LIST OF EQUATIONS      |
| 97  | 96. LIST OF REFERENCES     |
| 98  | 97. LIST OF FIGURES        |
| 99  | 98. LIST OF TABLES         |
| 100 | 99. LIST OF ABBREVIATIONS  |
| 101 | 100. LIST OF SYMBOLS       |
| 102 | 101. LIST OF EQUATIONS     |
| 103 | 102. LIST OF REFERENCES    |
| 104 | 103. LIST OF FIGURES       |
| 105 | 104. LIST OF TABLES        |
| 106 | 105. LIST OF ABBREVIATIONS |
| 107 | 106. LIST OF SYMBOLS       |
| 108 | 107. LIST OF EQUATIONS     |
| 109 | 108. LIST OF REFERENCES    |
| 110 | 109. LIST OF FIGURES       |
| 111 | 110. LIST OF TABLES        |
| 112 | 111. LIST OF ABBREVIATIONS |
| 113 | 112. LIST OF SYMBOLS       |
| 114 | 113. LIST OF EQUATIONS     |
| 115 | 114. LIST OF REFERENCES    |
| 116 | 115. LIST OF FIGURES       |
| 117 | 116. LIST OF TABLES        |
| 118 | 117. LIST OF ABBREVIATIONS |
| 119 | 118. LIST OF SYMBOLS       |
| 120 | 119. LIST OF EQUATIONS     |
| 121 | 120. LIST OF REFERENCES    |
| 122 | 121. LIST OF FIGURES       |
| 123 | 122. LIST OF TABLES        |
| 124 | 123. LIST OF ABBREVIATIONS |
| 125 | 124. LIST OF SYMBOLS       |
| 126 | 125. LIST OF EQUATIONS     |
| 127 | 126. LIST OF REFERENCES    |
| 128 | 127. LIST OF FIGURES       |
| 129 | 128. LIST OF TABLES        |
| 130 | 129. LIST OF ABBREVIATIONS |
| 131 | 130. LIST OF SYMBOLS       |
| 132 | 131. LIST OF EQUATIONS     |
| 133 | 132. LIST OF REFERENCES    |
| 134 | 133. LIST OF FIGURES       |
| 135 | 134. LIST OF TABLES        |
| 136 | 135. LIST OF ABBREVIATIONS |
| 137 | 136. LIST OF SYMBOLS       |
| 138 | 137. LIST OF EQUATIONS     |
| 139 | 138. LIST OF REFERENCES    |
| 140 | 139. LIST OF FIGURES       |
| 141 | 140. LIST OF TABLES        |
| 142 | 141. LIST OF ABBREVIATIONS |
| 143 | 142. LIST OF SYMBOLS       |
| 144 | 143. LIST OF EQUATIONS     |
| 145 | 144. LIST OF REFERENCES    |
| 146 | 145. LIST OF FIGURES       |
| 147 | 146. LIST OF TABLES        |
| 148 | 147. LIST OF ABBREVIATIONS |
| 149 | 148. LIST OF SYMBOLS       |
| 150 | 149. LIST OF EQUATIONS     |
| 151 | 150. LIST OF REFERENCES    |
| 152 | 151. LIST OF FIGURES       |
| 153 | 152. LIST OF TABLES        |
| 154 | 153. LIST OF ABBREVIATIONS |
| 155 | 154. LIST OF SYMBOLS       |
| 156 | 155. LIST OF EQUATIONS     |
| 157 | 156. LIST OF REFERENCES    |
| 158 | 157. LIST OF FIGURES       |
| 159 | 158. LIST OF TABLES        |
| 160 | 159. LIST OF ABBREVIATIONS |
| 161 | 160. LIST OF SYMBOLS       |
| 162 | 161. LIST OF EQUATIONS     |
| 163 | 162. LIST OF REFERENCES    |
| 164 | 163. LIST OF FIGURES       |
| 165 | 164. LIST OF TABLES        |
| 166 | 165. LIST OF ABBREVIATIONS |
| 167 | 166. LIST OF SYMBOLS       |
| 168 | 167. LIST OF EQUATIONS     |
| 169 | 168. LIST OF REFERENCES    |
| 170 | 169. LIST OF FIGURES       |
| 171 | 170. LIST OF TABLES        |
| 172 | 171. LIST OF ABBREVIATIONS |
| 173 | 172. LIST OF SYMBOLS       |
| 174 | 173. LIST OF EQUATIONS     |
| 175 | 174. LIST OF REFERENCES    |
| 176 | 175. LIST OF FIGURES       |
| 177 | 176. LIST OF TABLES        |
| 178 | 177. LIST OF ABBREVIATIONS |
| 179 | 178. LIST OF SYMBOLS       |
| 180 | 179. LIST OF EQUATIONS     |
| 181 | 180. LIST OF REFERENCES    |
| 182 | 181. LIST OF FIGURES       |
| 183 | 182. LIST OF TABLES        |
| 184 | 183. LIST OF ABBREVIATIONS |
| 185 | 184. LIST OF SYMBOLS       |
| 186 | 185. LIST OF EQUATIONS     |
| 187 | 186. LIST OF REFERENCES    |
| 188 | 187. LIST OF FIGURES       |
| 189 | 188. LIST OF TABLES        |
| 190 | 189. LIST OF ABBREVIATIONS |
| 191 | 190. LIST OF SYMBOLS       |
| 192 | 191. LIST OF EQUATIONS     |
| 193 | 192. LIST OF REFERENCES    |
| 194 | 193. LIST OF FIGURES       |
| 195 | 194. LIST OF TABLES        |
| 196 | 195. LIST OF ABBREVIATIONS |
| 197 | 196. LIST OF SYMBOLS       |
| 198 | 197. LIST OF EQUATIONS     |
| 199 | 198. LIST OF REFERENCES    |
| 200 | 199. LIST OF FIGURES       |
| 201 | 200. LIST OF TABLES        |
| 202 | 201. LIST OF ABBREVIATIONS |
| 203 | 202. LIST OF SYMBOLS       |
| 204 | 203. LIST OF EQUATIONS     |
| 205 | 204. LIST OF REFERENCES    |
| 206 | 205. LIST OF FIGURES       |
| 207 | 206. LIST OF TABLES        |
| 208 | 207. LIST OF ABBREVIATIONS |
| 209 | 208. LIST OF SYMBOLS       |
| 210 | 209. LIST OF EQUATIONS     |
| 211 | 210. LIST OF REFERENCES    |
| 212 | 211. LIST OF FIGURES       |
| 213 | 212. LIST OF TABLES        |
| 214 | 213. LIST OF ABBREVIATIONS |
| 215 | 214. LIST OF SYMBOLS       |
| 216 | 215. LIST OF EQUATIONS     |
| 217 | 216. LIST OF REFERENCES    |
| 218 | 217. LIST OF FIGURES       |
| 219 | 218. LIST OF TABLES        |
| 220 | 219. LIST OF ABBREVIATIONS |
| 221 | 220. LIST OF SYMBOLS       |
| 222 | 221. LIST OF EQUATIONS     |
| 223 | 222. LIST OF REFERENCES    |
| 224 | 223. LIST OF FIGURES       |
| 225 | 224. LIST OF TABLES        |
| 226 | 225. LIST OF ABBREVIATIONS |
| 227 | 226. LIST OF SYMBOLS       |
| 228 | 227. LIST OF EQUATIONS     |
| 229 | 228. LIST OF REFERENCES    |
| 230 | 229. LIST OF FIGURES       |
| 231 | 230. LIST OF TABLES        |
| 232 | 231. LIST OF ABBREVIATIONS |
| 233 | 232. LIST OF SYMBOLS       |
| 234 | 233. LIST OF EQUATIONS     |
| 235 | 234. LIST OF REFERENCES    |
| 236 | 235. LIST OF FIGURES       |
| 237 | 236. LIST OF TABLES        |
| 238 | 237. LIST OF ABBREVIATIONS |
| 239 | 238. LIST OF SYMBOLS       |
| 240 | 239. LIST OF EQUATIONS     |
| 241 | 240. LIST OF REFERENCES    |
| 242 | 241. LIST OF FIGURES       |
| 243 | 242. LIST OF TABLES        |
| 244 | 243. LIST OF ABBREVIATIONS |
| 245 | 244. LIST OF SYMBOLS       |
| 246 | 245. LIST OF EQUATIONS     |
| 247 | 246. LIST OF REFERENCES    |
| 248 | 247. LIST OF FIGURES       |
| 249 | 248. LIST OF TABLES        |
| 250 | 249. LIST OF ABBREVIATIONS |
| 251 | 250. LIST OF SYMBOLS       |
| 252 | 251. LIST OF EQUATIONS     |
| 253 | 252. LIST OF REFERENCES    |
| 254 | 253. LIST OF FIGURES       |
| 255 | 254. LIST OF TABLES        |
| 256 | 255. LIST OF ABBREVIATIONS |
| 257 | 256. LIST OF SYMBOLS       |
| 258 | 257. LIST OF EQUATIONS     |
| 259 | 258. LIST OF REFERENCES    |
| 260 | 259. LIST OF FIGURES       |
| 261 | 260. LIST OF TABLES        |
| 262 | 261. LIST OF ABBREVIATIONS |
| 263 | 262. LIST OF SYMBOLS       |
| 264 | 263. LIST OF EQUATIONS     |
| 265 | 264. LIST OF REFERENCES    |
| 266 | 265. LIST OF FIGURES       |
| 267 | 266. LIST OF TABLES        |
| 268 | 267. LIST OF ABBREVIATIONS |
| 269 | 268. LIST OF SYMBOLS       |
| 270 | 269. LIST OF EQUATIONS     |
| 271 | 270. LIST OF REFERENCES    |
| 272 | 271. LIST OF FIGURES       |
| 273 | 272. LIST OF TABLES        |
| 274 | 273. LIST OF ABBREVIATIONS |
| 275 | 274. LIST OF SYMBOLS       |
| 276 | 275. LIST OF EQUATIONS     |
| 277 | 276. LIST OF REFERENCES    |
| 278 | 277. LIST OF FIGURES       |
| 279 | 278. LIST OF TABLES        |
| 280 | 279. LIST OF ABBREVIATIONS |
| 281 | 280. LIST OF SYMBOLS       |
| 282 | 281. LIST OF EQUATIONS     |
| 283 | 282. LIST OF REFERENCES    |
| 284 | 283. LIST OF FIGURES       |
| 285 | 284. LIST OF TABLES        |
| 286 | 285. LIST OF ABBREVIATIONS |
| 287 | 286. LIST OF SYMBOLS       |
| 288 | 287. LIST OF EQUATIONS     |
| 289 | 288. LIST OF REFERENCES    |
| 290 | 289. LIST OF FIGURES       |
| 291 | 290. LIST OF TABLES        |
| 292 | 291. LIST OF ABBREVIATIONS |
| 293 | 292. LIST OF SYMBOLS       |
| 294 | 293. LIST OF EQUATIONS     |
| 295 | 294. LIST OF REFERENCES    |
| 296 | 295. LIST OF FIGURES       |
| 297 | 296. LIST OF TABLES        |
| 298 | 297. LIST OF ABBREVIATIONS |
| 299 | 298. LIST OF SYMBOLS       |
| 300 | 299. LIST OF EQUATIONS     |
| 301 | 300. LIST OF REFERENCES    |
| 302 | 301. LIST OF FIGURES       |
| 303 | 302. LIST OF TABLES        |
| 304 | 303. LIST OF ABBREVIATIONS |
| 305 | 304. LIST OF SYMBOLS       |
| 306 | 305. LIST OF EQUATIONS     |
| 307 | 306. LIST OF REFERENCES    |
| 308 | 307. LIST OF FIGURES       |
| 309 | 308. LIST OF TABLES        |
| 310 | 309. LIST OF ABBREVIATIONS |
| 311 | 310. LIST OF SYMBOLS       |
| 312 | 311. LIST OF EQUATIONS     |
| 313 | 312. LIST OF REFERENCES    |
| 314 | 313. LIST OF FIGURES       |
| 315 | 314. LIST OF TABLES        |
| 316 | 315. LIST OF ABBREVIATIONS |
| 317 | 316. LIST OF SYMBOLS       |
| 318 | 317. LIST OF EQUATIONS     |
| 319 | 318. LIST OF REFERENCES    |
| 320 | 319. LIST OF FIGURES       |
| 321 | 320. LIST OF TABLES        |
| 322 | 321. LIST OF ABBREVIATIONS |
| 323 | 322. LIST OF SYMBOLS       |
| 324 | 323. LIST OF EQUATIONS     |
| 325 | 324. LIST OF REFERENCES    |
| 326 | 325. LIST OF FIGURES       |
| 327 | 326. LIST OF TABLES        |
| 328 | 327. LIST OF ABBREVIATIONS |
| 329 | 328. LIST OF SYMBOLS       |
| 330 | 329. LIST OF EQUATIONS     |
| 331 | 330. LIST OF REFERENCES    |
| 332 | 331. LIST OF FIGURES       |
| 333 | 332. LIST OF TABLES        |
| 334 | 333. LIST OF ABBREVIATIONS |
| 335 | 334. LIST OF SYMBOLS       |
| 336 | 335. LIST OF EQUATIONS     |
| 337 | 336. LIST OF REFERENCES    |
| 338 | 337. LIST OF FIGURES       |
| 339 | 338. LIST OF TABLES        |
| 340 | 339. LIST OF ABBREVIATIONS |
| 341 | 340. LIST OF SYMBOLS       |
| 342 | 341. LIST OF EQUATIONS     |
| 343 | 342. LIST OF REFERENCES    |
| 344 | 343. LIST OF FIGURES       |
| 345 | 344. LIST OF TABLES        |
| 346 | 345. LIST OF ABBREVIATIONS |
| 347 | 346. LIST OF SYMBOLS       |
| 348 | 347. LIST OF EQUATIONS     |
| 349 | 348. LIST OF REFERENCES    |
| 350 | 349. LIST OF FIGURES       |
| 351 | 350. LIST OF TABLES        |
| 352 | 351. LIST OF ABBREVIATIONS |
| 353 | 352. LIST OF SYMBOLS       |
| 354 | 353. LIST OF EQUATIONS     |
| 355 | 354. LIST OF REFERENCES    |
| 356 | 355. LIST OF FIGURES       |
| 357 | 356. LIST OF TABLES        |
| 358 | 357. LIST OF ABBREVIATIONS |
| 359 | 358. LIST OF SYMBOLS       |
| 360 | 359. LIST OF EQUATIONS     |
| 361 | 360. LIST OF REFERENCES    |
| 362 | 361. LIST OF FIGURES       |
| 363 | 362. LIST OF TABLES        |
| 364 | 363. LIST OF ABBREVIATIONS |
| 365 | 364. LIST OF SYMBOLS       |
| 366 | 365. LIST OF EQUATIONS     |
| 367 | 366. LIST OF REFERENCES    |
| 368 | 367. LIST OF FIGURES       |
| 369 | 368. LIST OF TABLES        |
| 370 | 369. LIST OF ABBREVIATIONS |
| 371 | 370. LIST OF SYMBOLS       |
| 372 | 371. LIST OF EQUATIONS     |
| 373 | 372. LIST OF REFERENCES    |
| 374 | 373. LIST OF FIGURES       |
| 375 | 374. LIST OF TABLES        |
| 376 | 375. LIST OF ABBREVIATIONS |
| 377 | 376. LIST OF SYMBOLS       |
| 378 | 377. LIST OF EQUATIONS     |
| 379 | 378. LIST OF REFERENCES    |
| 380 | 379. LIST OF FIGURES       |
| 381 | 380. LIST OF TABLES        |
| 382 | 381. LIST OF ABBREVIATIONS |
| 383 | 382. LIST OF SYMBOLS       |
| 384 | 383. LIST OF EQUATIONS     |
| 385 | 384. LIST OF REFERENCES    |
| 386 | 385. LIST OF FIGURES       |
| 387 | 386. LIST OF TABLES        |
| 388 | 387. LIST OF ABBREVIATIONS |
| 389 | 388. LIST OF SYMBOLS       |
| 390 | 389. LIST OF EQUATIONS     |
| 391 | 390. LIST OF REFERENCES    |
| 392 | 391. LIST OF FIGURES       |
| 393 | 392. LIST OF TABLES        |
| 394 | 393. LIST OF ABBREVIATIONS |
| 395 | 394. LIST OF SYMBOLS       |
| 396 | 395. LIST OF EQUATIONS     |
| 397 | 396. LIST OF REFERENCES    |
| 398 | 397. LIST OF FIGURES       |
| 399 | 398. LIST OF TABLES        |
| 400 | 399. LIST OF ABBREVIATIONS |
| 401 | 400. LIST OF SYMBOLS       |
| 402 | 401. LIST OF EQUATIONS     |
| 403 | 402. LIST OF REFERENCES    |
| 404 | 403. LIST OF FIGURES       |
| 405 | 404. LIST OF TABLES        |
| 406 | 405. LIST OF ABBREVIATIONS |
| 407 | 406. LIST OF SYMBOLS       |
| 408 | 407. LIST OF EQUATIONS     |
| 409 | 408. LIST OF REFERENCES    |
| 410 | 409. LIST OF FIGURES       |
| 411 | 410. LIST OF TABLES        |
| 412 | 411. LIST OF ABBREVIATIONS |
| 413 | 412. LIST OF SYMBOLS       |
| 414 | 4                          |

# I. LIQUID METAL FAST BREEDER REACTORS--CIVILIAN

## A. Physics Development--LMFBR

### 1. Theoretical Reactor Physics

#### a. General Reactor Physics

##### (i) Resonance and Doppler Theory (R. N. Hwang and Y. Kikuchi)

Last Reported: ANL-7640, pp. 1-5 (Nov 1969).

(a) The Fission Widths of  $^{239}\text{Pu}$  with the Assumption of a Double-humped Potential. A grouping structure has been observed for

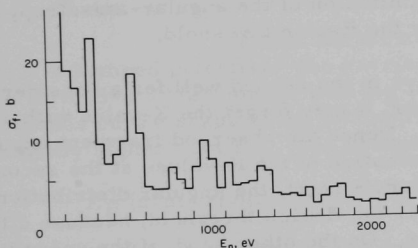


Fig. I.A.1. Petrel Data for Fission Cross Section of  $^{239}\text{Pu}$  Averaged over 50-eV Intervals

fission cross sections data of  $^{239}\text{Pu}$ . The mean spacing is about 200 eV and the mean width (HMW) of this structure is less than 100 eV,\* although large statistical fluctuations due to the small number of levels in the energy region over which the averaging is done makes it difficult to obtain precise mean values. This behavior is shown in Fig. I.A.1.

subthreshold fission cross section of  $^{240}\text{Pu}$ \*\* and is considered due to the existence of quasi-stable states in the second minimum point of the fission barrier.

From the channel theory of nuclear fission,<sup>†</sup> the  $0^+$ ,  $1^-$ ,  $2^-$  states of  $^{240}\text{Pu}$  (the compound nucleus after  $^{239}\text{Pu}$  absorbs a neutron) have one or two completely open channels, the  $1^+$  state has a partially open channel, and the  $0^-$  state has nearly no channel. As the grouping structure is considered to be predominant in the subthreshold energy range, we assume that this structure is due to the  $1^+$  state.

(b) Shape of the Fission Potential. The potential-energy curve is assumed to be as shown in Fig. I.A.2. In this potential there are two types of intermediate equilibrium states in the compound nucleus. The states of the first well (the normal compound states) are denoted as Class I states and those of the second well as Class II.

\*These values are obtained by averaging the Petrel data; see LA-3586 (1967).

\*\*Migneco, E., and Theobald, J. P., Nucl. Phys., A112, 603 (1968).

† Kikuchi, Y., and An, S., Nucl. Sci. Tech. 5, 86 (1968).

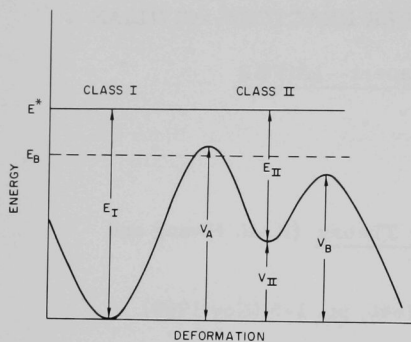


Fig. 1.A.2. Assumed Potential-energy Function

The conception of the saddle point must be changed with this potential. Which barrier top, A and B, should be considered as the saddle point? It may be reasonable to regard the higher barrier as the saddle point, considering the relation with the fission threshold.

The next problem is to determine which barrier is higher.

Björnholm and Strutinsky\* assumed that the barrier B was higher in the light nuclides such as  $^{231}\text{Th}$  and the barrier A was higher in the heavy nuclides such as  $^{241}\text{Pu}$ . This dis-

cussion follows from a systematic examination of the angular-anisotropy behavior of the fission fragments near the fission threshold.

If the nucleus stays in the second well for a considerable time after passing the first barrier, it may forget the K-value with which it passes over the first barrier. Hence the observed fragment angular anisotropy corresponds to the distribution of the K-values at the second barrier. If the second barrier is the saddle point, the angular distribution will change drastically with energy near the fission threshold, because different channels have different K-values. On the other hand, if the second barrier is 1-2 MeV lower than the first, there are so many channels at the second barrier that the average K-value does not change with energy. As a result the angular anisotropy is nearly constant with energy.

The experimental results show that the fragment angular anisotropy changes drastically with energy for light nuclei ( $A \leq 238$ ) and is nearly constant for heavy nuclei ( $A \geq 239$ ). This means that the second barrier is the saddle point for light nuclei and the first is the saddle point for heavy nuclei.

From this discussion, we can assume that the barrier A is higher than B for  $^{240}\text{Pu}$ .

The depth of the second minimum point can be estimated from the difference of the mean level spacings between Class I and Class II states. The relation between the mean level spacings and the excitation energies is given by a simple formula based on the Fermi gas model:

\* Björnholm, S., and Strutinsky, V. M., Nucl. Phys. A136, 7 (1969).

$$\frac{\langle D_{II} \rangle}{\langle D_I \rangle} = \left( \frac{E_I}{E_{II}} \right)^{5/4} \exp \left\{ 0.056 \sqrt{A} \left( \sqrt{E_{II}} - \sqrt{E_I} \right) \right\}, \quad (1)$$

where  $D_I$  and  $D_{II}$  are the mean level spacings of the Class I and Class II states, respectively, and  $E_I$  and  $E_{II}$  the corresponding excitation energies. In our case

$$E_I \equiv E^* = E_B + E_n; \quad E_{II} \equiv E^* - V_{II}, \quad (2)$$

where  $E^*$  is the total excitation energy of the compound nucleus,  $E_B$  the neutron binding energy, and  $E_n$  the neutron energy. In the energy range under consideration,  $E_I = E^* \simeq E_B$ .

Using  $D_I = 3$  eV,  $D_{II} = 200$  eV, and  $E_I = 6.5$  MeV, we get  $E_{II} = 4.0$  MeV. Hence,  $V_{II} = E^* - E_{II} = 2.5$  MeV.

From the assumption of the channel theory with a single humped potential,<sup>†</sup> the barrier height of the saddle point is estimated to be 0.15-0.2 MeV higher than  $E_B$  for the  $1^+$  state. Though this difference depends on the shape of the potential barrier, we can assume that  $V_A$  is slightly higher than  $E_B$ . The estimated values are as follows:

$E_B$  (neutron binding energy) : 6.5 MeV

$V_A$  (the first barrier height) :  $> E_B$  (6.6-6.7 MeV)

$V_{II}$  (the second minimum point): 2.7 MeV

$V_B$  (the second barrier height):  $< V_A$

(c) Formulation of the Fission Width.<sup>††</sup> In the present formulation, we assume that only one Class II state is predominant in the given energy range, because the intermediate groups of  $^{239}\text{Pu}$  are fairly well separated. The total Hamiltonian  $H$  is divided into  $H_0$  and  $V$ , where  $H_0$  is diagonal in the space of the functions:

$\psi_n$  (neutron scattering state)

$\psi_f$  (scission state)

$\phi_j$  (compound state of Class I);  $j = 1, \dots, \ell$

$\Phi$  (compound state of Class II),

<sup>†</sup> Kikuchi, Y., and An, S., *loc. cit.*

<sup>††</sup> This formulation is mainly due to H. Weigmann, Z. Physik 214, 7 (1968).

with the eigenvalues:

$$\langle \phi_j | H_0 | \phi_k \rangle = E_j \delta_{jk}; \quad j, k = 1, \dots, \ell;$$

$$\langle \Phi | H_0 | \Phi \rangle = E_0.$$

With the residual interaction  $V$ , these states are mixed. In this stage we make the following two assumptions:

- (1) a Class I state has no fission channels:  
 $\langle \phi_j | V | \psi_f \rangle = 0;$
- (2) a Class II state has no neutron channels:  
 $\langle \Phi | V | \psi_n \rangle = 0.$

Then we define the matrix elements:

$$\langle \phi_j | V | \phi_k \rangle = V_{jk}; \quad j \neq k;$$

$$\langle \phi_j | V | \Phi \rangle = W_j;$$

$$\langle \Phi | V | \psi_f \rangle = W_0;$$

$$\langle \phi_j | V | \psi_n \rangle = V_j.$$

We further assume that the mixing is weak enough to be treated as a perturbation. Then the perturbed wave functions of the compound nucleus are expressed as

$$\begin{aligned} \psi_0 &\cong \left[ 1 - \sum_j \frac{W_j^2}{2(E_j - E_0)^2} \right] \Phi + \sum_j \frac{W_j}{E_j - E_0} \phi_j; \\ \psi_j &\cong \left[ 1 - \frac{W_j^2}{2(E_j - E_0)^2} \right] \phi_j + \frac{W_j}{E_j - E_0} \Phi + \sum_{k \neq j} \frac{V_{jk}}{E_j - E_k} \phi_k. \end{aligned} \quad (3)$$

We call  $\psi_j$  and  $\psi_0$  the perturbed Class I state and the perturbed Class II state, respectively.

It was shown by Weidenmüller and his co-workers\* that the  $S$  matrices for neutron elastic scattering and neutron-induced fission are given by

\*Weidenmüller, H. A., Nucl. Phys. 75, 189 (1966); Weidenmüller, H. A., and Dietrich, K., *ibid.*, 83, 332 (1966); Mahaux, C., and Weidenmüller, H. A., *ibid.*, A91, 241 (1967).

$$S_{nn} = e^{2i\delta_n} \left( 1 - i \sum_j \frac{\Gamma_{jn}}{E - \mu_j} - i \frac{\Gamma_{on}}{E - \mu_0} \right)$$

and

$$S_{nf} = -ie^{i(\delta_n + \delta_f)} \left( \sum_j \frac{\Gamma_{jn}^{1/2} \Gamma_{jf}^{1/2}}{E - \mu_j} + \frac{\Gamma_{on}^{1/2} \Gamma_{of}^{1/2}}{E - \mu_0} \right), \quad (4)$$

where  $\mu_j$  and  $\mu_0$  are the poles that correspond to  $\psi_j$  and  $\psi_0$  states, respectively, and  $\Gamma_{jn}$ ,  $\Gamma_{jf}$ ,  $\Gamma_{on}$ , and  $\Gamma_{of}$  are the neutron and fission widths corresponding to these states. It is shown in the following how to calculate these parameters. The poles  $\mu_j$  and  $\mu_0$  are given as a solution of the equation

$$D \equiv \begin{vmatrix} (E - E_j)\delta_{jk} - F_{jk} + i\pi V_j V_k - (1 - \delta_{jk})V_{jk} & W_j \\ W_k & (E - E_0) - F_0 + i\pi W_0^2 \end{vmatrix} = 0; \quad (5)$$

$$F_{jk} = P \int dE' \frac{V_j V_k}{E - E'}; \quad F_0 = P \int dE' \frac{W_0^2}{E - E'},$$

where  $P$  means the principal value.

By assuming  $V_j$  and  $W_0$  to be independent of  $E$ , we put  $F_{jk} = F_0 = 0$ . Then the following sum rules hold:

$$\sum_j \Gamma_{jn} + \Gamma_{on} = 2\pi \sum_j V_j^2; \quad (6)$$

$$\sum_j \Gamma_{jf} + \Gamma_{of} = 2\pi W_0^2 \equiv \Gamma^\dagger, \quad (7)$$

where  $\Gamma^\dagger$  is the decaying width of the unperturbed Class II state ( $\Phi$ ) into scission.

We also define the decaying width of the unperturbed Class II state ( $\Phi$ ) into the many Class I states as

$$\Gamma^\downarrow = \frac{2\pi}{D_I} \overline{W_j^2}, \quad (8)$$

where the bar means the mean value  $\Gamma^\dagger$  must be larger than  $\Gamma^\downarrow$ , as the barrier  $A$  is higher than the barrier  $B$ .

In the following discussion, we neglect the coupling of the Class I states  $\phi_j$  with each other (directly and via  $\psi_n$  states), both being assumed to be small compared with their coupling with  $\Phi$ . Then by putting  $V_{jk} = 0$  and  $\pi V_j V_k = V_j^2 \delta_{jk}$ , Eq. (5) can be written as

$$D = (E - E_0 + i\pi W_0^2) \left[ \prod_j (E - E_j + i\pi V_j^2) \right] - \sum_k W_k^2 \left[ \prod_{j \neq k} (E - E_j + i\pi V_j^2) \right] = 0; \quad (9)$$

$$E - E_0 + i\pi W_0^2 = \sum_k \frac{W_k^2}{E - E_k + i\pi V_k^2}. \quad (10)$$

In the calculation of  $\mu_j$  for the perturbed Class I states, we neglect the  $k \neq j$  terms on the right-hand side of Eq. (10) for  $\mu_j$ , as the neutron width is much smaller than  $E_j - E_k$ . Then

$$\mu_j - E_0 + i\pi W_0^2 = \frac{W_j^2}{\mu_j - E_j + i\pi V_j^2}. \quad (11)$$

By solving this quadratic equation, we get two  $\mu_j$  values. Taking one whose real part is near to  $E_j$ , we get

$$\text{Im} \mu_j = \pi V_j^2 + \frac{2W_j^2 \pi W_0^2}{(E_j - E_0)^2 + \pi^2 W_0^4}. \quad (12)$$

Then,

$$\Gamma_j = -2\text{Im} \mu_j = 2\pi V_j^2 + \frac{W_j^2 \Gamma^\dagger}{(E_j - E_0)^2 + (1/4)(\Gamma^\dagger)^2}. \quad (13)$$

We can interpret the two terms of Eq. (13) as

$$\Gamma_{jn} = 2\pi V_j^2; \quad (14)$$

$$\Gamma_{jf} = \frac{W_j^2 \Gamma^\dagger}{(E_j - E_0)^2 + (1/4)(\Gamma^\dagger)^2}. \quad (15)$$

For the perturbed Class II state,  $\mu_0$  is obtained from Eq. (10) by putting  $\mu_0 \cong E_0 - i\pi W_0^2$  on the right-hand side:



$$\mu_0 - E_0 + i\pi W_0^2 = \sum_k \frac{W_k^2}{(E_0 - E_k) + i\pi(V_k^2 - W_0^2)}; \quad (16)$$

$$\Gamma_0 = -2\text{Im}\mu_0 = 2\pi W_0^2 + \sum_k \frac{W_k^2 2\pi(V_k^2 - W_0^2)}{(E_0 - E_k)^2 + \pi^2(V_k^2 - W_0^2)^2}. \quad (17)$$

Equation (10) can be interpreted as below, by neglecting  $V_k^2$  in the denominator;

$$\Gamma_{0n} = \sum_j \frac{2\pi V_j^2 W_j^2}{(E_j - E_0)^2 + (1/4)(\Gamma^\dagger)^2} = \sum_j \frac{\Gamma_{jn} W_j^2}{(E_j - E_0)^2 + (1/4)(\Gamma^\dagger)^2}; \quad (18)$$

$$\Gamma_{0n} = \Gamma^\dagger - \sum_j \frac{W_j^2 \Gamma^\dagger}{(E_j - E_0)^2 + (1/4)(\Gamma^\dagger)^2} = \Gamma^\dagger - \sum_j \Gamma_{fj}. \quad (19)$$

Equation (19) is consistent with the sum rule Eq. (17).

In this formulation we do not consider the neutron penetration effect in  $\Gamma_n$ . Thus these equations must be applied in the energy range for which  $\Gamma_n$  is nearly constant within the energy range of averaging. Hence, these equations are valid above a few hundred eV.

(d) Estimation of  $\Gamma^\dagger$ ,  $\Gamma^\dagger$ ,  $\Gamma_{jf}$ ,  $\Gamma_{jn}$ ,  $\Gamma_{of}$ , and  $\Gamma_{0n}$ . We use the Petrel data averaged over a 50-eV range and the resonance parameters in the new version of ENDF/B in order to estimate these values. First, the contribution of the  $0^+$ ,  $0^-$ ,  $1^-$ ,  $2^-$  states are calculated with the resonance parameters in the new ENDF/B and subtracted from the averaged fission-cross-section data so as to get the average fission cross section of the  $1^+$  state. Secondly, the averaged fission widths are deduced from these average fission cross sections. Finally, Eq. (15) is applied and the resonance parameters of the intermediate resonances ( $E_R$ ,  $\Gamma^\dagger$ ,  $W^2$ ) are obtained. The results are shown in Table I.A.1.\* From Table I.A.1 we get  $D_{II} \cong 210$  eV and  $\overline{\Gamma^\dagger} = 56$  eV. The mean fission width below 8 keV is about 60 meV.

Averaging Eq. (15), we get

$$\overline{\Gamma_f^{(1+)}} = \frac{1}{E_2 - E_1} \int_{E_1}^{E_2} \Gamma_{fj} = \frac{2\pi}{D_{II}} \overline{W_j^2}.$$

---

\*Kikuchi, Y., to be published in Trans. ANS.

Putting  $D_{II} = 220$  eV and  $\bar{\Gamma}_f^{(1+)} = 60$  meV, we get

$$\overline{W^2} \cong 2 \text{ (eV)}^2; \quad \Gamma^\dagger \cong \frac{2\pi \overline{W_j^2}}{D} \cong 4 \text{ eV}.$$

For the Class II state,

$$\Gamma_{on} \cong \frac{2\pi}{D_I} \frac{\bar{\Gamma}_{jn} \overline{W_j^2}}{\Gamma^\dagger} \cong 0.02 \bar{\Gamma}_{jn}; \quad \Gamma_{of} \cong \bar{\Gamma}^\dagger - \frac{2\pi \overline{W_j^2}}{D_I} = \Gamma^\dagger.$$

The value of  $\Gamma_{on}$  is so small that we need not consider this level in the neutron-induced fission process.

TABLE I.A.1. Resonance Parameters of the Intermediate Structure of  $^{239}\text{Pu}$

| $E_R$ (eV) | $\Gamma^\dagger$ (eV) | $\overline{W^2}$ (eV) <sup>2</sup> | Peak Value (eV) |
|------------|-----------------------|------------------------------------|-----------------|
| 83         | 22                    | 5.0                                | 0.909           |
| 266        | 50                    | 1.7                                | 0.136           |
| 465        | 20                    | 4.0                                | 0.800           |
| 512        | 34                    | 3.6                                | 0.424           |
| 791        | 25                    | 1.2                                | 0.192           |
| 995        | 40                    | 4.2                                | 0.420           |
| 1138       | 11                    | 1.5                                | 0.545           |
| 1340       | 50                    | 2.8                                | 0.224           |
| 1800       | 20                    | 0.8                                | 0.160           |
| 2301       | 36                    | 0.5                                | 0.056           |
| 2450       | 16                    | 0.7                                | 0.181           |
| 2677       | 19                    | 0.7                                | 0.147           |
| 2788       | 55                    | 1.5                                | 0.109           |
| 2953       | 70                    | 0.5                                | 0.286           |
| 3160       | 30                    | 2.6                                | 0.347           |
| 3256       | 10                    | 1.6                                | 0.640           |
| 3683       | 110                   | 1.8                                | 0.065           |
| 3800       | 40                    | 1.7                                | 0.170           |
| 3930       | 54                    | 1.2                                | 0.089           |
| 4192       | 84                    | 1.2                                | 0.057           |
| 4444       | 43                    | 1.2                                | 0.112           |
| 4563       | 91                    | 2.9                                | 0.127           |
| 4900       | 200                   | 0.8                                | 0.016           |
| 5236       | 52                    | 4.5                                | 0.346           |
| 5517       | 76                    | 4.2                                | 0.221           |
| 5610       | 57                    | 2.2                                | 0.154           |
| 5798       | 10                    | 1.3                                | 0.520           |
| 5821       | 80                    | 6.5                                | 0.325           |
| 6180       | 230                   | 3.5                                | 0.061           |
| 6546       | 55                    | 0.8                                | 0.058           |
| 6699       | 28                    | 3.9                                | 0.557           |
| 6799       | 17                    | 1.0                                | 0.230           |
| 7032       | 69                    | 1.6                                | 0.093           |
| 7367       | 115                   | 6.1                                | 0.212           |
| 7451       | 28                    | 1.7                                | 0.249           |
| 7548       | 75                    | 5.1                                | 0.272           |
| Mean       | 56                    | 2.4                                | 0.170           |

(e) Statistical Properties of  $\Gamma_f^{(1+)}$ . From Eq. (15), the statistical behavior of  $\Gamma_f^{(1+)}$  is mainly due to that of  $W_j^2$ . As  $W_j^2$  is considered to be essentially the penetration probability of the subthreshold barrier A, the statistical distribution must be the  $\chi^2$  distribution with one degree of freedom.

The statistical distribution of  $\Gamma^\dagger$  for each Class II state can be estimated from  $D_{II}$  and  $\Gamma^\dagger$ . As  $\Gamma^\dagger$  is the penetration probability of the second barrier B, the following relation with  $D_{II}$  may be valid:

$$\Gamma^\dagger = \frac{D_{II}}{2\pi} N,$$

where  $N$  is the number of channels at the second barrier. From  $\Gamma^\dagger \cong 56$  eV and  $D_{II} = 200$  eV, we get  $N = 1$ . Then  $\Gamma^\dagger$  has a  $\chi^2$ -distribution with one degree of freedom.

(ii) Analyses of Neutronic Characteristics of Reactors and Fuel Cycles (D. A. Meneley and L. J. Hoover)

Last Reported: ANL-7640, pp. 5-8 (Nov 1969).

Minimizing the number of neutron energy groups used in fuel-cycle calculations can be beneficial, through reduced computation time, if accuracy is not seriously compromised. To illustrate the effects of various group structures and collapsing methods, five different collapsed group structures were studied. Both single flux spectra and region-dependent flux spectra were used for collapsing. The results presented for collapsing with a single flux spectrum were previously reported.\* The standard linear flux weighting was used for all cross-section collapsing with the following exception: when using a region-dependent flux spectrum, the transport cross section was obtained from Travelli's Eq. (42).\*\*

The fuel-cycle package in the ARC System<sup>†</sup> was used. REBUS, an acronym for REactor BUrnup System, computes equilibrium fuel-cycle conditions. In these calculations, the burn time or cycle time was divided into two subintervals, with the fluxes computed at the beginning of cycle, middle of cycle, and end of cycle. The burn time was adjusted to achieve a core-averaged discharge burnup of 100,000 MWd/t. The feed enrichments were constrained to achieve criticality at the end of cycle. In addition, the control densities were fixed at cycle-averaged values. The neutronics solution was done with the two-dimensional diffusion-theory module in the ARC System.

\* Hoover, L. J., and Meneley, D. A., Trans. ANS 12, 441-442 (1969).

\*\* Travelli, A., in Reactor Physics Division Annual Report, July 1, 1967 to June 1968, ANL-7410 (Jan 1969), pp. 413-421.

<sup>†</sup> Toppel, B. J., et al., ANL-7322 (Nov 1967).

Two typical 1000-MWe, oxide-fueled reactors, the GE Advanced and Conservative designs,\* were analyzed. The Conservative design has a higher core-to-blanket leakage fraction than the Advanced Design. Both cores have multiple enrichment zones for power flattening and fractional-batch scatter-reloading fuel-management schemes.

By use of ultrafine-group P1 option in the MC<sup>2</sup> code,\*\* the microscopic cross sections were obtained from the ENDF/B file for estimated midcycle conditions. The energy range from 10 MeV to 22.6 eV was divided into 26 groups, each having a lethargy width of 0.5.

A two-dimensional diffusion-theory calculation for the estimated midcycle conditions gave the region-dependent flux spectrum. The centerline flux was chosen as the single flux spectrum. Problems were run using the various group structures shown in Table I.A.2.

TABLE I.A.2. Structures of Neutron Energy Groups

| 13 Groups<br>(eV)   | 8 Groups<br>(eV)    | 7 Groups<br>(eV)    | 6 Groups<br>(eV)    | 4 Groups<br>(eV)    |
|---------------------|---------------------|---------------------|---------------------|---------------------|
| $10.00 \times 10^6$ | $10.00 \times 10^6$ | $10.00 \times 10^6$ | $10.00 \times 10^6$ | $10.00 \times 10^6$ |
| $36.79 \times 10^5$ |                     |                     |                     |                     |
| $13.53 \times 10^5$ | $22.31 \times 10^5$ |                     |                     |                     |
| $49.79 \times 10^4$ | $49.79 \times 10^4$ | $13.53 \times 10^5$ | $13.53 \times 10^5$ |                     |
| $18.32 \times 10^4$ |                     | $30.20 \times 10^4$ |                     | $49.79 \times 10^4$ |
| $67.38 \times 10^3$ | $11.11 \times 10^4$ |                     | $18.32 \times 10^4$ |                     |
| $24.79 \times 10^3$ | $24.79 \times 10^3$ | $67.38 \times 10^3$ |                     |                     |
| $91.19 \times 10^2$ |                     | $24.79 \times 10^3$ | $24.79 \times 10^3$ | $24.79 \times 10^3$ |
| $33.55 \times 10^2$ | $55.31 \times 10^2$ | $15.03 \times 10^3$ |                     |                     |
| $12.34 \times 10^2$ | $12.34 \times 10^2$ | $20.35 \times 10^2$ | $33.55 \times 10^2$ | $33.55 \times 10^2$ |
| $45.40 \times 10^1$ |                     |                     |                     |                     |
| $16.70 \times 10^1$ | $27.54 \times 10^1$ | $27.54 \times 10^1$ | $27.54 \times 10^1$ |                     |
| 61.44               |                     |                     |                     |                     |
| 22.60               | 22.60               | 22.60               | 22.60               | 22.60               |

With these energy group structures, the feed enrichment and the breeding ratio varied less than 0.8%. The errors obtained using the single collapse spectrum are shown in Table I.A.3. The comparisons are made relative to the 13-group results. The fissile mass discharge from the reactor agrees well with the 13-group results, as does the core-discharge fissile mass (not shown). In the blanket, however, larger errors can accrue. The blanket <sup>239</sup>Pu discharge, of which the blanket fissile mass is mainly composed, compares favorably with the 13-group results. However, note the large errors in the <sup>241</sup>Pu blanket discharge. These errors are due to the hardness of the core spectrum used for collapsing relative

\*Murphy, P. M., et al., GEAP-5618 (1968).

\*\*Toppel, B. J., et al., ANL-7318 (June 1967).

to the blanket spectrum. This causes an underestimate of the  $^{239}\text{Pu}$  capture rate in the blankets, which is the source of the  $^{241}\text{Pu}$ .

TABLE I.A.3. Errors Using Single Collapse Spectrum

| Discharge      | Errors (%) |          |          |
|----------------|------------|----------|----------|
|                | 8 Groups   | 7 Groups | 6 Groups |
| Fissile Mass   | 0.1        | 0.4      | 0.6      |
| Blanket Pu-239 | 0.5        | 0.8      | 1.3      |
| Blanket Pu-241 | 4.0        | 10.0     | 20.0     |

By means of the region-dependent collapse, these spectral effects can be accounted for and the accuracy can be significantly increased. The results for 6 groups and 4 groups are shown in Table I.A.4. Note the significantly smaller errors. With region-dependent collapsing, fuel-cycle parameters can be calculated accurately with four neutron energy groups.

TABLE I.A.4. Errors Using Region-dependent Collapse Spectrum

| Discharge      | Errors (%) |          |
|----------------|------------|----------|
|                | 6 Groups   | 4 Groups |
| Fissile Mass   | 0.01       | 0.1      |
| Blanket Pu-239 | 0.01       | 0.1      |
| Blanket Pu-241 | 0.02       | 0.2      |

The conclusion from this study is that region-dependent collapsing can significantly decrease the errors in fuel-cycle calculations. For designs typical of those studied, in which the spectrum does not change markedly between the core and blanket, fuel-cycle calculations with eight neutron energy groups and a single collapse spectrum yield good accuracy for the feed enrichment, breeding ratio, and fissile mass discharge. With region-dependent collapse, four neutron energy groups yield good accuracy.

(iii) Reactor Dynamics (D. A. Meneley and E. L. Fuller)

Last Reported: ANL-7661, pp. 1-3 (Jan 1970).

(a) QX1--Startup Transient Case. The following summarizes one more problem in the continuing series designed to test and demonstrate the capabilities of the QX1 code and to study the importance of spatial kinetics to the analysis of LMFBR's. The case is the same as the

one outlined in Progress Report for October 1969, ANL-7632, pp. 1-2, except that the initial reactivity was set to  $-\beta$  by artificial reduction of the total yield per fission of the critical system. The driving source was computed from the spontaneous fission decay rate of Pu-240 in the system. The same rate of sodium removal as in the original problem was assumed to initiate the transient.

The behavior of the amplitude function is shown in Fig. I.A.3. Since the initial power is very low, the Doppler feedback terminates the first burst only after a power rise of roughly 12 decades. The maximum rise of fuel temperature at the first power peak is  $345^{\circ}\text{C}$ . Fuel melting begins at 0.084 sec. The maximum instantaneous inverse period during the first power rise is roughly  $3000\text{ sec}^{-1}$ , and the minimum on the first drop is around  $-3000\text{ sec}^{-1}$ . Referral to the integral parameters plotted in Fig. I.A.4 shows that there is no discernible fluctuation in the slow decrease of the prompt-neutron generation time caused by these large values. This shows the insensitivity of the flux shape function in the energy direction to the inverse period term in the shape equation. If the shape was sensitive to this term, the generation time would decrease for positive values and increase for negative values because of spectrum changes. The roughly linear decrease in the generation time results from spectral hardening following sodium removal.

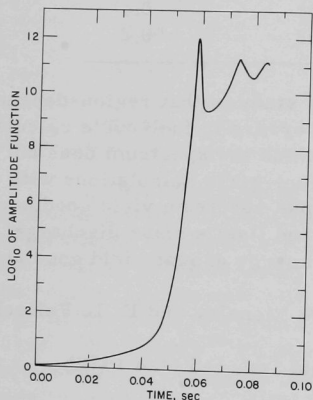


Fig. I.A.3. Amplitude Function after Uniform Voiding at  $t = 0$  of an Initially  $\$1$  Subcritical LMFBF

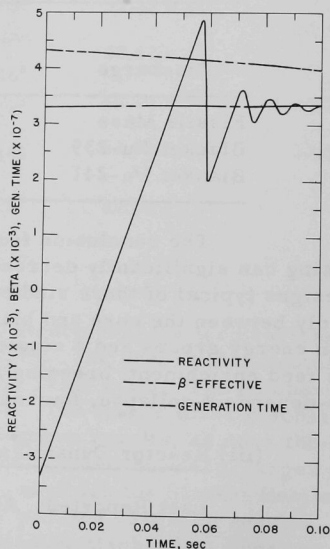


Fig. I.A.4. Response of Integral Parameters in Problem Shown in Fig. I.A.3

The initial reactivity rise in Fig. I.A.4 is almost linear; this test case is for uniform sodium removal, so the flux-shape changes are very small. The first Doppler response is very sharp because of the high rate of energy accumulation; then the reactivity oscillates around prompt critical until a balance is reached between the positive insertion rate and the negative Doppler feedback. If the transient were continued, the power would rise slowly because of the  $1/T$  dependence of the feedback.

b. Fast Critical Experiments--Theoretical Support--Idaho

(i) Supplementary Analytical Interpretation of Integral Data  
(R. G. Palmer)

Last Reported: ANL-7606, pp. 11-12 (Aug 1969).

(a) U-238 In-cell Capture Rates for ZPR-3 Assemblies 53 and 54. Relative U-238 capture rates at eight positions in the central unit cell of ZPR-3 Assemblies 53 and 54 have been determined both theoretically and experimentally. For the experiments, depleted uranium foils were irradiated in the cell locations as shown in Fig. I.A.5. The foils were counted

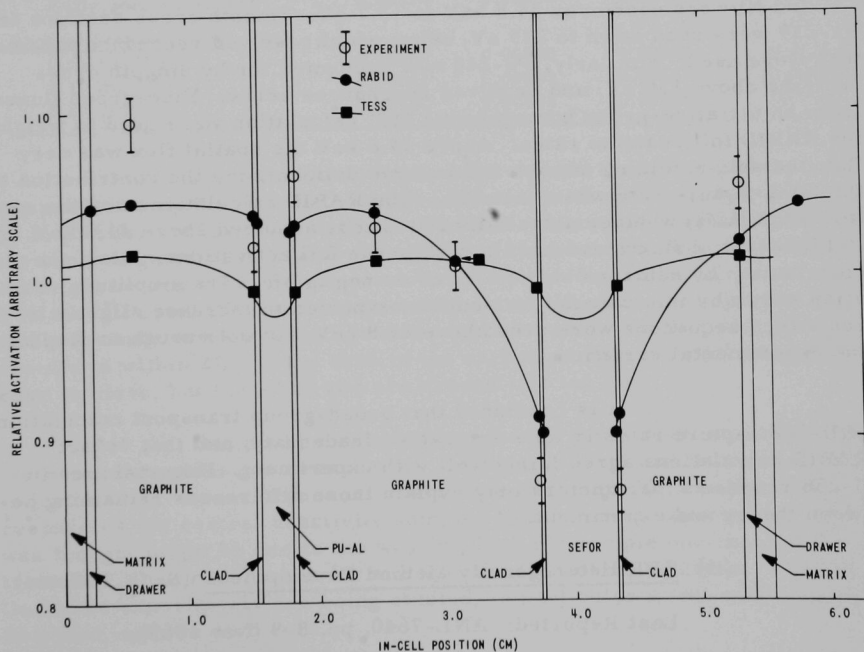


Fig. I.A.5. U-238 In-cell Capture Rates in ZPR-3 Assemblies 53 and 54



by a Ge(Li) gamma-ray spectrometer. The activations were obtained from three gamma rays (energies of 209.8, 228.2, and 277.6 keV) which follow the beta decay of Np-239. The experimental errors of  $\pm 1.5\%$  include a contribution from statistics of  $\pm 0.4\%$ .

Heterogeneously self-shielded, 23-epithermal-group neutron cross sections generated by MC<sup>2</sup> were used by the TESS transport code in a one-dimensional, double S<sub>12</sub> cell calculation. The amplitude variation exhibited by this calculation was clearly too small, because the self-shielding of each foil was inadequately accounted for.

Essentially "exact" calculations of the reaction rates in each foil were obtained from the integral transport code RABID. U-238 capture cross sections in the energy range from 24.8 to 3.35 keV (a span of 8 MC<sup>2</sup> fine groups, each 0.25-lethargy unit wide) were obtained from statistically generated resolved resonance sequences for (*l*, *J*) states of (1/2, 0), (1/2, 1), and (3/2, 1). The Schmidt tabulation was used for both the unresolved and the resolved resonance parameters. The resonance sequences were centered on each MC<sup>2</sup> fine group. Resolved U-238 resonances were used from 3.35 keV down to 13.7 eV. Resolved resonances for Al, Fe, Cr, and Ni were used over 24.8 keV to 13.7 eV. Smooth cross sections for Pu-239 were used down to 275 eV, below which resolved resonance parameters were used. Similarly, Pu-240 was accounted for by smooth cross sections above 130 eV, and resolved resonances below. Fine-group fluxes from an ultrafine-group homogeneous MC<sup>2</sup> calculation were used to weight the RABID foil reaction rates. Above 24.8 keV the spatial flux was very flat, the self-shielding of each foil became uniform, and the contribution to the total capture rate was about 28%. The RABID calculations are the same (to within 0.3%) whether a spatially flat flux is assumed above 24.8 keV, or if TESS spatial fluxes are used to weight the foil activations. Also, the contribution by neutrons below 13.7 eV is negligible. The amplitude variation shown by this calculation would be expected to increase slightly if resonance sequences were used above 24.8 keV, but not enough to display the experimental variation.

It is concluded that broad-group transport calculations of U-238 capture rates in foils are rather inadequate, and that "exact" RABID calculations agree fairly well with experiment. Uncertainties in U-238 resonance parameters may explain those differences remaining between theory and experiment.

(ii) ZPR Heterogeneity Method Development (R. G. Palmer)

Last Reported: ANL-7640, pp. 8-9 (Nov 1969).

Heterogeneity factors, sodium-void effects, and central sample worths have been calculated in GEDANKEN 1 (see Progress Report for August 1969, ANL-7606, pp. 8-10) using various spatial homogenization

procedures. The results are summarized in Table I.A.5. The "exact" results are based on 12-group one-dimensional transport calculations using the TESS code with extrapolations to  $S_\infty$ . The fluxes for the weighting procedures were obtained from S12 calculations for an infinitely repeating unit cell with uniform-group-dependent pseudoabsorption cross sections  $D_g B_g^2$  added. Real flux and bivariate, real, and adjoint flux, weighting homogenizations were then performed and the cross sections used for the whole reactor calculations.

TABLE I.A.5. Results of Various Weighting Procedures on "Experiments" in GEDANKEN 1

|  | "Exact" | Real Weighting | Bivariate Weighting | Volume Weighting |
|--|---------|----------------|---------------------|------------------|
| <u>Heterogeneity Factor, <math>\Delta k/k</math></u> |         |                |                     |                  |
| Normal Core  | 0.00634 | 0.00614        | 0.00554             | -                |
| Half Sodium-voided Core                              | 0.00518 | 0.00501        | 0.00443             | -                |
| Fully Sodium-voided Core                             | 0.00391 | 0.00370        | 0.00334             | -                |
| <u>Sodium-void Effects, <math>\Delta k</math></u>    |         |                |                     |                  |
| Half Sodium-voided                                   | 0.00159 | 0.00156        | 0.00154             | 0.00042          |
| Fully Sodium-voided                                  | 0.00236 | 0.00238        | 0.00213             | 0.00008          |
| <u>Central Sample Worth, <math>\Delta k</math></u>   |         |                |                     |                  |
| 0.01 cm $^{239}\text{Pu}$                            | 0.00567 | 0.00570        | 0.00556             | 0.00563          |
| 0.10 cm $^{238}\text{U}$                             | 0.00665 | 0.00679        | 0.00657             | 0.00654          |
| 0.25 cm $^{12}\text{C}$                              | 0.00183 | 0.00182        | 0.00159             | 0.00161          |

Compared with the "exact" results the heterogeneity factor predicted by the real weighted procedure are about 5% or less, and 12 to 15% for the bivariate method. For the sodium-void reactivity effects the real weighted results are within 2% and the bivariate somewhat higher. As might be expected, the simple volume-weighted results are quite poor. For the  $^{239}\text{Pu}$  and  $^{238}\text{U}$  central reactivity sample the results appear to be fairly insensitive to how the environment is treated, and they all give good results to within 2%. In the case of the carbon sample the real weighted case is close, but the other two are around 12% too low.

One could conclude from these results that the real weighting procedure gives good results for all three aspects and that bivariate is just a little worse. There is no evidence of the 20-30% reactivity discrepancies for central reactivity samples found in real experiments that was thought might be due to the way in which the sample environment is treated. These results are for one specific Gedanken, however. Further Gedanken experiments are being studied, in particular a two-zone, power-flattened, infinite slab core.

## 2. Experimental Reactor Physics

### a. Fast Critical Experiments--Experimental Support--Idaho

#### (i) Neutron-spectrum Measurements (G. G. Simons)

Last Reported: ANL-7640, pp. 10-12 (Nov 1969).

The fast-neutron spectrum (see Fig. I.A.6) was measured at a near-core-center position (1-P-16) in ZPR-3 Assembly 58 using the proportional-counter proton-recoil spectrometer system. A nominal 5/8-in. hydrogen counter and a nominal 15/16-in. methane counter were used to cover the neutron energy range from 0.33 keV to 2.37 MeV.

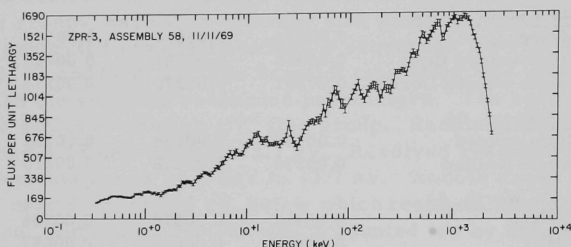


Fig. I.A.6. Neutron Spectrum at Position 1-P-16 in ZPR-3 Assembly 58  
Measured with the Proportional-counter Neutron Spectrometer

The combined neutron- and gamma-radiation level for the critical configuration (see Fig. I.A.7, p. 22, of ANL-7640) with all control and safety rods withdrawn was excessive for proper spectrometer system operation. The loading change required exchanging outer core fuel drawers for reflector drawers until the desired lower flux levels were obtained. For the neutron-spectrum measurement, the core outline was 70 fuel drawers in half one and 69 fuel drawers in half two; all control and safety rods and the neutron source were withdrawn. The reactor was 7%  $\Delta k/k$  subcritical.

The relatively soft neutron spectrum clearly reflects the presence of the iron in the core, especially at approximately 30 and 85 keV, which correspond to two large resonance regions for iron. The flux depression at 750 keV may be the result of the corresponding iron resonance. Likewise, other flux depressions may be attributable to either further iron resonances or resonances for nickel, chromium, and aluminum. It is difficult to evaluate the causes of these flux depressions truly because of the basic overall lack of structure present in the spectrum.

This neutron-spectrum measurement was the last which will be made using the basic spectrometer without pulse-pileup circuitry. The high count-rate system (see Fig. I.B.1, p. 3, Progress Report for March 1969, ANL-7561) will allow data to be accumulated at count rates between 10,000 and 30,000 cps, compared to the 6,000 cps for this measurement.

b. Fast Critical Experiments--Experimental Support--Illinois

(i) Pulsed, Cross-correlation, and Noise Measurements  
(C. E. Cohn)

Last Reported: ANL-7632, pp. 4-5 (Oct 1969).

The circuit\* shown in Fig. I.A.7 will accept either positive or negative pulses of 1 V or larger and shape them into a form suitable for use with RTL computer logic. The output from the circuit will have sharp transitions even if the input pulses have very long rise and fall times.

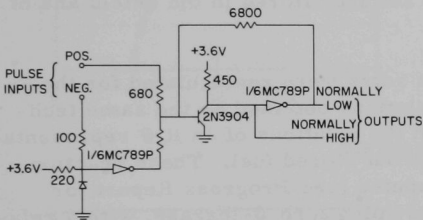


Fig. I.A.7. Universal Pulse Input for RTL Logic

When the pulse terminates, the inverse action will occur. The regenerative loop has enough hysteresis to give sharp, bounce-free transitions.

c. FFTF Critical Assembly Experiments--Planning and Evaluation (A. Travelli)

Last Reported: ANL-7661, pp. 10-11 (Jan 1970).

The results of calculation in diffusion theory of the radial variation of the B-10 capture, U-238 fission, Pu-239 fission, and Na-23 capture rates in the ZPPR/FTR-2 assembly with no fuel stored in the

\*Cohn, C. E., The Electronic Engineer, "IC Ideas," 28, No. 6 91 (1969).

shield have been given (see ANL-7661 and Progress Report for December 1969, ANL-7655, pp. 6-9). The neutron fluxes used in these computations were obtained from a DIFF-2D diffusion-theory solution in R,Z geometry, in which the shield sector was assumed to span over  $360^\circ$ .

The same reaction rates at the same positions using the same cross sections have now been computed for the case of fuel stored in the shield. The neutron fluxes for the reactor were again obtained from a diffusion solution in R,Z geometry. However, in order to simulate the leakage in the direction perpendicular to the plane in which the three radial traverse measurements were made, fictitious  $DB_\theta^2$  absorbers were added at each radial mesh point for all axial values closer to the midplane than the core half-height. The  $B_\theta^2$  values were group-dependent and R-dependent. They were derived from the flux solutions of an R, $\theta$  representation of the reactor and shield sector with stored fuel. Thus the solution of the R,Z problem has meaning only in the plane of the measurements, but includes the effect of the azimuthal finiteness of the fuel stored in the shield and of the shield itself.

For reference, the reaction rates were recalculated for the case of no stored fuel using R,Z flux solutions obtained by the same technique, where the  $B_\theta^2$  were derived from the solutions of an R, $\theta$  representation of the reactor and shield sector without stored fuel. These reaction rates agreed with those previously computed (see Progress Report for December 1969, ANL-7655, pp. 6-9), assuming zero  $\theta$ -leakage, with a relative discrepancy of 7% or less.

In Figures I.A.8 through I.A.19 computed reaction rates are compared on a logarithmic scale with measured values,\* with stored fuel in the upper graph (radial position indicated by dotted lines) and without it in the lower graph.

In Figures I.A.14 and I.A.15 (Pu-239 fission) and I.A.17 and I.A.18 (Na-23 capture) reaction rates computed with core-averaged cross sections differ enough from the rates computed with the radial reflector-averaged cross sections so that labels are provided. In all other traverses through the core the difference is almost indistinguishable. The traverses at an axial position 55.88 cm from the center are through the axial reflector (see ANL-7655, p. 6-9). Here the reaction rates computed with the axial reflector-averaged cross sections are also almost identical with their radial counterpart.

The relatively soft flux components which activate B-10 and Pu-239 are depressed by the presence of stored fuel in the shield. These

\*Progress Report for December 1969, ANL-7655, pp. 29-37; FFTF Monthly Progress Report, pp. 9-16 (Jan 1970).

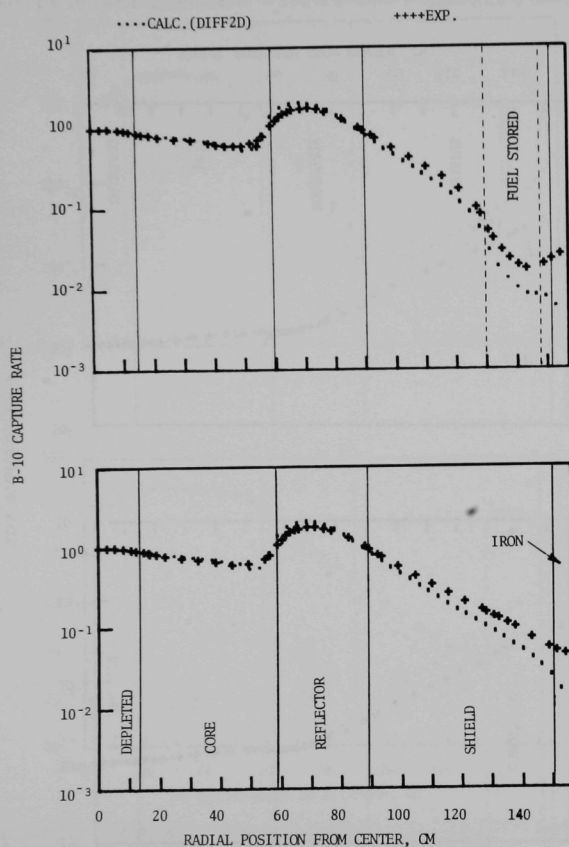


Fig. I.A.8. B-10 Capture Rate vs Radial Position in ZPPR/FTR-2 Shield Configuration at Axial Position 7.62 cm from Center

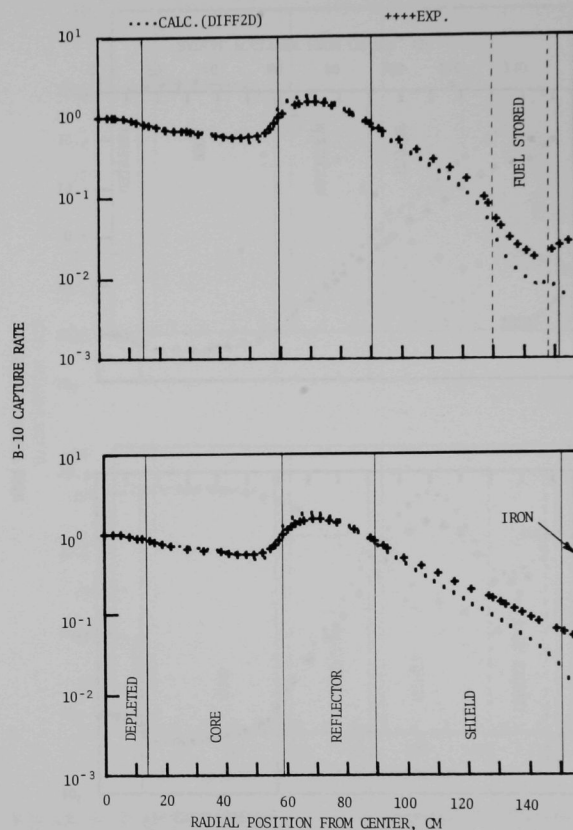


Fig. I.A.9. B-10 Capture Rate vs Radial Position in ZPPR/FTR-2 Shield Configuration at Axial Position 35.56 cm from Center

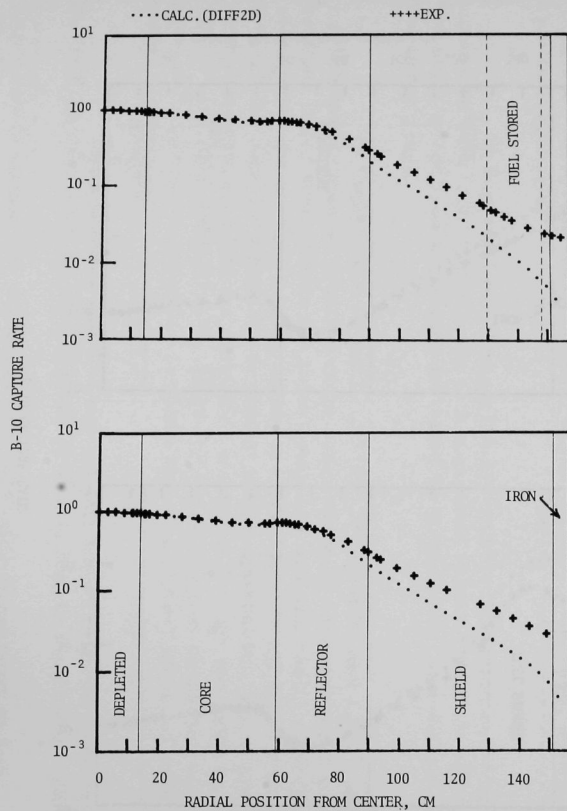


Fig. I.A.10. B-10 Capture Rate vs Radial Position in ZPPR/FTR-2 Shield Configuration at Axial Position 55.88 cm from Center

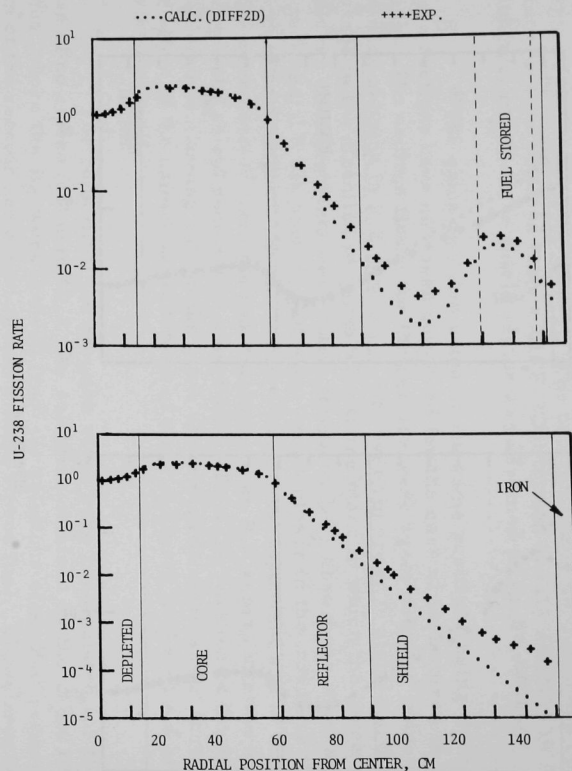


Fig. I.A.11. U-238 Fission Rate vs Radial Position in ZPPR/FTR-2 Shield Configuration at Axial Position 7.62 cm from Center



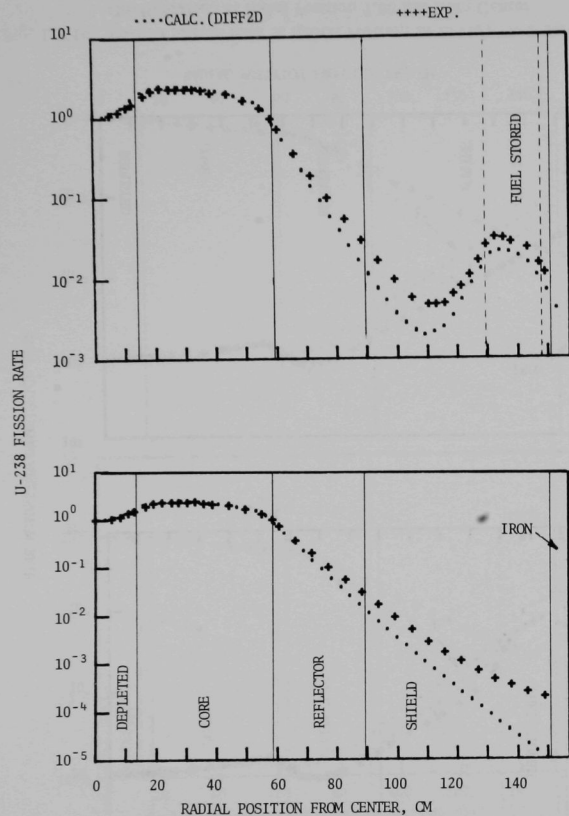


Fig. I.A.12. U-238 Capture Rate vs Radial Position in ZPPR/FTR-2 Shield Configuration at Axial Position 35.56 cm from Center

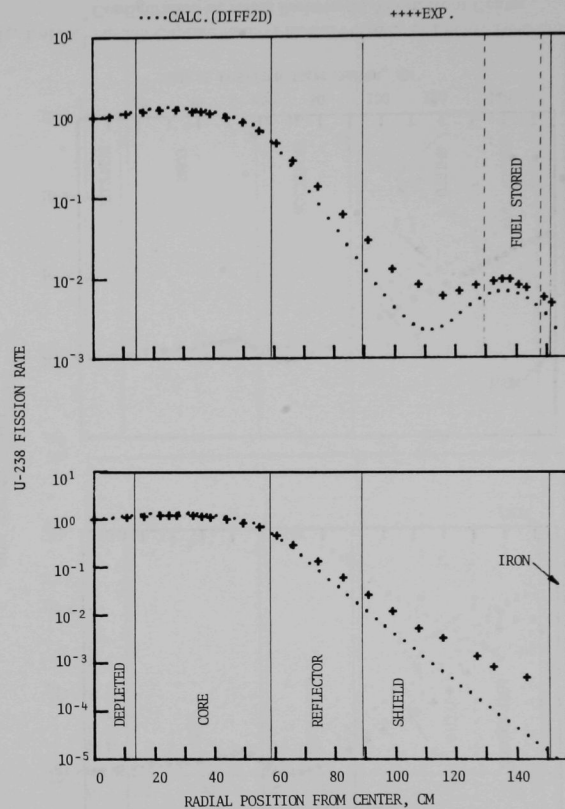


Fig. I.A.13. U-238 Capture Rate vs Radial Position in ZPPR/FTR-2 Shield Configuration at Axial Position 55.88 cm from Center

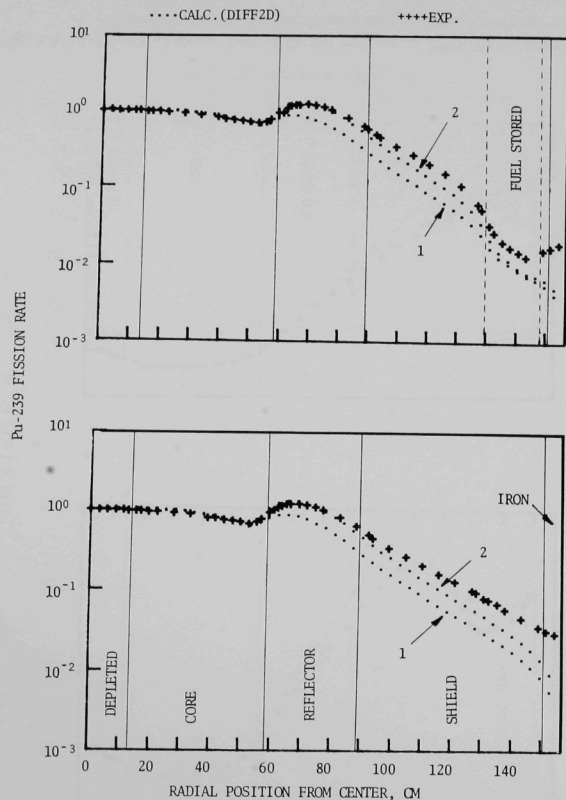


Fig. I.A.14. Pu-239 Fission Rate vs Radial Position in ZPPR/FTR-2 Shield Configuration at Axial Position 7.62 cm from Center

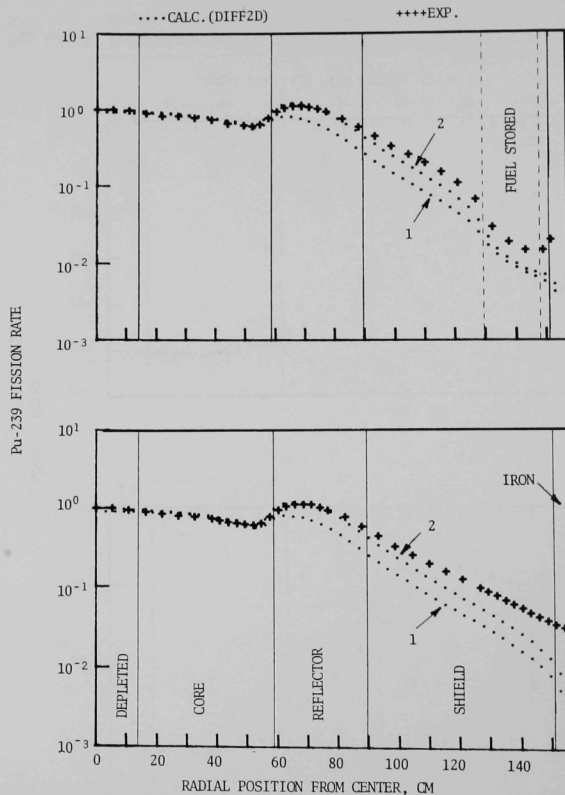


Fig. I.A.15. Pu-239 Capture Rate vs Radial Position in ZPPR/FTR-2 Shield Configuration at Axial Position 35.56 cm from Center

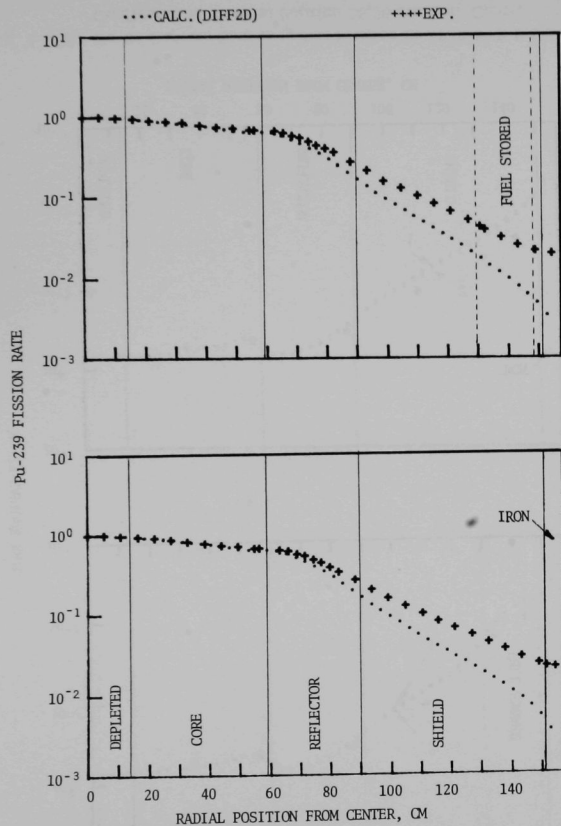


Fig. I.A.16. Pu-239 Capture Rate vs Radial Position in ZPPR/FTR-2 Shield Configuration at Axial Position 55.88 cm from Center

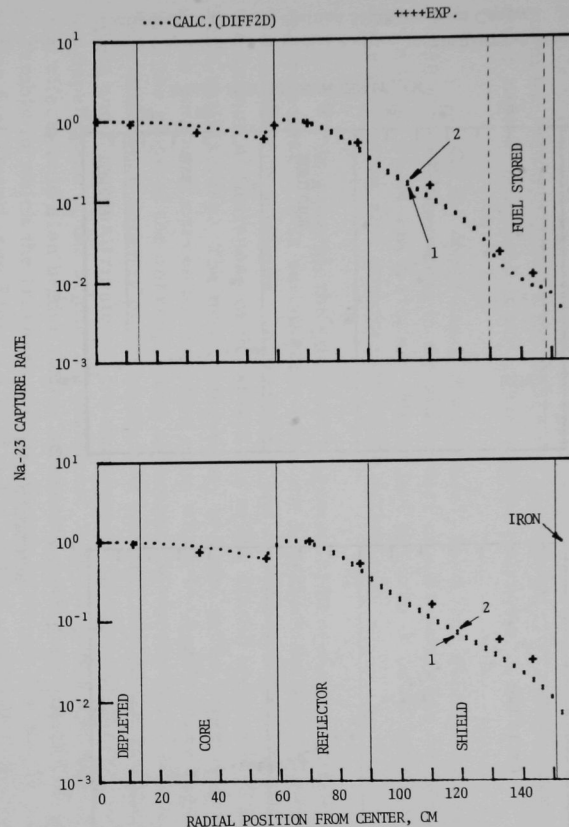


Fig. I.A.17. Na-23 Capture Rate vs Radial Position in ZPPR/FTR-2 Shield Configuration at Axial Position 7.62 cm from Center

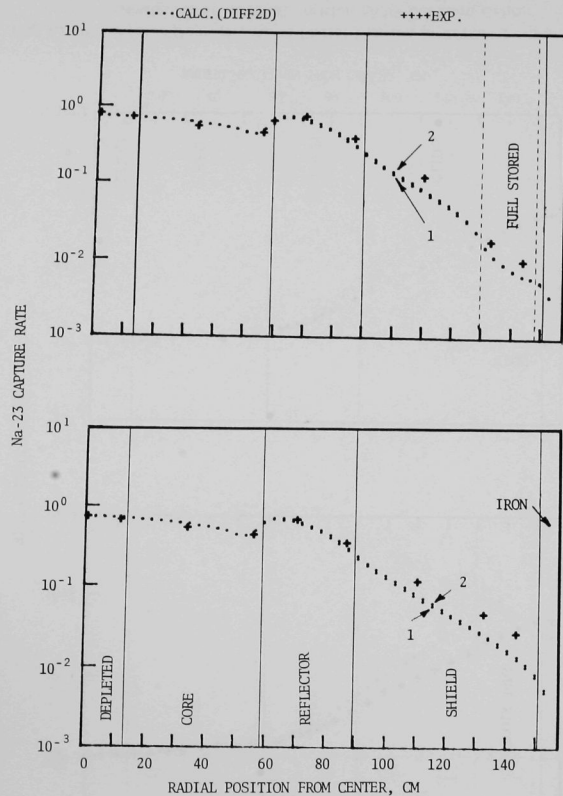


Fig. I.A.18. Na-23 Capture Rate vs Radial Position in ZPPR/FTR-2 Shield Configuration at Axial Position 35.56 cm from Center

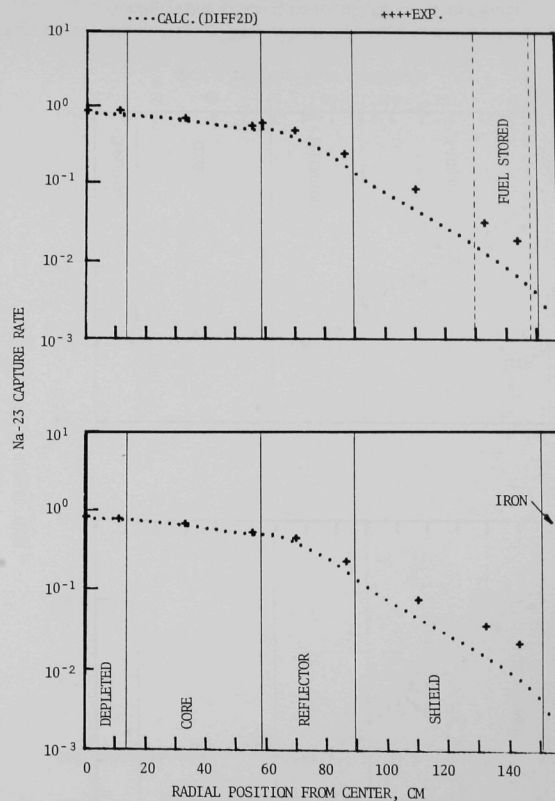


Fig. I.A.19. Na-23 Capture Rate vs Radial Position in ZPPR/FTR-2 Shield Configuration at Axial Position 55.88 cm from Center

depressions do not extend far enough to be seen in the 55.88-cm traverse. Notice that a soft flux component appears to be present (possibly due to room backscatter), which increases the experimental reaction rate at the outer radius, but which is not present in the computation.

On the other hand, the relatively hard flux which activates U-238 shows a maximum in the stored fuel which extends far enough to be seen in the 55.88-cm traverse. Stored fuel has only a small net depressing effect on the flux components which activate Na-23.

In general, the qualitative agreement between calculated and experimental data is satisfactory when one considers the approximate nature of the computations. In particular, the method used to take into account the azimuthal finiteness of the shield and of the stored fuel appears to be quite satisfactory. The main discrepancy is found in the negative gradient of the computed curves for reaction rate, which is usually more negative than the slope of the corresponding experimental curves in the shield region. This difference depends on the particular reaction and on the axial position and may be attributed to the deficiencies of diffusion theory, to angular dependence of the scattering matrices, or to the cross sections used. The effect could also be due to flux streaming down the channel through the assembly in which the traverse tube is placed; however, the Na-23 curves for no fuel stored (see Figs. I.A.17 - I.A.19) seem to contradict this explanation, because there is no channel for streaming in these cases and the effect is still present.

### 3. ZPR-6 and -9 Operations and Analysis

#### a. Clean Critical Experiments (W. Y. Kato and R. A. Karam)

Last Reported: ANL-7655, pp. 9-10 (Dec 1969).

(i) ZPR-6 Assembly 6A. The experiments planned for ZPR-6 Assembly 6A have been completed.

The critical mass of Assembly 6A, corrected for excess reactivity and for the difference in fuel arrangement in the outer region, was 1798 kg. The difference between the fuel arrangement in the inner and outer regions was as follows:  $^{235}\text{U}$  plates, 1/8-in. thick, were used in every other 2- or 3-in. segment of the unit cell of the outer region. Continuous 1/16-in.-thick  $^{235}\text{U}$  fuel columns were used in the inner region. The correction to the fully uniform system with the unit-cell configuration of the inner region was established by determining the relative reactivity between the loading patterns by progressive material substitution in one quadrant and then extrapolating to the full core.

Central reactivity worths of Re, W, Ta,  $^{10}\text{B}$ ,  $^{235}\text{U}$ ,  $^{238}\text{U}$ ,  $^{239}\text{Pu}$ , C, Be, Na, and stainless steel were measured in the "sodium-in" configuration.

The reactivity worths of the core materials were measured in the environment of the core-loading pattern. This measurement comprised the oscillation of two 2 x 2 x 2-in. stainless steel-clad cans, relative to each other, loaded in essentially the same manner as in the core. Additionally, the central reactivity worths of  $^{235}\text{U}$ ,  $^{238}\text{U}$ ,  $^{10}\text{B}$ , Re, W, C, and Be were measured in a 40-cm-radius, sodium-free central region.

The perturbation denominator was measured with a procedure previously described.\* This quantity was also measured with the sodium removed from the central region of 40-cm radius.

The sodium-void coefficient was measured as a function of axial position in sections 6 in. long in the nine central drawers. This coefficient was also measured as a function of radius. In these measurements, sodium-filled cans, extending 7 in. in each half, were replaced with empty cans.

To satisfy the requirement that the true plate- and cell-averaged values of the ratio of  $^{238}\text{U}$  fission and capture to  $^{235}\text{U}$  fission be established over the total core and blanket, foil measurements were made at the following locations:

\*Karam, R. A., Nucl. Sci. Eng. 37, 192 (1969).

- a. core center (1/16-in. enriched unit cell),
- b. core-reflector radial interface (1/16-in. enriched unit cell),
- c. one drawer from radial interface (1/16-in. enriched unit cell),
- d. regions III and IV (1/8-in. enriched unit cell),
- e. 2 in. in radial reflector,
- f. axial reflector interface,
- g. 2 in. from axial interface into the core,
- h. 2 in. in axial reflector, and
- i. corner of core where axial and radial reflectors meet.

Reaction-rate traverses for linking the spatial dependence of the unit-cell reaction rates measured at the specific points described above were measured at two positions within the unit cell: (1) between one  $\text{U}_3\text{O}_8$  and the adjacent sodium can and, (2) between the  $^{238}\text{U}$  and  $^{235}\text{U}$  plates. The fission and capture rates in  $^{238}\text{U}$  were measured at the first position, and the same reaction rates in  $^{238}\text{U}$  and fission rates in  $^{235}\text{U}$  were measured at the second position. These reaction rates were measured at the mid-plane every 6 in. along the horizontal radius and at the core-reflector interface of the 45° radius. Additionally, these rates were determined every 6 in. along the axial dimensions.

Axial traverses with  $^{238}\text{U}$  and  $^{235}\text{U}$  for the purpose of extracting material buckling were made every 1/2 in. Radial traverses were made at two positions in every drawer. These were carried through the blanket. The  $^{238}\text{U}$  fission rate was measured as a function of plate position. Additionally, reaction rates indicative of the distribution of resonance neutrons were measured by manganese activation within the  $^{238}\text{U}$  plate and across the unit cell.

All data are being processed and analyzed.

b. Mockup Experiments (J. W. Daughtry)

Last Reported: ANL-7661, pp. 15-16 (Jan 1970).

(i) Correction of Incorrectly Reported Drawer Loading. The drawer loading patterns for FTR-3 (ZPR-9 Assembly 26) were reported in the Progress Report for December 1969, ANL-7655, pp. 10-13. The

loading pattern for the inner-core, Type-A drawers, shown as Fig. I.A.10, p. 11, is incorrect. The correct loading pattern is given in Fig. I.A.20.

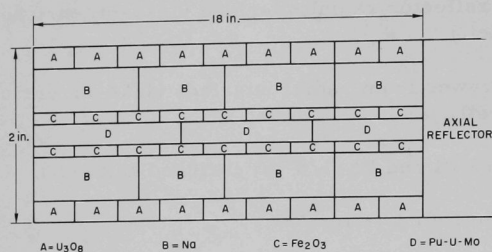


Fig. I.A.20  
Loading Pattern for Inner-  
core Drawer-type A

(ii) Adjustments of FTR-3 Radial Reflector. Following the initial criticality of FTR-3, 128 tubes of radial-reflector material were removed from the outer edge of the assembly. As used here, a tube of material is  $2 \times 2 \times 60$  in., i.e., the contents of a matrix tube extending through both halves of the reactor. The nickel from these 128 tubes, approximately 2680 kg, was shipped to Idaho to be used for an EBR-II critical experiment with ZPR-3.

The resulting FTR-3 configuration (see Fig. I.A.21) was subcritical. In order to achieve criticality again without modifying the fuel or peripheral boron control zones, drawers containing stainless steel and sodium were added around the periphery of the radial reflector. A total of 224 tubes of this type were added, giving the matrix loading pattern shown in Fig. I.A.22. The atom densities in this outer region containing

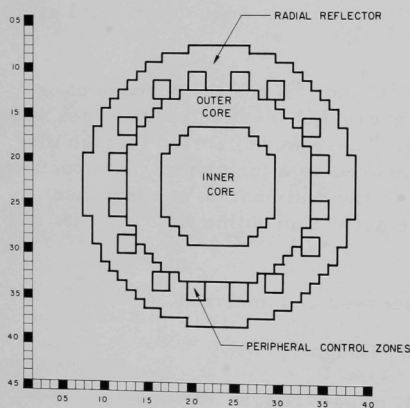


Fig. I.A.21. Subcritical FTR-3 Configuration due  
to Partial Removal of Radial Reflector

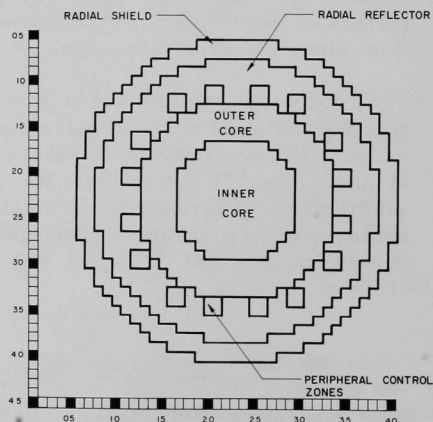


Fig. I.A.22. New FTR-3 Reference  
Configuration



stainless steel and sodium (hereafter, referred to as the radial shield) are given in Table I.A.6. The inner ring of the radial shield, consisting of 128 tubes, is loaded as shown in Fig. I.A.23, which is identical to the radial reflector loading pattern except that the nickel has been replaced by stainless steel. The outer ring of the radial shield, consisting of 96 tubes, is loaded as shown in Fig. I.A.24. The drawers in the outer ring were loaded differently only because there was an insufficient inventory of stainless steel of the sizes required to load the entire radial shield like Fig. I.A.23.

TABLE I.A.6. Atom Densities in the Radial Shield

| Element | $10^{21}$ atoms/cm <sup>3</sup> | Element | $10^{21}$ atoms/cm <sup>3</sup> |
|---------|---------------------------------|---------|---------------------------------|
| Na      | 6.754                           | Mn      | 0.827                           |
| Fe      | 39.022                          | C       | 0.105                           |
| Cr      | 11.258                          | Mo      | 0.036                           |
| Ni      | 5.372                           |         |                                 |

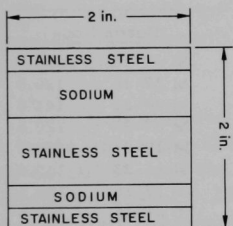


Fig. I.A.23. Loading Pattern for Radial Shield--Inner Ring

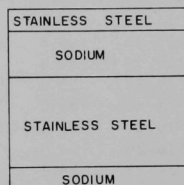


Fig. I.A.24. Loading Pattern for Radial Shield--Outer Ring

The outer radius of the radial reflector is now 85.4 cm; the outer radius of the radial shield is 97.4 cm. The axial height of the radial shield is 154.4 cm, the same as the radial reflector. The matrix loading pattern as shown in Fig. I.A.22 is the new reference configuration for the FTR-3 critical experiments program.

(iii) Measurement of Central Neutron Spectrum. The neutron-spectrum measurement was scheduled early in the program of experiments so that the gamma-ray background would be as low as possible. The measurement was made near the center of the assembly using the proton-recoil counter technique. It was necessary to have the reactor in a sub-critical state due to the excessively high count rates that one would have with the reactor critical. The spectrum measurement was made with the reactor configuration as shown in Fig. I.A.21. All ten boron rods were fully inserted, and nine of the ten fuel bearing rods were fully withdrawn. The one fuel-bearing rod at matrix location M 24-23 was left fully

inserted, since it was in the tube adjacent to the proton-recoil counter. Based on subsequent calibrations of all control and safety rods, the reactor was approximately 2.1% (about \$7) subcritical. The results of the measurement are being analyzed and will be reported at a later time.

(iv) Calibrations of Control and Safety Rods. All control and safety rods have been calibrated in the new critical FTR-3 reference configuration. The total worth of the ten fuel-bearing rods and ten boron rods was slightly less than 2%  $\Delta k/k$ . In order to meet the operational requirement that there be at least 2%  $\Delta k/k$  shutdown margin due to rod action, an additional boron safety rod was installed. Table I.A.7 gives the locations of all fuel-bearing and boron rods as well as the measured worth of each rod. The calibrations were done by the inverse kinetics method using an SEL-840 computer on-line.

TABLE I.A.7. Worths of Control and Safety Rods

| Worth  |          |       |        | Worth      |          |        |        |
|--|----------|-------|--------|------------|----------|--------|--------|
| Rod No.  | Location | Ih    | % Δk/k | Rod No.    | Location | Ih     | % Δk/k |
| Fuel Bearing Rods                              |          |       |        | Boron Rods |          |        |        |
| 1  | M 21-21  | 94.5  |        | 1          | M 19-16  | 120.5  |        |
| 2  | M 21-25  | 94.5  |        | 2          | M 27-16  | 120.5  |        |
| 3  | M 24-19  | 88.0  |        | 3          | M 30-23  | 144.0  |        |
| 4  | M 24-23  | 95.0  |        | 4          | M 27-30  | 120.5  |        |
| 5  | M 24-27  | 88.0  |        | 5          | M 19-23  | 120.5  |        |
| 6  | S 16-20  | 81.5  |        | 6          | M 16-23  | 145.0  |        |
| 7  | S 16-26  | 81.5  |        | 7          | S 19-16  | 120.5  |        |
| 8  | S 24-27  | 88.0  |        | 8          | S 27-16  | 120.5  |        |
| 9  | S 30-26  | 81.5  |        | 9          | S 30-23  | 144.0  |        |
| 10   | S 30-19  | 76.5  |        | 10         | S 27-30  | 120.5  |        |
|  |          |       |        | 11         | S 19-30  | 120.5  |        |
| Total  |          | 869.0 | 0.817  | Total      |          | 1397.0 | 1.313  |
| Total for all rods: Ih--2266.0; % Δk/k--2.130. |          |       |        |            |          |        |        |

#### 4. ZPR-3 and ZPPR Operations and Analysis

##### a. Clean Critical Experiments

Last Reported: ANL-7661, pp. 16-20 (Jan 1970).

##### (i) Integral Measurement of $^{239}\text{Pu}$ Alpha (P. I. Amundson and W. Y. Kato)

Assembly 57 of ZPR-3 (see Progress Report for June 1969, ANL-7581, pp. 8-11) was built on ZPR-3 in order to irradiate at its center, a small sample of highly purified  $^{239}\text{Pu}$  and measure the capture-to-fission ratio. The captures in  $^{239}\text{Pu}$  were measured using mass-spectrometric techniques, whereas the fissions were determined by measuring the activity of the  $^{140}\text{Ba}$  fission product.

The total number of fissions occurring in a  $^{239}\text{Pu}$  sample during the long irradiation was determined by measuring the gamma activity of  $^{140}\text{Ba}$  by gamma spectrometry. Calibration of the  $^{140}\text{Ba}$  gamma activity was accomplished by irradiating nanogram amounts of plutonium in contact with mica fission-track recorders and milligram amounts of plutonium for  $^{140}\text{Ba}$ -activity determination in a shorter irradiation in the same assembly. The total number of plutonium fissions occurring during the short irradiation was determined by counting the fission tracks in the mica track recorders. The ratio of the specific  $^{140}\text{Ba}$  activities between the short- and long-term irradiations and the absolute number of fissions from the track recorders resulted in  $331 \pm 5$  and  $344 \pm 5$  fissions per  $10^9$   $^{239}\text{Pu}$  atoms for two samples in the long irradiation.

The total number of captures occurring in the  $^{239}\text{Pu}$  samples was determined by measuring the  $^{240}\text{Pu}/^{239}\text{Pu}$  atom ratio for both irradiated and control samples of the highly purified, low- $^{240}\text{Pu}$  sample using a tandem mass spectrometer. Unirradiated or control  $^{239}\text{Pu}$  samples; a value of  $25 \pm 4$  ppb of  $^{240}\text{Pu}$  was obtained. Two irradiated samples gave values of  $142 \pm 7$  and  $153 \pm 7$  ppb  $^{240}\text{Pu}$  atoms corresponding to the two fission samples. This results in a value of  $0.363 \pm 0.024$  for  $^{239}\text{Pu}$  alpha (capture-to-fission ratio).

Calculations of the alpha value of  $^{239}\text{Pu}$  for this experiment have been made using the ENDF/B differential cross-section data above 25 keV and ENDF/B, and the data of Gwin and of Schomberg between 0.1 and 25 keV. Alpha values of 0.283, 0.325, and 0.408 were obtained using a theoretically calculated spectrum and the ENDF/B, Gwin, and Schomberg data, respectively. If the time-of-flight measured spectrum is used instead of the theoretical spectrum, the theoretical alpha values become 0.264, 0.303, and 0.370. In order to get agreement with the experimentally measured central integral alpha value of  $0.363 \pm 0.024$ , it appears necessary to use differential alpha values greater than the Gwin data but lower than the Schomberg values in the energy range from 0.1 to 25 keV.

#### (ii) Assembly 59 (P. I. Amundson)

Analysis of the experiments with Assembly 59 has been completed. The results of the perturbation traverses for the Pu-239 annulus are shown in Table I.A.8.

Perturbation traverses with a Cf-252 source were made at two power levels, 8 and 50 W. The differences of the two results for a given position gives the worth of the prompt neutrons at a certain power level to be inferred. All the results were normalized to the count rate for a 108.9- $\mu\text{g}$  Pu-239 foil in a back-to-back fission chamber, placed 2 in. back from the assembly interface in position 2-P-16. The results are shown in

Table I.A.9. Foil-activation measurements should enable this count rate to be converted to a fission rate near a fuel plate at the center of the reactor.

TABLE I.A.8. Pu-239 Perturbation Traverses  
for ZPR-3 Assembly 59a,b

| Radial          |                   | Axial                       |                   |
|-----------------|-------------------|-----------------------------|-------------------|
| Position        | Ih                | Position (in.) <sup>c</sup> | Ih                |
| P20             | $2.054 \pm 0.016$ | -10.06                      | $1.646 \pm 0.028$ |
| P19             | $3.110 \pm 0.043$ | -9.06                       | $2.209 \pm 0.019$ |
| P18             | $4.168 \pm 0.016$ | -8.06                       | $2.709 \pm 0.024$ |
| P17/18          | $4.546 \pm 0.032$ | -7.06                       | $3.264 \pm 0.032$ |
| P17             | $4.964 \pm 0.019$ | -6.06                       | $3.687 \pm 0.024$ |
| P16/17          | $5.090 \pm 0.020$ | -5.06                       | $4.094 \pm 0.026$ |
| P16             | $5.225 \pm 0.014$ | -4.06                       | $4.457 \pm 0.021$ |
| P15/16          | $5.083 \pm 0.024$ | -3.06                       | $4.775 \pm 0.025$ |
| P15             | $4.963 \pm 0.020$ | -2.06                       | $5.020 \pm 0.021$ |
| P14/15          | $4.590 \pm 0.026$ | -1.03                       | $5.155 \pm 0.030$ |
| P14             | $4.203 \pm 0.030$ | 0                           | $5.193 \pm 0.014$ |
| P13/14          | $3.652 \pm 0.026$ | 1.00                        | $5.187 \pm 0.020$ |
| P13             | $3.110 \pm 0.015$ | 2.00                        | $5.058 \pm 0.030$ |
| P12/13          | $2.533 \pm 0.020$ | 3.00                        | $4.834 \pm 0.025$ |
| P12             | $1.996 \pm 0.031$ | 4.00                        | $4.504 \pm 0.058$ |
| P11/12          | $1.564 \pm 0.028$ | 5.00                        | $4.074 \pm 0.027$ |
| P11             | $1.139 \pm 0.035$ | 6.00                        | $3.603 \pm 0.021$ |
| P10/11          | $0.920 \pm 0.036$ | 7.00                        | $3.196 \pm 0.044$ |
| P10             | $0.669 \pm 0.028$ | 8.00                        | $2.635 \pm 0.028$ |
| P9              | $0.377 \pm 0.021$ | 9.00                        | $2.106 \pm 0.025$ |
| P8 <sup>d</sup> | $0.239 \pm 0.026$ | 10.00                       | $1.572 \pm 0.023$ |
| P7 <sup>d</sup> | $0.076 \pm 0.039$ | 11.00                       | $1.157 \pm 0.043$ |
|                 |                   | 13.00                       | $0.764 \pm 0.028$ |
|                 |                   | 15.00                       | $0.450 \pm 0.028$ |
|                 |                   | 17.00                       | $0.184 \pm 0.036$ |

<sup>a</sup>Pu-239 0.010-in. annulus used.

<sup>b</sup>Errors quoted are standard errors calculated from spread of perturbation results.

<sup>c</sup>Positive numbers are into Half 1. Center is 1.03 in. into Half 1 from interface.

<sup>d</sup>Positions P8 and P7 were centered 0.25 in. in towards the core from the true cell center.

TABLE I.A.9. Cf-252 Source Perturbation Traverses  
for ZPR-3 Assembly 59a,b,c

| Radial   |               | Axial                       |               |
|----------|---------------|-----------------------------|---------------|
| Position | Ih            | Position (in.) <sup>d</sup> | Ih            |
| P20/21   | 4.937 ± 0.020 | -10.06                      | 5.112 ± 0.026 |
| P20      | 5.950 ± 0.045 | -9.06                       | 6.004 ± 0.023 |
| P19/20   | 6.656 ± 0.040 | -8.06                       | 6.795 ± 0.026 |
| P19      | 7.579 ± 0.034 | -7.06                       | 7.447 ± 0.035 |
| P18/19   | 8.106 ± 0.023 | -6.06                       | 8.134 ± 0.036 |
| P18      | 8.702 ± 0.019 | -5.06                       | 8.590 ± 0.024 |
| P17      | 9.589 ± 0.056 | -4.06                       | 8.997 ± 0.029 |
| P16      | 9.833 ± 0.014 | -2.06                       | 9.550 ± 0.027 |
| P15      | 9.578 ± 0.035 | 0                           | 9.748 ± 0.022 |
| P14      | 8.746 ± 0.034 | +2.00                       | 9.583 ± 0.026 |
| P13/14   | 8.047 ± 0.023 | +4.00                       | 9.076 ± 0.023 |
| P13      | 7.439 ± 0.022 | +5.00                       | 8.678 ± 0.024 |
| P12/13   | 6.649 ± 0.028 | +6.00                       | 8.158 ± 0.030 |
| P12      | 5.865 ± 0.032 | +7.00                       | 7.533 ± 0.031 |
| P11/12   | 4.928 ± 0.036 | +8.00                       | 6.865 ± 0.025 |
|          |               | +9.00                       | 6.128 ± 0.023 |
|          |               | +10.00                      | 5.250 ± 0.027 |

<sup>a</sup>All results at a power such that Pu-239 (94.4 wt % Pu-239, 108.9  $\mu$ g) foil in back-to-back chamber, 2 in. from the reactor interface in 2-P-16 undergoes 632.1 fissions/sec.

<sup>b</sup>Source strength

for radial results (Jan. 2, 1970) =  $5.955 \times 10^7$  n/sec

for axial results (Jan. 7, 1970) =  $5.933 \times 10^7$  n/sec.

<sup>c</sup>Errors quoted are standard errors calculated from spread of perturbation results.

<sup>d</sup>Positive numbers are into Half 1. Center is 1.03 in. in Half 1 from interface.

Central perturbation measurements were made with samples in two environments. The standard environment was the same as that used in Assembly 58 (see Fig. I.A.19, p. 15, Monthly Report for December 1969, ANL-7655). A voided environment (see Fig. I.A.25) was also used. The results for Assemblies 58 and 59 are given in Table I.A.10, and the ratios in Table I.A.11. The design calculations indicated central perturbation worths for both assemblies to be approximately 20% higher than the measured values for U-235 and Pu-239, and approximately 30% higher compared with the 0.1-in.-dia U-238 cylinder and the 0.06-in.-dia cylinder

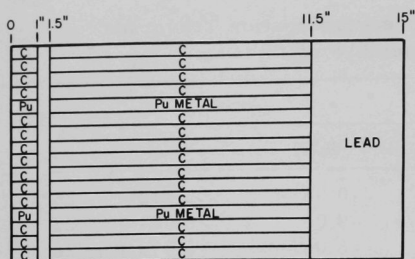


Fig. I.A.25. Half-inch Voided Drawer  
for Central Perturbations

graphite-modified spectrum, the other sampling an average cell spectrum, show the dependence of the results on the environment.

TABLE I.A.10. Central Perturbation Results for  
ZPR-3 Assemblies 58 and 59 (Ih/kg)

| Sample                   | Mass<br>(g) | 58 Standard      | 59 Standard      | 59 Void          |
|--------------------------|-------------|------------------|------------------|------------------|
| Pu-239 annulus 0.010 in. | 4.801       | 875.7 $\pm$ 1.7  | 1100 $\pm$ 3     | 1025 $\pm$ 3     |
| Pu-239 annulus 0.007 in. | 2.761       | 862.0 $\pm$ 2.9  | 1076 $\pm$ 7     | 1007 $\pm$ 5     |
| U-235 annulus 0.010 in.  | 7.128       | 566.4 $\pm$ 1.6  | 709.0 $\pm$ 2.8  | 665.0 $\pm$ 2.2  |
| U-235 annulus 0.005 in.  | 3.638       | 552.4 $\pm$ 1.1  | 691.0 $\pm$ 3.6  | 653.1 $\pm$ 5.5  |
| U-235 annulus 0.003 in.  | 2.327       | 554.0 $\pm$ 3.4  | 696.6 $\pm$ 4.6  | -                |
| U-238 cyl. 0.42 in. dia  | 85.76       | -54.8 $\pm$ 0.1  | -61.3 $\pm$ 0.2  | -65.0 $\pm$ 0.2  |
| U-238 cyl. 0.20 in. dia  | 19.63       | -72.0 $\pm$ 0.5  | -82.0 $\pm$ 1.3  | -85.4 $\pm$ 0.7  |
| U-238 cyl. 0.10 in. dia  | 4.908       | -88.3 $\pm$ 2.0  | -104.1 $\pm$ 2.9 | -108.6 $\pm$ 4.3 |
| B-10 cyl. 0.06 in. dia   | 0.0988      | -39710 $\pm$ 110 | -49230 $\pm$ 180 | -48710 $\pm$ 190 |
| C cyl. 0.4 in. dia       | 6.910       | -                | 333.4 $\pm$ 3.2  | 319.2 $\pm$ 1.9  |
| Pb cyl. 0.4 in. dia      | 51.36       | -                | -                | 6.9 $\pm$ 0.3    |
| S.S. cyl. 0.4 in. dia    | 35.90       | -                | -                | 4.9 $\pm$ 0.6    |
| Ta annulus 0.005 in.     | 3.300       | -                | -                | -1205 $\pm$ 5    |
| Ta annulus 0.003 in.     | 1.888       | -                | -1322 $\pm$ 13   | -1302 $\pm$ 6    |
| Ta annulus 0.002 in.     | 1.317       | -                | -                | -1374 $\pm$ 8    |

Notes: a) Errors quoted are standard errors calculated from spread of inhour determinations. Not included are errors in sample masses.

b) All samples are 2 in. long. The annuli have outside diameters of approximately 0.40 in.

c) Sample compositions--

Pu-239--98.78 wt % Pu; 95.05 wt % Pu-239, 4.50 wt % Pu-240, 0.45 wt % Pu-241

U-235--0.010 in. annulus 93.20 wt % U-235, others 93.10 wt % U-235

U-238--0.21 wt % U-235

B-10--92.8 wt % boron, 92.1 wt % B-10 in boron

Others--No significant contaminants.

of B-10. This latter discrepancy will be reduced when the experimental results are corrected to zero sample size. The ratios of perturbations for U-235, Pu-239, and B-10 in the two standard environments are constant, but higher than those for the U-238 samples. This same difference, about 5% in the same direction, was observed for zero-size samples in the design calculations. The differences between the two environments in Assembly 59, one sampling a

TABLE I.A.11. Central Perturbation Ratios for ZPR-3  
Assemblies 58 and 59

| Sample            | Assembly 59 Standard | Assembly 59 Void     |
|-------------------|----------------------|----------------------|
|                   | Assembly 58 Standard | Assembly 59 Standard |
| Pu-239 annulus    |                      |                      |
| 0.010 in.         | $1.256 \pm 0.004$    | $0.932 \pm 0.004$    |
| Pu-239 annulus    |                      |                      |
| 0.007 in.         | $1.248 \pm 0.010$    | $0.936 \pm 0.009$    |
| U-235 annulus     |                      |                      |
| 0.010 in.         | $1.252 \pm 0.006$    | $0.938 \pm 0.005$    |
| U-235 annulus     |                      |                      |
| 0.005 in.         | $1.251 \pm 0.006$    | $0.945 \pm 0.009$    |
| U-235 annulus     |                      |                      |
| 0.003 in.         | $1.257 \pm 0.012$    | -                    |
| U-238 cylinder    |                      |                      |
| 0.42 in. diameter | $1.118 \pm 0.004$    | $1.060 \pm 0.004$    |
| U-238 cylinder    |                      |                      |
| 0.2 in. diameter  | $1.139 \pm 0.018$    | $1.041 \pm 0.017$    |
| U-238 cylinder    |                      |                      |
| 0.1 in. diameter  | $1.180 \pm 0.044$    | $1.043 \pm 0.049$    |
| B-10 cylinder     |                      |                      |
| 0.06 in. diameter | $1.240 \pm 0.005$    | $0.989 \pm 0.005$    |
| C cylinder        |                      |                      |
| 0.4 in. diameter  | -                    | $0.957 \pm 0.012$    |
| Ta annulus        |                      |                      |
| 0.003 in.         | -                    | $0.985 \pm 0.011$    |

The errors quoted are standard errors calculated from the spread of the perturbation measurements. In the comparison of the standard environments in the two assemblies, systematic errors of 1% from the autorod calibration in each assembly must be added.

A series of substitutions between reactor shutdowns were made in the front of the 1-P-16 core drawer in Assembly 59. The changes in reactivity were determined using control rod 5. Reference loadings (with the plate arrangement in the core drawer to make the substitutions simple) were repeated before and after each experiment, and corrections made for the average change in core temperature. The actual substitutions and the reactivity changes are listed in Table I.A.12. For the last substitution experiment, the replacement of the 2-in. fuel plates by four 1-in. fuel plates, the front 2 in. of each set of substituted core material was loaded into a 2-in. cubic box to prevent movement of the rest of the contents which were loaded in a standard 21-in. drawer. The result for this last substitution was obtained from three measurements with each configuration.



TABLE I.A.12. Central Substitution Experiment for Assembly 59

| Substitution<br>(in 1-P-16)   | Changes in Mass<br>(g) |         | Reactivity<br>(Ih) |
|---|------------------------|---------|--------------------|
| Remove one 2 x 1 x 1/8-in. Pu plate<br>and seven 2 x 1 x 1/8-in. C plates<br>(i.e. front one inch of half a drawer).          | Pu-239                 | -30.64  | $-46.3 \pm 2.0$    |
|   | Pu-240                 | -1.43   |                    |
|   | Pu-241                 | -0.08   |                    |
|   | Al                     | -0.37   |                    |
|   | Steel                  | -9.37   |                    |
|   | Ni                     | -1.2    |                    |
|   | C                      | -40.406 |                    |
| Replace front 2 in. of central col-<br>umn of graphite by 2 x 2 x 1/8-in.<br>B-10 plate (i.e. midway between<br>fuel plates). | B-10                   | +3.1    | $-144.7 \pm 2.0$   |
|   | B-11 (+ impurities)    | +0.5    |                    |
|   | Steel                  | +33.3   |                    |
|   | C                      | -13.1   |                    |
| Replace front 2 in. of central col-<br>umn of graphite by four 1 x 1 x 1/8-<br>in. U-235 plates.                              | U-235                  | +133.77 | $103.4 \pm 2.0$    |
|   | U-238                  | +9.67   |                    |
|   | C                      | -13.1   |                    |
| Replace front 2 in. of central col-<br>umn of graphite by 2 x 2 x 1/8-in.<br>Pu plate.  | Pu-239                 | +65.72  | $77.7 \pm 2.0$     |
|   | Pu-240                 | +3.18   |                    |
|   | Pu-241                 | +0.18   |                    |
|   | Al                     | +0.76   |                    |
|   | Steel                  | +16.77  |                    |
|   | C                      | -13.1   |                    |
| Replace two front 2 x 2 x 1/8-in.<br>Pu-239 plates by four 2 x 1 x 1/8-<br>in. Pu-239 plates (using boxes).                   | Pu-239                 | -9.05   | $-10.0 \pm 0.2$    |
|   | Pu-240                 | -0.44   |                    |
|   | Pu-241                 | -0.01   |                    |
|   | Al                     | -0.07   |                    |
|   | Steel                  | +1.54   |                    |
|   | C                      | +0.08   |                    |

The temperature coefficient of reactivity for a single 6-in. natural  $\text{UO}_2$  sample was measured at the center of Assembly 59. The annular sample had an inner radius 0.16 cm, outer radius 0.63 cm, and a mass of 137.2 g of  $\text{UO}_2$ . The drawer through which the sample passed is shown in Fig. I.A.26. The total worth of the sample, at 22°C, was  $-9.34 \pm 0.09$  Ih. The difference in the worth of the sample as a function of temperature is given in Table I.A.13.

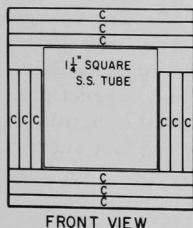


Fig. I.A.26  
Core Drawer for Doppler  
Sample for Assembly 59  
of ZPR-3

(iii) ZPPR Assembly 2. Initial fuel loading has begun for ZPPR Assembly 2, the demonstration-plant critical assembly. The initial loading was 20% of the predicted critical mass of 1205 kg Pu. The predicted critical volume is 2600 liters, divided equally between two zones of core enrichment. Initial criticality is anticipated during the first half of March 1970. Examination of the proposed experimental program, with regard to duration and sequence of experiments, is in progress.



TABLE I.A.13. Reactivity Changes  
of Natural  $\text{UO}_2$  Sample

| Temperature ( $^{\circ}\text{K}$ ) | Reactivity Change (lh) |
|------------------------------------|------------------------|
| 295                                | 0                      |
| 500                                | $-0.994 \pm 0.014$     |
| 800                                | $-1.980 \pm 0.010$     |
| 1099                               | $-2.765 \pm 0.007$     |

Note: Errors quoted are standard errors calculated from the spread of the perturbation measurements only.

b. Doppler Experiments  
(R. Kaiser)

Last Reported: ANL-7655,  
pp. 17-18 (Dec 1969).

The open-loop automatic control system for the ZPPR reactivity Doppler experiment has been checked out. Specifications have been written for SEL 840A computer program to handle data recording and averaging on-line. The preset

accumulator, which controls Doppler-rod oscillation, will also send signals to the computer to control the data-recording process. During the interval that the Doppler rod is in motion, the computer will be asked to average the data just recorded and print the results on the control-room teletype.

A design modification package for axial Doppler drive capability has been sent out for bids.

c. Mockup Critical Experiments (W. P. Keeney and D. Meneghetti)

Last Reported: ANL-7655, pp. 18-42 (Dec 1969).

(i) Description of ZPR-3 Assembly 60. Assembly 60 is the first in the current series of criticals in support of the EBR-II reactor program. This assembly is a version of a homogenized 91-element EBR-II loading in which U-235 is substituted for the plutonium of the oxide elements. The U-235 concentration was further adjusted to produce a critical radius for the succeeding critical, which will contain a partial radial reflector of nickel, close to that of EBR-II, without a change in the composition of the assembly core. The Assembly-60 core-radial blanket boundary is quasi-hexagonal with the radial blanket similar to that of EBR-II. The top and bottom axial reflectors are asymmetric, each consisting of two regions representing a sodium-rich gap and a steel-rich reflector.

The target compositions are listed in Table I.A.14. The detailed zone compositions, which will vary due to piece-size distributions and combinations of different lots of material as well as the control- and safety-rod nonfissile components, are now being calculated for the "as-built" assembly. Typical arrangements of the plates in each reactor zone are shown in Fig. I.A.27.

TABLE I.A.14. Target Compositions for Assembly 60  
of ZPR-3, on EBR-II Critical Mockup

| Core                          |                        |                            |                |      |      |
|-------------------------------|------------------------|----------------------------|----------------|------|------|
| Isotope                       | N (atoms/b-cm)         | Isotope                    | N (atoms/b-cm) |      |      |
| U-235                         | 0.005595               | O                          | 0.002134       |      |      |
| U-238                         | 0.004565               | SS                         | 21.2 vol %     |      |      |
| Na                            | 0.01018                |                            |                |      |      |
| Blanket, Gaps, and Reflectors |                        |                            |                |      |      |
|                               |                        | Target Composition (vol %) |                |      |      |
|                               |                        | (Densities at 22°C)        |                |      |      |
| Zone <sup>a</sup>             | Description            | SS                         | U-238          | Na   | Void |
| R1                            | Upper Gap              | 25.5                       |                | 62.6 | 11.9 |
| R2                            | Top Axial Reflector    | 45.1                       |                | 42.2 | 12.7 |
| R3                            | Lower Gap              | 37.7                       |                | 48.1 | 14.2 |
| R4                            | Bottom Axial Reflector | 52.5                       |                | 36.4 | 11.1 |
| R7                            | Radial Blanket         | 15.8                       | 58.0           | 18.2 | 8.0  |

<sup>a</sup>Zone numbers correspond to Fig. I.A.29.

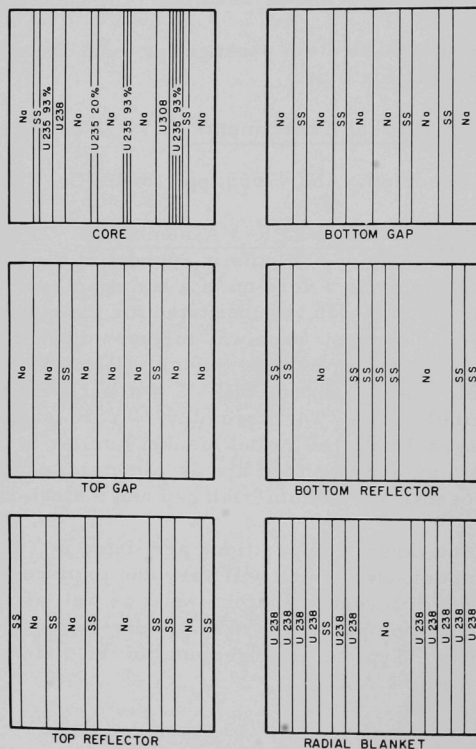


Fig. I.A.27. Plate Arrangement of Typical Zones  
in Assembly 60 of ZPR-3

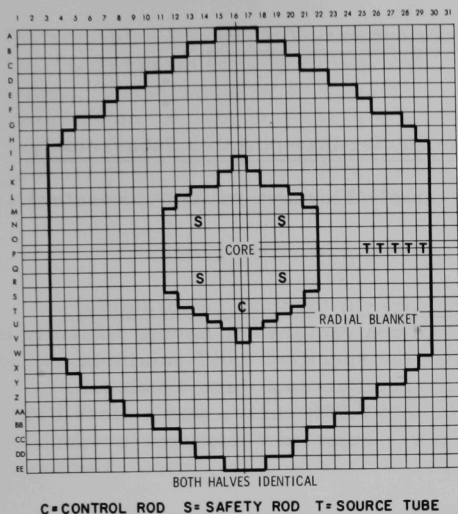


Fig. I.A.28. Reference Core Loading for  
Assembly 60 of ZPR-3

ket for core compositions were made at matrix positions 1- and 2-U-14 and at 1-2-U-18. The worths will be available after analysis of the control-rod data.

(ii) Critical Loading. The critical loading (see Fig. I.A.28) contained 221.93 kg of U-235 and was critical with the control rod in 1-T-16 withdrawn 6.31 in. The excess reactivity of this loading will be reported upon completion of the analysis of the kinetic calibration data of the control rod. The total worth of the eight safety rods was determined to be  $-2.1\% \Delta k/k$ . Figure I.A.29 shows a horizontal section of the assembly. The zone thicknesses are across the flats and are not cylindrical equivalents. Spring-gap positions are not shown as they will be included in the detailed composition descriptions of zones and subzones.

### (iii) Experimental Program.

Edge substitutions of radial blan-

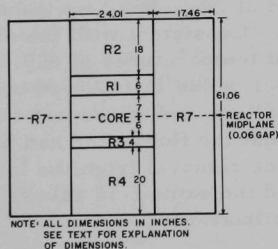


Fig. I.A.29

Horizontal Section of  
Assembly 60 of ZPR-3

Central radial traverses for reaction rate with U-235 and U-238 counters and axial traverses in the P-16 and P-11 matrix positions with U-235, U-238, and B-10 counters have been completed, as well as a scoping irradiation for future neutron activation irradiations.

## B. Component Development--LMFBR

### 1. Instrumentation and Control

#### a. Instrumentation Development for Instrumented Subassembly

##### (i) Instrumented-Subassembly Flowmeters (G. A. Forster)

Last Reported: ANL-7655, p. 43 (Dec 1969).

##### (a) Procurement of Mark-III (Sodium-calibratable) Flowmeters.

Both contractors are having difficulty in obtaining Type 304 stainless steel with the specified 0.06% minimum carbon content. Several years ago, when our specifications were developed, Type 304 stainless steel containing 0.06 to 0.08% carbon was a stock item. Also, experience then indicated that fewer rejected welds were produced in material of higher carbon content.

Better welding techniques are now available. Also, metallurgical processes have improved to the extent that most Type 304 stainless steels contain carbon in the range 0.048-0.06%. Therefore, we have lowered our carbon requirement to 0.045% minimum; below this value the strength of Type 304 stainless steel drops rapidly at temperatures above 1000°F.

(b) Calibration of Mark-III Flowmeters. The Mark-III flowmeter (Serial 010), constructed at ANL, has been successfully calibrated in the Flowmeter Calibration Loop. Consistent with the original test plan, calibration runs were first made at temperatures of 600, 700, and 800°F; then the flowmeter was cooled to below 400°F, followed by repeat runs at 600 and 800°F. Data from the initial run and the repeat runs matched within experimental error, indicating that the flowmeter had been adequately stabilized for use up to 800°F. After removal from the loop, the internal magnetic flux in the flowmeter read the same (710 gauss) as before the calibration runs, again indicating stabilization.

In the coming weeks, magnetic-tape and strip-chart recordings of data will be analyzed to determine the calibration constants for this flowmeter. A Quality Assurance Report covering the materials, fabrication, and assembly of this flowmeter has been completed except for the calibration data.

##### (ii) Fuel-Pin Thermocouples (A. E. Knox)

Last Reported: ANL-7595, pp. 27-28 (July 1969).

##### (a) In-pile Tests in EBR-II Instrumented Subassembly.

Five of the seven fuel-pin thermocouples in the Test II (XX01) EBR-II

Instrumented Subassembly are functioning normally. Thermocouple No. 3 (FCTC 3) has an erratic output, and thermocouple No. 1 (FCTC 1) has no output. Examination of FCTC 3 with a time-domain reflectometer (TDR) revealed an opening in the thermoelements above the thorium-insulated region. FCTC 1 is currently being examined with a TDR in Idaho. Results of these tests and TDR calibrations being performed in Illinois should enable a more exact determination of the failure locations.

(iii) Instrumented-subassembly Coolant Thermocouples  
(A. E. Knox)

Last Reported: ANL-7618, p. 18 (Sept 1969).

(a) Tests of Prototype Coolant and Spacer-wire Thermocouples. Coolant thermocouples are being tested to determine the adequacy of purchase specifications, quality-assurance procedures, and new thermocouple designs.

Eight sheathed Chromel/Alumel thermocouples (two spacer-wire, three outlet, one structural capsule, and two inlet thermocouples) and one sheathed fuel-pin thermocouple lead wire pair (tested as a thermocouple) have been successfully tested out-of-pile. These thermocouples were selected from the lot purchased for instrumented sub-assemblies and represent each type of stainless steel-sheathed thermocouple and lead wire in the Test II (XX01) Instrumented Subassembly for EBR-II. They were constructed by commercial sources to meet ANL specifications and quality-assurance requirements. The nine sensors were insulated with high-purity, high-density crushed alumina and sheathed with Type 304 stainless steel. The Chromel/Alumel thermocouples were made with the highest-accuracy thermoelement material available. The thermoelements in the fuel-pin thermocouple lead wires were Type 308L stainless steel and Alumel.

The sensors were thermally cycled between two simulated EBR-II temperature distributions, with maximum temperatures of 700 and 900°F. Temperature changes were not rapid, with an excursion between the two temperature distributions taking about one hour. Forty-eight temperature excursions were effected in a period of three months. During this period, the measured loop resistance, insulation resistance, and voltage output of each thermocouple remained constant.

This out-of-pile test revealed no gross defect in the stainless steel-clad thermocouples; it also demonstrated the reliability of a relatively new thermocouple construction, i.e., a dual diameter (0.062-in.-OD to 0.040-in.-OD) thermocouple that is spiraled and replaces a 0.040-in.-OD EBR-II fuel-pin spacer wire.

b. FFTF Instrumentation (R. A. Jaross)

(i) In-Core Flowsensor (T. P. Mulcahey)

Last Reported: ANL-7661, p. 23 (Jan 1970).

(a) Permanent Magnet Probe-type Flowsensor (F. Verber)

The specification for commercial procurement of a Type-A flowsensor was reviewed and approved with minor revisions, during a joint RDT/PNL/W/ANL meeting at ANL. After the revisions are made, the procurement package will be forwarded to prospective suppliers for quotations.

In the meantime, tests of prototype Flowsensor A-4 in the CAMEL Loop at sodium temperatures and velocities of interest are being continued. Figure I.B.1 records the sensor operation at 1000°F. Comparison of output signals with those previously recorded at 1000°F reveals very good reproducibility for all sodium velocities; for example, the

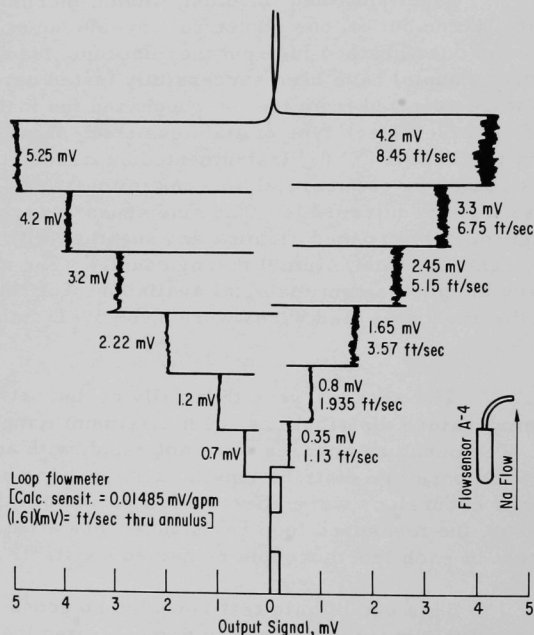


Fig. I.B.1. Test of Permanent-magnet Flowsensor A-4 at 1000°F in the 4-in. Schedule-10 Pipe Test Section of the CAMEL Loop. The magnet was temperature-stabilized at 1300°F for operation at 1200°F.

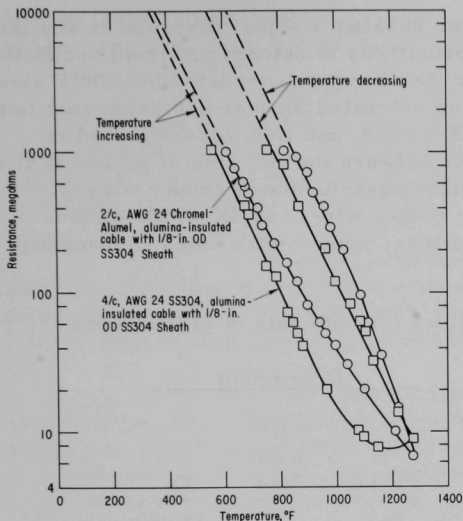


Fig. I.B.2. Effect of Temperature on Insulation Resistance of 1-ft-long Samples of Alumina-insulated, Type 304 Stainless Steel-sheathed, Chromel-Alumel and Type 304 Stainless Steel Cables in an Air Environment

difference between signal outputs at 1.13 ft/sec is 0.07 mV. Thus far, Flowsensor A-4 has been at a temperature of 1000°F, or higher, for a total of 700 hr, with no forced flow during off-work hours.

Measurements of insulation resistance versus temperature in an air environment were made with samples of two, Type 304 stainless steel-sheathed, Alumina-insulated cables. Although limited by the 1000-megohm Megger used, the results (see Fig. I.B.2) illustrate the increase in insulation resistance achieved by expelling water vapor from the cables.

(b) Eddy-current Probe-Type Flowsensors  
(J. Brewer)

Stability tests of Probe No. 9 continue in the CAMEL. Stability tests have been completed in an oven with Probe Nos. 3X-3, 2X-4, and 2X-5. High-temperature (up to 1400°F) oven tests were performed with Probe No. 3X-9.

Recently, the sodium temperature in the CAMEL has been held at 1000°F for 24 hr/day and 7 days/week. The pump was operated 7 hr/day and 5 days/week, with a velocity of 6.44 ft/sec in the annulus about Probe No. 9. Thus 576 hr of continuous operation at 1000°F and 126 hr of flow time have been accumulated. During this time, there has been no measurable deviation in balance or flow sensitivity of Probe No. 9.

Five oven tests each were performed with Probes 3X-3, 2X-4, and 2X-5 to aid in determining the optimum wire size for desired stability. Probes 3X-3 and 2X-5 had heat-treated and pickled bobbins to eliminate magnetic effects. Probe 2X-4 did not have this treatment; therefore, in the stability comparison, only data between 400 and 700°F were used. Also, test No. 1 for each probe was considered a curing cycle, and only data from tests Nos. 2, 3, 4, and 5 were used. Test No. 2 of Probe 2X-4 was not used because the data were questionable.

The quality factor for each probe is determined by

$$Q_f = \frac{\text{Instability in mV (rms)}}{\text{Sensitivity in mV (rms)/ft-sec}} \times 100.$$



Instability is defined as the maximum unbalance signal deviation in any test in the series of tests considered. Sensitivity is determined from oscillating-rig tests; however, sensitivity of Probe 2X-4 was corrected for 400°F since there is a slight magnetic effect from untreated Inconel-600 below that temperature. Similar tests of Probes X-3, X-4, and X-5 were reported in ANL-7661. The important difference between the two sets of probes is that X-3 and X-4 were dry-wound with fiberglass-insulated copper wire, X-5 was dry-wound with heavy Formvar copper wire, and 3X-3, 2X-4, and 2X-5 were wet-wound with heavy Formvar copper wire using Ceramabond 503 ceramic cement.

The quality factors for both sets of probes were

| Wet-wound |                     |       | Dry-wound |                     |       |
|-----------|---------------------|-------|-----------|---------------------|-------|
| Probe     | AWG<br>Wire<br>Size | $Q_f$ | Probe     | AWG<br>Wire<br>Size | $Q_f$ |
| 3X-3      | 26                  | 13.9% | X-3       | 30                  | 13.0% |
| 2X-4      | 24                  | 19.2% | X-4       | 26                  | 22.8% |
| 2X-5      | 20                  | 22.7% | X-5       | 20                  | 51.3% |

Data from one test with 3X-3 looked slightly questionable; had it not been used the  $Q_f$  would have been 8.7%. In general, the results indicate a trend toward more wire turns for a given area for better stability.

The new probe, 3X-9, has an Inconel-625 bobbin and was wet-wound with 15-mil, ceramic-coated, nickel-clad silver wire. After the probe was heated to 1100°F and then cooled, there was a considerable increase in magnetic effect at low temperature. The reason for the increase is not known at this time, but the nickel clad is suspected. This phenomenon will be pursued further.

It is planned to investigate Inconel-600 further since this material will be used with gold-wire coils in the next probe to be tested in the CAMEL or CCTL.

(ii) Gas Disengagement for Failed-fuel Monitoring (E. S. Sowa)

(a) Tests of Gas Disengagement

Last Reported: ANL-7661, pp. 23-24 (Jan 1970).

Two additional tests were made with the Failed-Element Detection and Location (FEDAL) module at 1100°F, sodium flow at 2 ft/sec in the vertical section, and circulating argon gas flow at 1 ft<sup>3</sup>/min.

In both tests, normal operation of the cascade still resulted in entrapment of the fission-gas activity as observed in tests at lower temperatures.

In the first test, there was an initial rise in the activity level to ~27,600 cpm that held steady for 4 min. When the sodium flow was reduced to zero, the activity increased slowly and linearly to ~36,000 cpm. Subsequent restart of the pump produced a peak at ~168,000 cpm, which eventually leveled off at 66,000 cpm.

No initial peak was observed in the second test. Instead, a slight rise in activity to 1800 cpm occurred after 3 min. When the pump was turned off, the activity increased linearly to 60,000 cpm after 7 min. Only a slight peak was observed after pump restart.

Three comparison tests at 500, 800, and 1100°F, respectively, were also performed with the module operating at the flood level, i.e., the cascade totally submerged. The results were identical: only one peak occurred 48 sec after injection of the krypton-85 gas; there was quantitative recovery of the gas, and no second peak after stop and restart of sodium flow.

These results indicate that gas-bubble separation occurs primarily at the surface of the sodium pool and that a gas-trapping action occurs with the cascade operating in a normal manner. There was no separation of the krypton gas in the surge tank, which confirms that gas solubility or carryover is not present.

c. EBR-II In-Core Instrument Test Facility (E. Hutter)

(i) Design, Development, and Fabrication of the Facility  
(O. S. Seim, R. H. Olp, and T. Sullivan)

Not previously reported.

(a) Mockup Testing. A mockup-testing program has been initiated to provide full-scale design information for the final design of the facility. The mockup area is located in Building D-331 (EBWR reactor building), which is equipped with the necessary overhead crane space to handle the 35-ft-long INCOT assemblies. A full-scale mockup of portions of the EBR-II small rotating plug has been installed in the access opening of the lower-level walkway area of the building. This mockup will include the following full-scale dimensional projections of the major pieces of equipment and overhead structures now on the EBR-II rotating plug: reactor cover-lifting structure, festoon-cable takeup reel, control-rod drive assemblies, and the associated center support column including the lifting platform.

The first items scheduled for testing in the mockup are full-scale models of the straight handling container, the offset handling container, and the assembly of the terminal box and support station. As part of the INCOT quality-assurance program, the testing program will include operating tests of the mockup of the final INCOT equipment.

## 2. Fuel Handling, Vessels, and Internals

### a. Core Component Test Loop (CCTL) (R. A. Jaross)

Last Reported: ANL-7661, p. 25 (Jan 1970).

#### (i) Loop Modifications to Accommodate Second FFTF Subassembly

(a) Pump-bypass Piping. The insulation, electrical heater, and leak-detector circuit have been removed preparatory to replacement of the 2-in. Powell valve used to throttle bypass flow through the hydraulic bearing of the pump. The valve was installed in the CCTL before completion of qualification tests of this design at typical operating conditions; it was assumed that because of the low pressure at the pump-bearing bypass, the tests would be successful.

In the qualification tests, a 2-in. Powell valve was filled with sodium from a loop of known concentration of sodium oxide, and operated at 10 psig and 1000°F. The valve incurred a bellows failure after 45 cycles. In view of the relatively few cycles to failure, the Powell valve was adjudged unacceptable for service in the CCTL.

Criteria for acceptance of the pump-bearing-bypass valve was established as follows:

| <u>No. of<br/>Cycles</u> | <u>Pressure<br/>(psig)</u> | <u>Temperature<br/>(°F)</u> |
|--------------------------|----------------------------|-----------------------------|
| 300                      | 10                         | 1000                        |
| 500                      | 10                         | 1160                        |
| 200                      | 50                         | 1160                        |

The Powell valve is being replaced by a Robertshaw-Fulton valve. The latter has successfully completed the above acceptance test.

(b) Plugging Loop. All mechanical, quality assurance, and electrical work associated with this modification is completed. A 500°F ambient-system-qualification test to provide for sodium preheating of this facility is completed.

(c) Vacuum-Distillation-Sodium Sampler and Materials-Surveillance Facility. Drawings for all components external to the CCTL test vessel have been completed, reviewed, and procurement started. Completion of this facility is not required for loop operation.

(d) Cold Trap. After removal of the insulation, the cold trap was visually inspected for electrical and mechanical integrity of the heater and thermocouple. Trace resistance heaters for the NaK-jacket economizer were found suspect and were replaced. Also, seven thermocouples in the NaK heat-rejection system evidenced faulty insulation; they were replaced by stainless steel-jacketed thermocouples.

### C. Sodium Technology

#### 1. Purification of Sodium

##### a. Identification and Removal of Particulate Matter in Sodium (J. E. Draley)

Last Reported: ANL-7640, p. 34 (Nov 1969).

To help establish criteria for the control of particulate matter in LMFBR coolant sodium, it is planned to determine the concentration and composition of the particles in EBR-II primary and secondary coolants. Before collecting particles from the EBR-II, however, suitable methods and procedures must be developed. For this purpose, filtration experiments are being performed with the Mechanical Properties and Corrosion Loop, and the first of these has been completed.

The loop is constructed of Type 347 stainless steel, has a sodium capacity of ~20 gal, and was operated in the temperature range from 565 to 371°C, with a bypass cold trap at 130°C. The loop had already been running for 3 days, containing a variety of new, stainless steel specimens for other tests, when the particle filter was installed on the bypass, ahead of the cold trap. The filter consisted of a 0.25-in. layer of cobalt powder (nominally 3-4  $\mu\text{m}$ ) on a stainless steel filter disk (5- $\mu\text{m}$  porosity). The temperature of the sodium passing through the filter on its way to the cold trap was about 350°C.

The pressure drop through the filter was well within the pumping capability of a small electromagnetic pump that circulated the sodium through the cold-trap sidestream. During the 27 hr of the filtration experiment, a reduction in flowrate through the filter of about 54% occurred, with constant pump power. A total sodium flow of 243 gal through the filter was calculated by integrating the curve of flow rate versus time.

The particles collected by the filter have not been identified yet. Treatment of the cobalt powder with water revealed the presence of a

second phase, apparently magnetic, which was darker and settled more slowly from the aqueous suspension than the bulk of the cobalt. Spectroscopic and X-ray analysis of this material is planned.

## 2. On-line Monitors

- a. Evaluation and Improvement of the Carbon-activity Meter  
(J. T. Holmes, C. Luner, and N. Chellew)

Last Reported: ANL-7640, pp. 35-36 (Nov 1969).

Included in our program on development of on-line monitors for sodium impurities is the evaluation and improvement of a carbon meter developed by the United Nuclear Corporation (UNC).<sup>\*</sup> This meter measures carbon diffusion (or carbon flux) through an iron membrane exposed to sodium at 1200 to 1400°F. The carbon reaching the reverse side of the membrane is reacted with a flowing, moist, hydrogen-argon mixture to form CO. The CO is catalytically converted to CH<sub>4</sub>, and the CH<sub>4</sub> concentration in the gas stream is continually measured by a flame-ionization detector. The on-line carbon meter includes a preheat section to bring the sodium to the desired temperature before it flows past the diffusion membrane.

The ultimate goal of this work is a reliable on-line carbon meter that will indicate whether or not detrimental carburization or decarburization is taking place in the LMFBR. The more immediate objectives are (1) an understanding of the basic relationship of the carbon-meter response to various carbon species, (2) a proof test of the current UNC carbon meter in flowing sodium, and (3) improvement of the current diffusion-type carbon meter and installation of the improved model in the EBR-II primary sodium system.

To realize the first objective, the response of the UNC carbon meter to the addition of various materials which behave as sources or sinks for carbon is being investigated. In these experiments, the diffusion probe is immersed in sodium contained in a copper vessel and stirred with a copper agitator. An all-copper system (except for the probe) is used because copper is inert to carbon and thus does not alter the carbon concentration in the sodium.

Experiments reported previously in ANL-7640 showed that addition of a ferritic steel or small amounts (~1 ppm C) of sodium carbide substantially increased the carbon flux through the probe, and that the insertion of a Type 304 stainless steel rod markedly decreased the carbon flux. From this behavior, it can be inferred that the high-temperature UNC side loop, which is fabricated from stainless steel, may act as a getter

---

<sup>\*</sup>Mckee, J. M., Caplinger, W. H., and Kolodney, M., Nucl. Appl. 5, 236 (1968).

for carbon and lower the carbon concentration at the carbon-sensing probe. Consequently, an inert liner for the side loop was sought. The response of the probe on inserting various materials into stirred sodium was tested. Molybdenum and a molybdenum-30 wt % tungsten alloy caused no noticeable change in the carbon flux, whereas a nickel rod increased the flux. Accordingly, molybdenum was selected for further testing as the liner material for the high-temperature sections in the meter. Copper, although inert to carbon, is not considered a potential liner material because of its high solubility in sodium.

As part of the experimental program to proof-test the UNC carbon meter in flowing sodium, a small, pumped-sodium apparatus (the Test and Evaluation Apparatus, TEA) has been built and the UNC carbon meter installed. TEA was recently started up, and experiments with the carbon meter have begun. Tests of the response of the UNC carbon meter, with its Type 304 stainless steel side loop, to the addition of small quantities of  $\text{Na}_2\text{C}_2$  and NaCN are planned. The modified meter having a molybdenum liner in the high-temperature sections will be installed in parallel with the UNC meter at a later date for direct comparison.

### 3. Sampling

#### a. Sampling of Radioactive Sodium (W. E. Miller and P. Vilinskas)

Last Reported: ANL-7640, p. 36 (Nov 1969).

The presence of radioactive  $^{22}\text{Na}$  and  $^{24}\text{Na}$  in reactor sodium complicates its sampling and analysis. In the analyses for oxygen and trace metals, the radioactive sodium can be separated by evaporation in an on-line distillation sampler. The purpose of this work is to develop improved on-line distillation samplers and to extend this method to in situ analysis of the residue and to analysis of fission products more volatile than sodium.

The use of a liquid-sodium jet eductor to create the vacuum required for distillation is being investigated. Such a device may simplify the design and operation of distillation samplers, since the jet provides means of disposing of the radioactive sodium distillate by returning it to the reactor system. In addition, this method of drawing a vacuum can also be useful in analyzing for fission products more volatile than sodium, such as cesium and rubidium. Available data indicate a high relative volatility for these metals in dilute sodium solution; e.g., at  $440^\circ\text{C}$ , cesium is about 150 times more volatile than sodium. Thus, continuous on-line distillation to separate cesium isotopes from the  $^{24}\text{Na}$  activity may be possible.

To accomplish this separation, sodium could be drawn through an orifice into a flash chamber. If the flash chamber is operated at 1 Torr



pressure and the entering sodium is at 550°C, only ~2% of the sodium flow would be vaporized in a constant-enthalpy process while the bulk of the cesium is being vaporized. The vapor could then be fed to a rectification device operated under almost total reflux. The cesium-rich vapor from the top of the rectification device would be continuously analyzed by a gamma counter and returned to the system through a jet eductor. The liquid from this separations process would be returned to the system through the same jet eductor. Calculations show that the enrichment factor for cesium, expressed as

$$\left( \frac{\text{Cs activity}}{^{24}\text{Na activity}} \right)_{\text{exit gas}} / \left( \frac{\text{Cs activity}}{^{24}\text{Na activity}} \right)_{\text{inlet liquid}},$$

is approximately  $10^5$  for partial evaporation followed by about two theoretical stages of rectification. The dynamic flow characteristics of such a system are being studied in a mockup using water instead of sodium.

#### 4. Fission Product Behavior and Control

##### a. Data-analysis Methods for Determining Fuel Failures (W. E. Miller)

Last Reported: ANL-7640, pp. 36-37 (Nov 1969).

An important objective for fuel-failure detection systems is the capability of differentiating between innocuous leaks and serious ruptures than may lead to blockage of coolant channels and propagation of fuel failure. Examination of a variety of data on irradiated fuels indicates that such a distinction might be based on the relative concentrations of various isotopes of cesium and rubidium in the sodium coolant.

Cesium and rubidium (as well as iodine, bromine, and tellurium) migrate through  $\text{UO}_2\text{-PuO}_2$  fuel and collect at the fuel-cladding gap or interface. Cesium and rubidium isotopes can enter the sodium through a break in the cladding by three mechanisms: (1) dissolution in sodium contacting the bare fuel, (2) volatilization into the sodium, and (3) decay of xenon and krypton precursors that have reached the sodium or the cover gas. The ratio of the various isotopes in the sodium would be expected to vary with (1) the mechanism(s) of escape and (2) the residence time of the precursors and of the cesium and rubidium isotopes inside the fuel cladding. The latter is controlled by the size of the cladding break; thus, a large, serious break might be indicated by a sudden increase in certain of the cesium and rubidium isotopes in the sodium coolant.

Further evaluation of this concept, especially with regard to the volatility of cesium and rubidium from oxide fuels and the likely extent of release of the various isotopes of these elements from various types of fuel failures, is under way.



## D. EBR-II--Research and Development

### 1. Equipment--Fuel Related (E. Hutter)

#### a. Higher-worth Control Rod (O. S. Seim and T. Sullivan)

Last Reported: ANL-7640, p. 39 (Nov 1969).

All parts needed for two prototypes of the higher-worth control rods have been fabricated. Preirradiation measurements of the  $B_4C$  pellets that will be used in each upper preassembly will be made prior to assembly.

#### b. Higher-worth Safety Rod (O. S. Seim and T. Sullivan)

Not previously reported.

Fabrication drawings of a higher-worth safety rod are complete. The design incorporates a 10-in.-long section containing natural  $B_4C$ . Additional studies are being made to compare the worth of the natural  $B_4C$  rods with that of enriched  $B_4C$  rods.

### 2. New Subassemblies and Experimental Support (E. Hutter)

#### a. Improved Reflector Subassembly (O. Seim, W. Ware, and D. Walker)

Previously Reported: ANL-7548, p. 47 (Jan 1969).

Design of the Type BNS (bare nickel and stainless steel) reflector subassembly has been completed, and 190 complete subassemblies are being fabricated. The BNS subassembly is a standard-sized EBR-II hexagonal subassembly that contains solid hexagonal slugs of nickel reflector and/or stainless steel shield material. It is designed for use in both the inner and outer blanket regions of the reactor.

For use as a reflector (primarily in the inner blanket region), the subassembly comprises an upper and lower axial shield and a reflector section. The lower shield is a single length of Type 304 stainless steel, and the upper axial shield is two lengths of Type 304 stainless steel. The reflector section, three lengths of nickel, is centered on the vertical core centerline. The uppermost shield piece is cut to length to provide a minimum gap of 1/16 in. between a crushable tube and the top end fixture.

For use as a shield subassembly (primarily in the outer blanket), the nickel reflector pieces are replaced by pieces of stainless steel. Each shield or reflector piece is hexagonal and measures 2.062 in. across the flats.

The basic subassembly, shown in Fig. I.D.1, has an overall length of 27 in. and an outside diameter of 2.290 in. across the hexagonal

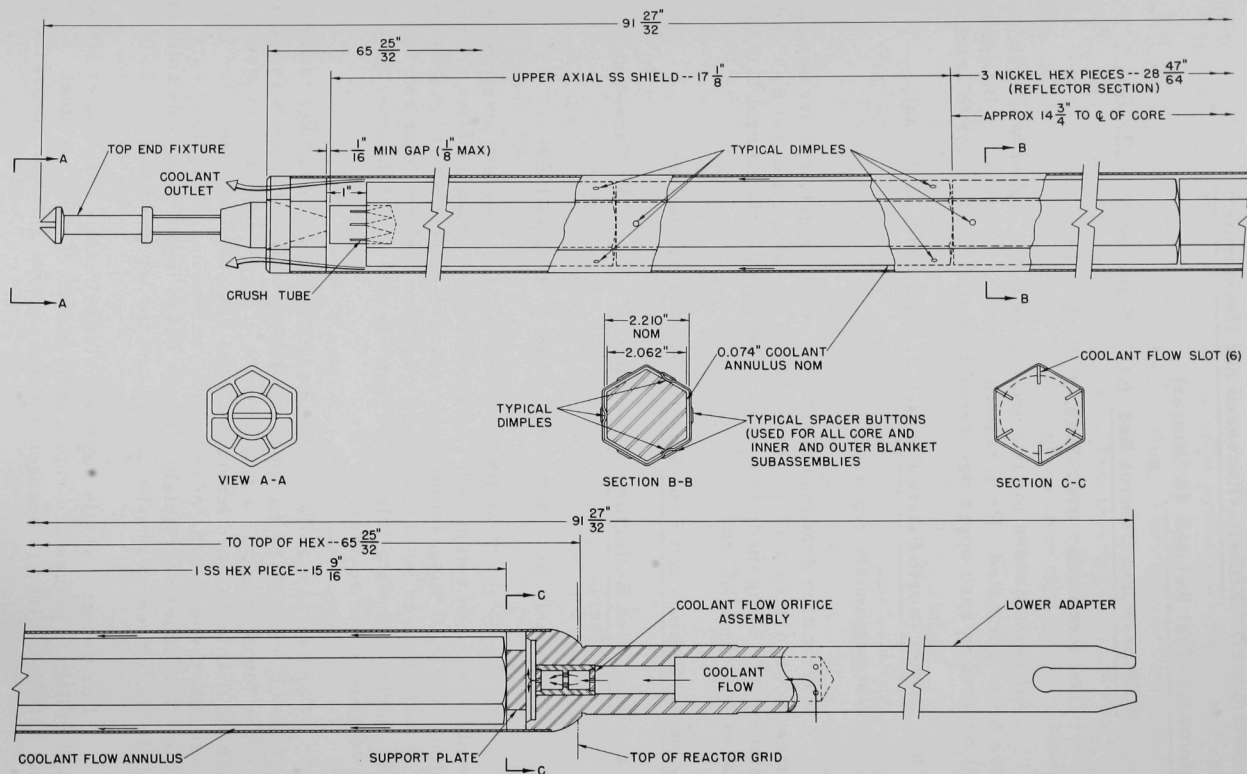


Fig. I.D.1. EBR-II Model BNS Reflector Subassembly

flats. These dimensions are identical with those of all other EBR-II sub-assemblies except control- and safety-rod subassemblies. The lower adapter of the subassembly is the same as that used in a standard EBR-II inner- or outer-blanket subassembly containing an assembly for orificing coolant flow. A hexagonal tube  $64\frac{17}{32}$  in. long and 2.290 in. across the flats is welded to the lower adapter. This tube contains the shield and/or reflector pieces. A standard EBR-II top end fixture is welded into the top of the hexagonal tube so that the subassembly can be handled by the normal EBR-II fuel-handling equipment.

A slotted support plate is placed above the lower adapter and on the inside of the hexagonal tube. This plate supports the weight of the six metal shield and/or reflector pieces. Coolant passes through the slots and enters a 0.074-in.-wide annulus between the shield and reflector pieces and the inside wall of the hexagonal tube.

The shield and/or reflector pieces are kept centered within the hexagonal tube by dimples formed in the alternate flats of the tube at the top and bottom of each piece. Each tube flat contains six dimples spaced at various intervals along its length to give a total of 36 dimples. Each dimple is  $3/8$  in. in diameter and 0.048 in. deep. Thus, the clearance between the bottom of the dimple and the shield and reflector pieces is 0.052 in. This clearance will accommodate any anticipated differential swelling. A short length of thin-walled, small-diameter stainless steel tubing between the upper shield piece and the top end fixture holds the subassembly components against the support plate, and will crush to accommodate vertical swelling.

A technique has been developed to form the tube dimples without distorting the tube beyond the dimensional tolerance. This technique, which uses a metal female die and a rubber male die in a hydraulic press, eliminates the problems of maintaining precise die alignment and the associated dimensional deviations that misalignment would cause. A simple laboratory setup of the hydraulic press and dies has been made to demonstrate workability. A measured length of hexagonal tubing was dimpled with the laboratory setup. After being dimpled, the tubing was measured again to see if the dimensions had changed. The test indicated that the dimples could be formed accurately to within a  $\pm 0.003$ -in. tolerance without distorting the tube significantly. This forming method will be used in the fabrication of the 190 subassemblies.

### 3. Instrumented Subassemblies (E. Hutter and A. Smaardyk)

#### a. Test Three-PNL-17

Last Reported: ANL-7655, pp. 58-59 (Dec 1969).

(i) Assembly. The assigned experimental number for this subassembly is XX02.

Fuel elements for XX02 were received from the Pacific Northwest Laboratory (PNL), and were accepted after inspection and radiography by ANL. After inspection, the instrument leads were cut and dressed to the required length for assembling, and the required checks of electrical instrumentation were made. The resistance of the insulation of the thermocouples was of the order of  $10^9$  ohms at 50 V, except for the thermocouple in element 19, the insulation of which had a measured resistance of  $1.4 \times 10^6$  ohms at 25 V. Because of the central location of element 19 with respect to other adjacent thermocouples, PNL instructed ANL to proceed using element 19. Assembly began on February 9.

A completed flowmeter that had been tested in the sodium flowmeter-test loop also was received. It was covered with a black oxide film resulting from exposure to sodium in the loop. Procedures were prepared for making the plug weld to the hexagonal subassembly tube, and sample weldments showed that satisfactory welds could be made without removing the oxide film.

After it had been assembled, the subassembly was subjected to a tensile test, which indicated elastic conditions under a test load of 2000 lb. The extension tube is being assembled.

Plans are being made to modify the EBR-II instrumented-subassembly shipping container for shipping XX02 from Illinois to the EBR-II site. A closely fitted wooden structure will be used around the fuel-element section, and the outer container will be reinforced with heavy plate at the fuel-element location.

#### (ii) Bulkhead Brazing (D. Walker)

The procedure developed to braze the 20 stainless steel sensor leads to the bulkhead for instrumented subassembly XX01 (test 2) has been changed for subassembly XX02. This change was made to prevent the embrittlement of the sensor leads that occurred at the top of the braze joint, where the braze alloy powder had been preplaced.

Figure I.D.2 shows the design of the bulkhead for XX02. The 0.187/0.189-in.-dia holes are cavities in the bulkhead. Braze-alloy powder is preplaced in these cavities, and stainless steel sleeves, which are placed over the sensor leads from the top, are pushed down into the cavity in the bulkhead until they contact the powder (see Fig. I.D.3). After brazing, fillets of braze alloy will be at locations A and B in Fig. I.D.3. In these areas, the reaction of the sensor lead with the braze alloy is minimal, and the lead remains ductile. The zone of greatest embrittlement occurs where the braze-alloy powder had been placed preparatory to brazing. The added sleeve completely isolates the area.

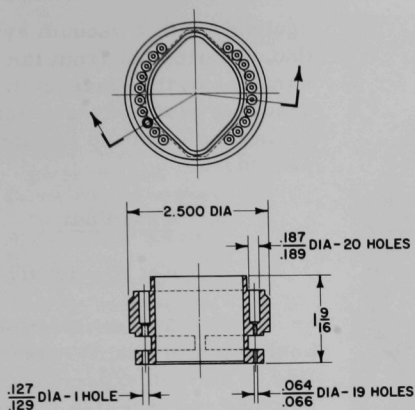


Fig. I.D.2

Drywell Bulkhead for Instrumented Subassembly XX02

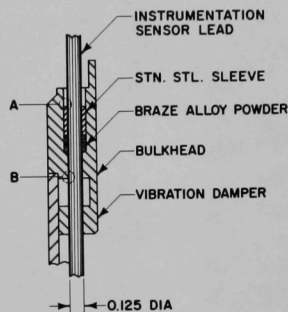


Fig. I.D.3

Longitudinal Section of Drywell Bulkhead for Instrumented Subassembly XX02, Showing Pre-placement of Braze-alloy Powder and Insertion of Stainless Steel Sleeve

Figure I.D.4 shows a longitudinal cross section through an etched full-sized test braze sample. Excellent wetting and flow of the braze alloy has occurred. The sensor lead has been brazed to the bulkhead at the B location, and to the sleeve and bulkhead at the A location. The preplaced powder has consolidated as a result of melting, and an isolated void has developed.

The same sodium-compatible, high-nickel braze alloy used on XX01 will be used on the XX02 bulkhead. The composition and melting range of the alloy are:

Chemical Analysis, wt %

Si--10.00  
Cr--20.00  
Fe--3.00  
Ni--Balance

Melting Range, °F

| <u>Solidus</u> | <u>Liquidus</u> | <u>Brazing Temperature</u> |
|----------------|-----------------|----------------------------|
| 1975           | 2075            | 2150                       |

The brazing is done in high-purity hydrogen supplied from a palladium-silver alloy diffusion purifier. The brazing furnace is

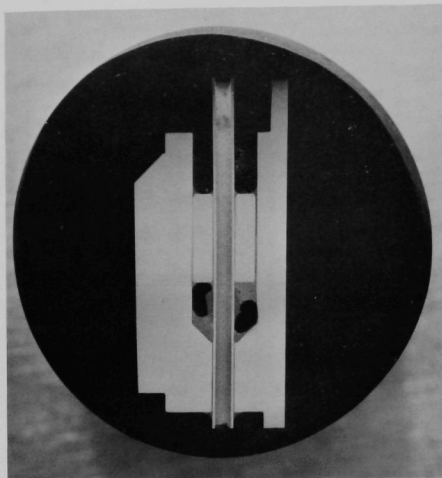


Fig. I.D.4. Etched Longitudinal Section through Brazed Sensor Lead in Test Bulkhead of Instrumented Subassembly XX02 (PNL-17). Gray areas at interfaces are the braze alloy. Mag. 2.5X.

equipped with a vacuum system that removes air from the mating surfaces of the braze joint, thereby ensuring good hydrogen activation during the clean-up portion of the procedure.

#### b. Test Four

Not previously reported.

The description, safety analysis, and quality-assurance outline of a creep experiment that is to be made in the test-4 instrumented subassembly has been received from Battelle Northwest Laboratory.

One creep specimen, loaded by pneumatic bellows, and four pressurized tubes will be included in the subassembly for study of biaxial stresses. ANL will install the capsule containing the

specimen and its associated instrumentation in the subassembly. The test-4 subassembly will differ from the previous instrumented subassemblies mainly in the use of two heavy leads. A 3/16-in. heater lead will supply 7 kW of electrical power to the creep-capsule heater, and a 3/16-in. concentric shaft arrangement will drive an extensometer gearbox within the creep capsule. Another requirement calls for operation of the temperature controls and heater during fuel handling to maintain the capsule at the desired temperature.

Table I.D.1 lists the instrument-lead requirements for the subassembly.

Methods for incorporating the inlet-coolant and outlet-coolant thermocouples, as well as for supporting the creep capsule, were developed and incorporated into the design. A drywell has been introduced into the design of the subassembly, separate from the creep capsule, for housing the flux monitors.

The lead cutting that is to be done before the subassembly is removed from the reactor is being developed. This development work consists of studying the optimum placement of the leads on the cutting circle, the cutting of sample leads in air, and the proof test cutting of representative leads in a sodium environment.

TABLE I.D.1. Instrument-lead Requirements for the Test-4 Instrumented Subassembly

| Designation                                      | Diameter of Leads (in.) | Number of Leads Required |
|--|-------------------------|--------------------------|
| Ceramic-insulated sheathed cable for heater coil | 3/16                    | 1                        |
| Concentric drive shaft for extensometer          | 3/16                    | 1                        |
| Extensometer detector                            | 1/16                    | 1                        |
| Biaxial-specimen tubes                           | 1/16                    | 4                        |
| Capsule thermocouples                            | 1/16                    | 6                        |
| Loading-bellows tube                             | 1/8                     | 1                        |
| Capsule-gas thermocouple                         | 1/16                    | 2                        |
| Inlet-coolant thermocouple                       | 1/16                    | 1                        |
| Outlet-coolant thermocouple                      | 1/16                    | 1                        |
| Flux-monitor tube                                | 3/16                    | 1                        |
|  |                         | Total 19                 |

The equipment for performing the lead-cutting tests in air comprises a structure to simulate the 30-ft-long extension tube, a motor to drive the shaft of the cutting tool, and a torque transducer. The equipment for performing the lead-cutting tests in sodium includes two pots. The tests will be performed in one of the pots, and the other pot will serve as a sodium reservoir. A motor-mount pad is on the cover of the first pot, and the drive shaft of the cutting tool extends through the cover. A test block containing leads and the cutting tool can be inserted through the cover.

#### 4. Coolant Chemistry (D. W. Cissel)

- a. Sodium Coolant Quality Monitoring and Control (W. H. Olson, E. R. Ebersole, and D. C. Cutforth)

Last Reported: ANL-7661, pp. 37-40 (Jan 1970).

(i) In-line Vacuum Distillation of Sodium. Testing of the in-line vacuum-distillation sodium sampler continued in the EBR-II secondary sodium system. The sampler was designed to provide residue from 125 g of sodium for determinations of trace metals. It appears that the sampler also can be used for oxygen determinations if all sodium in the residue can be assumed to be  $\text{Na}_2\text{O}$ .

Table I.D.2 lists the results for three samples of secondary sodium, each ~125 g and obtained with a sample flow of ~0.8 gpm, distilled in line and analyzed for oxygen. The residue was dissolved, and total sodium was determined by flame-emission spectrophotometry. Oxygen concentration then was calculated by assuming that all sodium was present as  $\text{Na}_2\text{O}$ .



TABLE I.D.2. Oxygen in Secondary Sodium by  
Analysis of Vacuum-distillation Residues

| Sample<br>Date | Sample<br>Container | Flush<br>Time<br>(min) | Sample<br>Temp<br>(°F) | Oxygen<br>(ppm) |
|----------------|---------------------|------------------------|------------------------|-----------------|
| 12/18/69       | Ti                  | 18                     | 533                    | 1.4             |
| 2/11/70        | Ti                  | 32                     | 560                    | 1.7             |
| 2/12/70        | 304 SS              | 55                     | 550                    | 1.6             |

Note: On 1/15/70, oxygen was 1.8 ppm as determined by the mercury amalgamation method.

(ii) Nitrogen Contamination in EBR-II Primary Cover Gas. The nitrogen content in the EBR-II primary cover gas has been monitored closely since April 1968. Three general trends were observed after several months of monitoring. First, step increases in the nitrogen concentration often occurred during restricted fuel handling. Step increases of 1000 ppm were common, and some step increases of 2500 ppm were observed. The second trend was a steady increase in nitrogen content during unrestricted fuel handling. Increases of 1000-2000 ppm were frequent. The third trend was a gradual decrease in nitrogen content when the reactor was operating.

During 1968 and the first nine months of 1969, the nitrogen content in the primary cover gas ranged from a low of less than 1000 ppm, at the end of a purge of the primary-tank cover gas, to a high of about 14,500 ppm. The overall weighted average concentration during this time was about 5500 ppm.

The operating procedures for restricted fuel handling were refined near the end of 1969. Since then, step increases in nitrogen content during restricted fuel handling have not been observed. However, the nitrogen content still has increased during unrestricted fuel handling and decreased during reactor operation. The pressure of the primary cover gas was raised during an extended sequence of unrestricted fuel handling, but the results were inconclusive. Further work is planned to ascertain the effect of increased cover-gas pressure.

Since October 1969, the nitrogen content has ranged from a low of about 2000 ppm to a high of about 5500 ppm. The weighted average concentration is about 3300 ppm.

## 5. Experimental Irradiation and Testing\* (R. Neidner)

### a. Experimental Irradiations

Last Reported: ANL-7661, p. 40 (Jan 1970).

Table I.D.3 shows the status of the experimental subassemblies in EBR-II as of February 15, 1970.

TABLE I.D.3. Status of EBR-II Experimental Irradiations as of February 15, 1970 (Run 40B in Progress)

| Subassembly<br>No. and<br>(Position) | Date<br>Charged | Capsule Content and<br>(Number of Capsules)    | Experi-<br>menter | Accumulated<br>Exposure<br>(MWd) | Estimated<br>Goal<br>Exposure<br>(MWd) | Burnup <sup>a</sup>            |
|--------------------------------------|-----------------|--|-------------------|----------------------------------|--|--------------------------------|
| XG03<br>(7D1)                        | 7/16/65         | UO <sub>2</sub> -20 wt % PuO <sub>2</sub> ( 2) | GE                | 26,948                           | 37,000                                 | 6.9                            |
| XG04<br>(7B1)                        | 7/16/65         | UO <sub>2</sub> -20 wt % PuO <sub>2</sub> ( 2) | GE                | 28,144                           | 45,000                                 | 7.2                            |
| XO12A<br>(4B2)                       | 12/12/69        | UO <sub>2</sub> -20 wt % PuO <sub>2</sub> (19) | NUMEC             | 2,038                            | 4,200                                  | 1.1 + 10.2 <sup>b</sup> = 11.3 |
| XO18B<br>(4E2)                       | 10/2/69         | Structural ( 3)                                | GE                | 2,638                            | 10,000                                 | 1.0 + 5.8 <sup>b</sup> = 6.8   |
|                                      |                 | Structural ( 2)                                | ANL               |                                  |  | 1.0 + 5.8 <sup>b</sup> = 6.8   |
|                                      |                 | Structural ( 1)                                | ANL               |                                  |  | 1.0                            |
|                                      |                 | Structural ( 1)                                | PNL               |                                  |  | 1.0                            |
| XO21B<br>(2D1)                       | 2/23/69         | Structural ( 6)                                | PNL               | 18,278                           | 23,200                                 | 3.9 + 4.1 <sup>b</sup> = 8.0   |
|                                      |                 | Structural ( 1)                                | PNL               |                                  |  | 3.9                            |
| XO27<br>(4B3)                        | 11/21/67        | UO <sub>2</sub> -25 wt % PuO <sub>2</sub> (18) | GE                | 15,430                           | 17,600                                 | 8.5                            |
|                                      |                 | Structural ( 1)                                | PNL               |                                  |  | 6.1                            |
| XO34A<br>(2F1)                       | 9/30/69         | Structural ( 4)                                | ORNL              | 2,638                            | 7,500                                  | 1.1 + 4.8 <sup>b</sup> = 5.9   |
|                                      |                 | Structural ( 3)                                | ORNL              |                                  |  | 1.1                            |
| XO35<br>(7B3)                        | 4/13/68         | Structural ( 7)                                | ORNL              | 15,222                           | 44,800                                 | 3.5                            |
| XO36<br>(7E1)                        | 7/25/68         | UO <sub>2</sub> -25 wt % PuO <sub>2</sub> (19) | GE                | 12,828                           | 43,300                                 | 3.4                            |
| XO38<br>(7C5)                        | 5/7/68          | Structural ( 7)                                | INC               | 14,804                           | 17,700                                 | 3.2                            |
| XO40A<br>(5B2)                       | 9/30/69         | UO <sub>2</sub> -20 wt % PuO <sub>2</sub> (18) | ANL               | 2,638                            | 4,800                                  | 1.3 + 3.5 <sup>b</sup> = 4.8   |
|                                      |                 | UO <sub>2</sub> -25 wt % PuO <sub>2</sub> (16) | GE                |                                  |  | 1.3 + 3.4 <sup>b</sup> = 4.7   |
| XO41<br>(7A3)                        | 7/24/68         | Structural ( 7)                                | PNL               | 13,264                           | 16,700                                 | 2.9                            |
| XO43<br>(4D2)                        | 2/20/69         | UO <sub>2</sub> -25 wt % PuO <sub>2</sub> (37) | GE                | 8,544                            | 11,000                                 | 4.7                            |
| XO50<br>(4C2)                        | 2/23/69         | UO <sub>2</sub> -20 wt % PuO <sub>2</sub> ( 4) | GE                | 8,544                            | 11,900                                 | 4.5 + 7.4 <sup>b</sup> = 11.9  |
|                                      |                 | UO <sub>2</sub> -28 wt % PuO <sub>2</sub> ( 4) | GE                |                                  |  | 4.5                            |
|                                      |                 | UO <sub>2</sub> -20 wt % PuO <sub>2</sub> ( 5) | ORNL              |                                  |  | 4.5                            |
|                                      |                 | (U <sub>0.28</sub> -Pu <sub>0.18</sub> )C ( 2) | W                 |                                  |  | 4.5                            |
|                                      |                 | Structural ( 4)                                | GE                |                                  |  | 3.3 + 5.3 <sup>b</sup> = 8.6   |
| XO51<br>(3A2)                        | 12/16/68        | UO <sub>2</sub> -25 wt % PuO <sub>2</sub> (37) | PNL               | 9,089                            | 16,400                                 | 1.8                            |
| XO54<br>(4E1)                        | 3/31/69         | UO <sub>2</sub> -25 wt % PuO <sub>2</sub> (37) | PNL               | 7,944                            | 10,000                                 | 4.2                            |
| XO55 <sup>c</sup><br>(7A4)           | 2/23/69         | (U <sub>0.85</sub> -Pu <sub>0.15</sub> )C (19) | UNC               | 9,314                            | 20,000                                 | 2.9                            |
| XO56<br>(5C2)                        | 4/2/69          | UO <sub>2</sub> -25 wt % PuO <sub>2</sub> (37) | GE                | 7,944                            | 10,600                                 | 3.9                            |
| XO57<br>(2B1)                        | 2/23/69         | Structural ( 7)                                | PNL               | 9,314                            | 15,000                                 | 3.9                            |
| XO58<br>(6F1)                        | 4/24/69         | UO <sub>2</sub> -25 wt % PuO <sub>2</sub> (37) | GE                | 7,368                            | 16,000                                 | 2.7                            |
| XO59<br>(4A1)                        | 4/23/69         | UO <sub>2</sub> -25 wt % PuO <sub>2</sub> (37) | PNL               | 7,368                            | 17,500                                 | 2.5                            |
| XO61<br>(7A5)                        | 4/23/69         | Structural ( 7)                                | INC               | 8,138                            | 18,000                                 | 1.8                            |
| XO62<br>(6F3)                        | 5/23/69         | UO <sub>2</sub> -25 wt % PuO <sub>2</sub> (37) | GE                | 5,465                            | 13,400                                 | 2.4                            |

TABLE I.D.3 (Contd.)

| Subassembly No. and (Position) | Date Charged | Capsule Content and (Number of Capsules)       | Experimenter | Accumulated Exposure (MWd) | Estimated Goal Exposure (MWd) | Burnup <sup>a</sup>          |
|--------------------------------|--------------|--|--------------|----------------------------|-------------------------------|------------------------------|
| XO63 (7F5)                     | 6/29/69      | Magnetic Materials ( 7)                        | ANL          | 5,804                      | 5,400                         | 1.2                          |
| XO64 (4F2)                     | 5/28/69      | UO <sub>2</sub> -25 wt % PuO <sub>2</sub> (19) | GE           | 6,236                      | 10,700                        | 3.5                          |
| XO65B (7E5)                    | 1/30/70      | Structural (22)<br>Structural ( 5)             | ANL          | 667                        | 1,350                         | 0.1 + 0.4 <sup>b</sup> = 0.5 |
| XO68 (4A3)                     | 1/30/70      | Mark IA (61)                                   | ANL          | 667                        | 6,500                         | 0.2                          |
| XO69 (4F1)                     | 10/1/69      | UO <sub>2</sub> -25 wt % PuO <sub>2</sub> (37) | PNL          | 2,638                      | 20,700                        | 0.9                          |
| XO70 (3E1)                     | 1/10/70      | UO <sub>2</sub> -20 wt % PuO <sub>2</sub> ( 8) | NUMEC        | 1,267                      | 6,000                         | 0.7 + 6.5 <sup>b</sup> = 7.2 |
|                                |              | UO <sub>2</sub> -20 wt % PuO <sub>2</sub> ( 7) | GE           |                            |                               | 0.7 + 5.1 <sup>b</sup> = 5.8 |
|                                |              | (U <sub>0.8</sub> -Pu <sub>0.2</sub> )C ( 1)   | LASL         |                            |                               | 0.7 + 1.4 <sup>b</sup> = 2.1 |
|                                |              | (U <sub>0.8</sub> -Pu <sub>0.2</sub> )C ( 1)   | LASL         |                            |                               | 0.7                          |
|                                |              | (U <sub>0.8</sub> -Pu <sub>0.2</sub> )C ( 1)   | W            |                            |                               | 0.7                          |
|                                |              | (U <sub>0.8</sub> -Pu <sub>0.2</sub> )N ( 1)   | BMI          |                            |                               | 0.7                          |
| XO71 (4C3)                     | 1/30/70      | Mark II (28)                                   | ANL          | 667                        | 3,800                         | 0.4                          |
|                                |              | Mark II ( 9)                                   | ANL          |                            |                               |                              |
| XO72 (6B2)                     | 12/12/69     | UO <sub>2</sub> -20 wt % PuO <sub>2</sub> (18) | ANL          | 2,038                      | 9,200                         | 0.8                          |
|                                |              | Structural ( 1)                                | ANL          |                            |                               | 0.5                          |
| XO73 (6C3)                     | 12/12/69     | UO <sub>2</sub> -25 wt % PuO <sub>2</sub> (37) | PNL          | 2,038                      | 29,600                        | 0.5                          |
| XO74 (5A2)                     | 1/10/70      | UO <sub>2</sub> -25 wt % PuO <sub>2</sub> (37) | PNL          | 1,267                      | 14,500                        | 0.6                          |
| XO75 (5E4)                     | 1/30/70      | (U <sub>0.8</sub> -Pu <sub>0.2</sub> )C (18)   | UNC          | 667                        | 5,100                         | 0.3                          |
| XXO1 (5F3)                     | 11/19/69     | UO <sub>2</sub> (16)                           | ANL          | 2,038                      | 2,700                         | 0.5                          |
|                                |              | Structural ( 2)                                | ANL          |                            |                               | 0.7                          |

<sup>a</sup>Estimated accumulated center burnup on peak rod, based on unperturbed flux and without depletion corrections (fuels, at. %; nonfuels, nvt x 10<sup>-22</sup>).

<sup>b</sup>Previous exposure from another subassembly.

<sup>c</sup>XO55 relocated from 6A4 for Run 40.

Subassembly XO20 was discharged from the reactor at the end of Run 39. The following subassemblies were installed: XO65B (ANL/EBR-II pressurized-tubing experiment, reconstituted); XO68 (61 encapsulated Mark-IA fuel elements); XO71 (37 encapsulated Mark-II fuel elements); and XO75 (UNC carbide capsules reconstituted from Subassembly XO33).

Three subassemblies--XO55, XO72, and XO40A--were moved to different grid locations.

## 6. Materials-Coolant Compatibility (D. W. Cissel)

### a. Evaluation and Surveillance of EBR-II Materials

Last Reported: ANL-7661, pp. 40-44 (Jan 1970).

#### (i) Evaluation of Materials Subassembly XA08 (S. Greenberg)

Electron-microprobe examination showed no evidence of carbon transfer to or from the surface. The distribution of carbon observed

in the sample was consistent with the sensitization observed through the optical microscope. The sample-exposure temperature calculated by the HECTIC code is 423°C, which is in good agreement with the minimum temperature of approximately 425°C that was deduced from the observed metal-lurgical structure.

(ii) Substitution of Other Stainless Steels for Type 304 Stainless Steel in EBR-II (S. Greenberg and W. E. Ruther)

Machining costs would be reduced appreciably if Type 304 stainless steel were replaced with a free-machining and/or lower-cost grade in a variety of relatively complicated components of expendable core hardware in EBR-II. In addition, designers would have more flexibility if these alternative materials were acceptable.

The primary alternative materials being considered are Types 201, 302, and 303 stainless steels (the last would not be used for any fusion-welded component). These materials along with Type 304 LN stainless steel--an experimental material of possible LMFBR interest--are being tested together with Type 304 stainless steel as a basis for comparison in a polythermal flowing-sodium loop. The temperatures in the hot and cold legs of the loop are 1050 and 700°F, cold-trap temperature is 257°F, and maximum flow rate is approximately 2 m/sec. The test has run for about a month.

Type 304 LN stainless steel, made by U.S. Steel, has a relatively high nitrogen content; the test samples contain 0.14% N and 0.016% C. It is designed for increased resistance to intergranular penetration.

(iii) Evaluation of Chromium Plating (W. E. Ruther)

Preparations are being made for corrosion evaluation of thin (~0.0001 in.) chromium plating within EBR-II. The hardware has been machined, and the corrosion specimens have been prepared for exposure in a material-test subassembly in the EBR-II inner blanket.

Thirty ring specimens, each approximately 2 in. in diameter and 2 in. long, will be stacked on the central support column in the subassembly. Each specimen will be weighed to the nearest 0.1 mg on an analytical balance before and after the reactor exposure. If only the external exposed area is considered, each milligram of weight loss will correspond to approximately 0.6  $\mu$ in. of chromium loss.

The intent is to expose five repeating groups of six rings each. Each group will consist of the following rings:

- a. bare Type 304 stainless steel;
- b. "electrolizing" chromium plate, 75-150  $\mu$ in. thick;
- c. "electrolizing" chromium plate, 150-250  $\mu$ in. thick;

- d. ordinary electroplate, 25-75  $\mu$ in. thick;
- e. ordinary electroplate, 75-150  $\mu$ in. thick;
- f. ordinary electroplate, 450-550  $\mu$ in. thick;

On the basis of previous experience with a similar sub-assembly, the temperature at the bottom will be 700°F and the temperature at the top approximately 940°F. Sodium flow will be approximately 1.2 gpm. The exposure will be for approximately 10 months in Row 7 of EBR-II. This length of exposure is necessary for accurate forecasting of loss of plating for the longer-lived applications in EBR-II.

b. Examination of Materials from EBR-II Surveillance Subassemblies  
(R. V. Strain and S. Greenberg)

Last Reported: ANL-7661, p. 44 (Jan 1970).

Table I.D.4 lists the changes in weight and in density of the hardness samples exposed in SURV-2. As was the case with SURV-1, only the beryllium-copper and tantalum samples showed consistently high weight losses. (There are no longer any beryllium-copper components operating in the reactor.) One sample each of aluminum bronze and T-1 tool steel also showed unusually high apparent weight losses, which are believed to be due to experimental error. Components fabricated of aluminum bronze and T-1 tool steel are performing satisfactorily in EBR-II.

TABLE I.D.4. Weight and Density Changes of Hardness Samples from SURV-2

| Material                            | Sample <sup>a</sup><br>No. | Preirradiation<br>Weight (g) | Weight<br>Change <sup>b</sup><br>(mg) | Preirradiation<br>Density (g/cm <sup>3</sup> ) | Density<br>Change <sup>b</sup><br>(g/cm <sup>3</sup> ) |
|-------------------------------------|----------------------------|------------------------------|---------------------------------------|--|--|
| Aluminum Bronze--<br>Ampco Grade 18 | A-1                        | 16.1235                      | -1.1                                  | 7.477  | +0.009   |
|                                     | A-2                        | 16.0560                      | -1.5                                  |  |  |
|                                     | A-3                        | 16.0648                      | -9.7                                  |  |  |
|                                     | A-4                        | 16.0629                      | -1.0                                  |  |  |
|                                     | A-5 (He)                   | 16.0239                      | 0.0                                   |  |  |
| Stellite 6B                         | B-1                        | 18.0991                      | +0.3                                  | 8.376  | +0.014   |
|                                     | B-2                        | 18.0889                      | +0.3                                  |  |  |
|                                     | B-3                        | 18.0865                      | +0.1                                  |  |  |
|                                     | B-4                        | 18.1008                      | +0.6                                  |  |  |
|                                     | B-5 (He)                   | 18.1005                      | +0.7                                  |  |  |
| Inconel X-750                       | C-1                        | 17.7736                      | -1.1                                  | 8.267  | +0.017   |
|                                     | C-2                        | 17.7620                      | -1.0                                  |  |  |
|                                     | C-3                        | 17.7684                      | -1.1                                  |  |  |
|                                     | C-4                        | 17.6870                      | -1.0                                  |  |  |
|                                     | C-5 (He)                   | 17.7699                      | -1.2                                  |  |  |
| Type 420                            | D-1                        | 16.3578                      | -0.2                                  | 7.698  | +0.005   |
| Stainless Steel                     | D-2                        | 16.3498                      | -0.9                                  |  |  |
|                                     | D-3                        | 16.3557                      | -0.5                                  |  |  |
|                                     | D-4                        | 16.4963                      | -0.9                                  |  |  |
|                                     | D-5 (He)                   | 16.5042                      | -0.5                                  |  |  |

TABLE I.D.4 (Contd.)

| Material                                  | Sample <sup>a</sup><br>No. | Preirradiation<br>Weight (g) | Weight<br>Change <sup>b</sup><br>(mg) | Preirradiation<br>Density (g/cm <sup>3</sup> ) | Density<br>Change <sup>b</sup><br>(g/cm <sup>3</sup> ) |
|---|----------------------------|------------------------------|---------------------------------------|--|--|
| T-1 Tool Steel                            | E-1                        | 18.6689                      | +0.2                                  | 8.656  | -0.014   |
|   | E-2                        | 18.6770                      | -0.5                                  |  |  |
|   | E-3                        | 18.6598                      | +0.1                                  |  |  |
|   | E-4                        | 18.6753                      | -9.3                                  |  |  |
|   | E-5 (He)                   | 18.7068                      | +1.1                                  |  |  |
| Type 347<br>Stainless Steel               | F-1                        | 16.9494                      | -1.0                                  | 7.908  | 0.000  |
|   | F-2                        | 16.9453                      | -0.4                                  |  |  |
|   | F-3                        | 16.9346                      | -0.5                                  |  |  |
|   | F-4                        | 16.9265                      | -0.6                                  |  |  |
|   | F-5 (He)                   | 16.9272                      | -0.6                                  |  |  |
| Type 416<br>Stainless Steel               | G-1                        | 16.3470                      | 0.0                                   | 7.638  | +0.003   |
|   | G-2                        | 16.3083                      | +0.2                                  |  |  |
|   | G-3                        | 16.3447                      | -0.3                                  |  |  |
|   | G-4                        | 16.3548                      | -1.1                                  |  |  |
|   | G-5 (He)                   | 16.3550                      | -0.7                                  |  |  |
| Beryllium-Copper--<br>Berylco 25          | H-1                        | 17.9677                      | -137.7                                | 8.348  | +0.001   |
|   | H-2                        | 17.9745                      | -333.9                                |  |  |
|   | H-3                        | 17.9862                      | -491.6                                |  |  |
|   | H-4                        | 17.9594                      | -3.6                                  |  |  |
|   | H-5                        | 17.9843                      | -1.1                                  |  |  |
| Type 304<br>Stainless Steel<br>with Boron | I-1                        | 16.7669                      | -1.5                                  | 7.760  | +0.002   |
|   | I-2                        | 16.7736                      | -1.1                                  |  |  |
|   | I-3                        | 16.8037                      | -1.8                                  |  |  |
|   | I-4                        | 16.5024                      | -0.7                                  |  |  |
|   | I-5 (He)                   | 16.8292                      | -0.2                                  |  |  |
| Type 17-4 PH<br>Stainless Steel           | J-1                        | 16.6606                      | -0.8                                  | 7.750  | -0.001   |
|   | J-2                        | 16.6748                      | -0.5                                  |  |  |
|   | J-3                        | 16.6930                      | -1.0                                  |  |  |
|   | J-4                        | 16.6408                      | -0.5                                  |  |  |
|   | J-5 (He)                   | 16.7058                      | -0.6                                  |  |  |
| Type 304<br>Stainless Steel               | K-1                        | 16.8490                      | -0.3                                  | 7.935  | -0.008   |
|   | K-2                        | 16.8591                      | -1.8                                  |  |  |
|   | K-3                        | 16.8633                      | -0.3                                  |  |  |
|   | K-4                        | 16.8248                      | -0.3                                  |  |  |
|   | K-5 (He)                   | 16.8222                      | -0.4                                  |  |  |
| Tantalum                                  | M-1                        | 36.1254                      | -9.7                                  | 16.685   | -0.061   |
|   | M-2                        | 36.1815                      | -29.9                                 |  |  |
|   | M-3                        | 36.1617                      | -11.5                                 |  |  |
|   | M-4                        | 36.1365                      | -18.4                                 |  |  |
|   | M-5 (He)                   | 36.1470                      | +0.5                                  |  |  |

<sup>a</sup>For each material listed, the first four samples were exposed directly to the sodium of the reactor primary system. The fifth sample in each case was sealed in a capsule containing a helium atmosphere. The irradiation temperature was about 700°F, and the total residence time in position 12E1 of the core was about 52 months.

<sup>b</sup>Minus sign indicates decrease; plus sign indicates increase.

Only the samples of tantalum, T-1 tool steel, and Type 304 stainless steel showed appreciable reductions in density. The density of the remaining seven samples (three exposed in sodium and four in helium)

of each material will be checked in an attempt to determine whether or not there has been an actual reduction in density. The apparent increases in density of Stellite 6B and of Inconel X-750 probably are due to experimental error, but additional samples of these materials also may be checked.

c. Effect of Interstitial Elements in EBR-II Sodium

Last Reported: ANL-7655, p. 65 (Dec 1969).

(i) Nitridation of Type 304 Stainless Steel in Sodium  
(T. D. Claar)

The argon cover gas for the EBR-II primary system typically contains 0.25-0.50 wt % of nitrogen as an impurity. The bulk sodium under this cover gas is maintained at 700°F. During operation, this sodium is passed through the core of the reactor, from which it exits at 900°F. When the reactor power level is raised to 62.5 MWt, however, the temperature of the stainless steel in experimental subassemblies is expected to reach approximately 1200°F. If nitrogen is transported from the cover gas into the reactor core, interactions with stainless steel components may result at this temperature. A series of experiments was performed to evaluate the nitriding potential under conditions approximating those in the bulk tank and in the core.

By exposing Type 304 stainless steel for one week to sodium at a temperature of 1020°F and under a nitrogen cover gas, it was demonstrated initially that nitridation of stainless steel in sodium could occur. Metallographic examination of the foils revealed a nitride layer extending to a depth of  $4 \times 10^{-4}$  in. into the metal exposed to the sodium and  $7 \times 10^{-4}$  in. into the foil exposed to the cover gas above the sodium.

To simulate the reactor cover gas more closely, commercially prepared gas mixtures of 0.1 wt % and of 1.0 wt % nitrogen in pure argon were obtained. Seven-day tests were conducted in which Type 304 stainless steel foils were exposed to sodium at 1020 and 1200°F under each of the two A-N<sub>2</sub> cover gases. The surfaces exposed directly to the sodium were electropolished before testing to give an extremely smooth surface. After exposure, these surfaces were examined microscopically; they were found to contain massive nitrides at the grain boundaries and smaller nitride precipitates within the grains. Transverse sections of the foils showed nitrides at the grain boundaries near the sodium-exposed surface to a depth less than  $1 \times 10^{-3}$  in. The degree of surface nitriding increased with temperature and nitrogen content of the cover gas.

The closest duplication of the conditions in the EBR-II primary tank was obtained by exposing a 5-mil Type 304 stainless steel foil



to 700°F sodium under an A-1 wt %  $N_2$  cover gas for four weeks. Under these conditions, only a very slight amount of surface nitriding could be detected microscopically. Chemical analysis of the foil indicated no increase in nitrogen content above the level of 0.045 wt % in the as-received material. The material was not embrittled as a result of the exposure.

Nitriding of Type 304 stainless steel in liquid sodium under the conditions in the EBR-II tank appears to be an extremely slow process and should cause no significant degradation of EBR-II reactor components during their normal lifetimes. Examination of the EBR-II auxiliary gripper plug exposed at the sodium-argon interface in the tank suggests that nitridation above the sodium level may be more important than nitridation in the sodium. Further testing is planned to evaluate this possibility.

(ii) Tritium Distribution in Sodium-cooled Fast Reactors  
(S. Greenberg)

Tritium is produced in a sodium-cooled fast reactor as a result of the fission process and of the neutron-lithium interaction. (Lithium may be present in sodium as an impurity and/or a deliberately added oxygen getter.)

Since tantalum is an excellent hydrogen getter, it was thought reasonable to analyze the tantalum cladding of Source SO-1915, which had been exposed to primary sodium in EBR-II for about five years. During this period, the concentration of hydrogen in the tantalum increased from 2 to 13 ppm. Of the hydrogen in the tantalum after its exposure in EBR-II, 0.076 wt % was tritium. The initial tritium concentration of the tantalum was nil.

Measurable quantities of tritium apparently have reached the coolant sodium, thus having access to the cover gas and, in turn, to the atmosphere. This matter will continue to be studied.

## 7. Reactor Analysis, Testing, and Methods Development

Last Reported: ANL-7661, pp. 45-66 (Jan 1970).

### a. Improved Drop-rod Design (I. A. Engen, J. K. Long, and J. B. Waldo)

(i) Mechanical Tests. The existing EBR-II stainless steel drop rod utilizes the standard EBR-II control-rod scram system and a special stainless steel control subassembly. The rod is dropped by gravity and given a scram assist by 30-psig air pressure applied to a scram-assist cylinder at the top of the rod drive. The scram-assist pressure is effective over the full 14-in. drop-rod travel and accelerates the drive system at approximately 1.2 G over the first 10 in. of rod travel. In the last 4 in. of travel, the rod-and-drive system is gradually decelerated to rest by an oil-filled shock absorber.

To improve the quality of results from physics studies performed with the rod-drop method, it is desirable to remove the reactivity associated with the rod from the core as fast as physically possible. A study was made to establish whether or not the effective scram time could be reduced without a major redesign of the drop-rod drive system. It was immediately obvious that any large increase in maximum rod velocity would require complete redesign of the shock absorber and the drive. Therefore, a method was developed for raising the average rod velocity over the first 10 in. of drop without increasing the maximum velocity appreciably.

This method makes use of a higher scram-assist pressure and a modified scram air cylinder. The assist pressure was raised from 30 to 95 psig, which increased the theoretical acceleration from 1.2 to 2.6 G. Pressure-relieving ports were located in the wall of the air cylinder so that the air-assist pressure could be applied for only the first 3.5 in. of travel, and then the pressure would be relieved by venting to the atmosphere. From this point on, the rod would continue to accelerate due to gravity (minus friction and hydraulic effects) at approximately 0.87 G until it entered the shock absorber. Calculations indicated that this system would subtract at least 50 msec from the 210-msec drop time in the first 10 in. of travel of the present drop-rod system. The maximum velocity in the new system would be increased by 10%, but the increased kinetic energy would be offset by the fact that the air-assist pressure would no longer be acting on the rod while it is being decelerated.

To verify the accuracy of the calculations and to determine the feasibility of the vented-cylinder concept, a complete mockup of the control-rod-drive system was assembled from spare parts of control-rod drives. The mockup contained a complete assembly of a control-rod upper drive, including scram cylinder, scram clutch assembly, rack drive motor,

limit switches, etc., as well as a steel billet to simulate the weight of the rod-drive extension and the subassembly itself. An electrical power-supply and control cabinet also was fabricated to simplify operation of the drive.

The mockup was tested first with a standard scram cylinder and 30-psig air-assist pressure to see how closely it could duplicate the scram curves obtained with the reactor drop-rod system. The same time-versus-position recording system was used for the mockup as is used in the reactor installation. Table I.D.5 compares the results from the two systems.

TABLE I.D.5. Comparison of Results from Existing and Mockup Drop-rod Systems, Using Standard Air Assist

|   | Existing System | Mockup |
|---|-----------------|--------|
| 10-in. Scram Time, msec                   | 210             | 200    |
| Maximum Velocity, ft/sec                  | 7               | 7.3    |
| Maximum Acceleration, ft/sec <sup>2</sup> | 45              | 48     |
| Maximum Deceleration, ft/sec <sup>2</sup> | 130             | 145    |

The results indicate that the mockup simulated the actual installation acceptably well. The new scram system was installed on the mockup. This consisted of the special vented air cylinder, a new air accumulator tank, and provision for the 95-psig air pressure. Table I.D.6 gives the pertinent test data for the improved system. These results probably are representative of the changes that could be expected if the improved system were installed in the reactor. The 10-in. scram time was reduced 50 msec with negligible change in the shock loadings applied to the system components. No mechanical problems were observed.

Some details of the numerical procedures used to treat the data for rod position versus time are as follows:

1. Data were sampled at a rate of 200 samples per second. A two-point average of consecutive pairs of points was taken, resulting in a time separation of 0.01 sec.
2. Position data were normalized to a total rod travel of 14 in.
3. The data then were smoothed twice by a Hamming function operation.

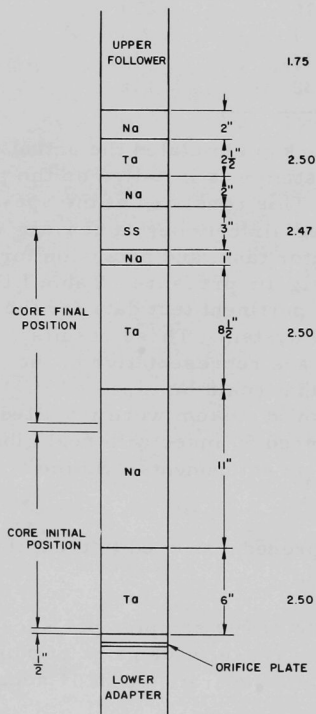
4. Initial points for each drop were selected as 0.02 sec prior to an indicated total movement of 0.06 in. This permits the starting point to be determined in a consistent fashion in spite of noise in the data.
5. Velocity and acceleration (not plotted) were determined by the formulas

$$v_i = (P_{i+1} - P_{i-1}) / 2\Delta t$$

and

$$a_i = (-P_{i-2} + 16 P_{i-1} - 30 P_i + 16 P_{i+1} - P_{i+2}) / \Delta t^2.$$

(ii) Physics Design for High Worth. The physics calculations for a drop rod based on tantalum have evolved to the point where a design for such a rod is being proposed to replace the present stainless steel rod. Figure I.D.5 shows the segments of the tantalum and reflective materials of which this rod is composed, as well as their required lengths, spacings, and cross-sectional areas.



This particular design was developed by a computer survey based on patterns of material worths obtained by the CANDID-PETULA codes (two-dimensional diffusion-perturbation theory). The program used for the survey was designed to calculate the worths of each half-inch increment of travel of rods composed of various lengths, spacings, and densities of segments. A set of lengths, spacings, and densities is called a design. If the worth increments for a design form a pattern which meets certain criteria, the computer prints the worth of each half-inch increment of travel and the total worth of 14 in. of travel. If the criteria are not met, the design is rejected, and the program moves to another design. The criteria which the design must meet are:

1. The first three half-inches of travel must be worth less than 0.1 lh each.

2. The total negative worth of 14 in. of travel must be greater than 12 lh.

Fig. I.D.5. Arrangement of Materials in Proposed Improved Drop Rod

3. No half-inch of travel must contribute a positive worth of more than 0.1 lh.
4. The last half-inch of travel must be worth less than 0.1 lh.

Final selection of a design is made by inspection of those designs meeting the above criteria.

It was found that the first three criteria could be met easily by adjusting the length and spacing of two tantalum segments in the lower portion of the rod. The final tail of the worth pattern could be shaped to meet criterion number four by adding two additional followers in the upper portion of the rod. Because these followers are relatively far from the core at the beginning of the drop, their inclusion does not distort the initial part of the pattern. Upper followers of nickel, stainless steel, and tantalum were examined, and it was found that a short length of stainless steel followed by a short length of tantalum would give the desired result. The design shown in Fig. I.D.5 actually has negligible worth over the last  $1\frac{1}{2}$  in. of travel, has a total worth of -15.7 lh, and adequately meets all other criteria as well. Because of the tantalum, this new design will reduce the reactivity of EBR-II by 46 lh relative to the present stainless steel rod.

The worth patterns used for the design of the rod were checked against experimental worth patterns determined with an EBR-II mockup on ZPR-3. The experimental comparisons indicated that the cross-section set calculated the worth of the tantalum about 10% too high. The correction for self-shielding is about 20% of the total worth. The design chosen is based on the experimental results.

(iii) Combined Effects of the New Physics Design with the Faster Mechanical Design. Figure I.D.6 shows the estimated reactivity change versus time for the tantalum drop rod, using either the standard

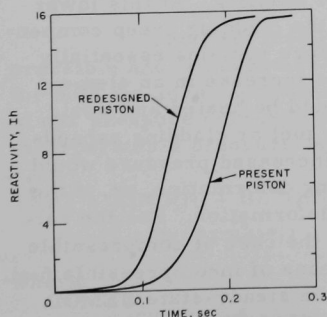


Fig. I.D.6

Reactivity-vs-Time Curves for Tantalum Drop Rod with Present Piston and with New Fast Design

air assist (present piston) or the new and faster air assist (redesigned piston). The decrease of about 50 msec in overall time for removal of the greater part of the reactivity with the faster piston is apparent. Also significant is the fact that, even if the removal of the first and last 0.2 lh are ignored because they are within the noise level, the removal time still is reduced from about 165 to 150 msec by the faster assist. Although this improvement may seem small, it is based on an idealization of the worth calculations. Positive and negative effects at the beginning and end of the drop actually may not cancel as calculated. The faster mechanical design, which has been tested and verified, will be

of further advantage, especially if the worth cancellation is less than ideal at the beginning of the drop. The 15-msec decrease should therefore be regarded as a minimum improvement attributable to the new mechanical design, with 50 msec as a maximum.

b. BEMOD Calculations of a Mark-IA Fuel Element Subject to an Overpower Transient (J. F. Koenig)

Calculations have been made using the BEMOD program to determine the response of a Mark-IA fuel element that has a 1.8 at. % burnup and is subjected to an overpower transient while at 62.5-MWt power.

The volume swelling of low-swelling ( $Si > 200$  ppm) Mark-IA U-5 wt % Fs fuel is assumed to be related by the equation

$$\Delta V/V = 0.04 \times bu + \text{smaller of (a) } 0.07887 (bu - 1.1)^2 \text{ or (b) } 0.7/[1 + (P/279)],$$

where  $\Delta V/V$  is the fractional increase in the fuel swelling,  $bu$  is the burnup in at. %, and  $P$  is the greater of the fuel-cladding contact pressure or the plenum pressure. The first term represents the growth of solid fission product and the second term (a) represents the breakaway swelling. The third term (b) represents the compressibility of the breakaway swelling. This last term is quite important because it can allow the fuel to compress during an overpower transient in which the pressure increases. Provisions have been made in the program to prevent the fuel from compressing during the overpower transients.

As the fuel swells, the bond sodium in the annulus is displaced to the volume usually occupied by the gas in the plenum. The resulting decrease in the volume of gas in the plenum, along with a slight amount of fission-gas release, will cause the pressure in the gas plenum to increase. With the present fuel-swelling model, the plenum pressure increases to about 2000 psi, which decreases the rate of fuel swelling. At this lower fuel-swelling rate, the volume increase due to the cladding creep compensates for additional fuel swelling, and the pressure remains essentially constant at about 2000 psi. If the power were to increase in an element with high plenum pressure, the bond sodium would be heated and would expand at about five times the rate at which the fuel or cladding expands, thereby increasing the plenum pressure. The increased pressure would be relieved by fuel compression, elastic cladding deformation, or, if the pressure is high enough, by inelastic cladding deformation. For the calculations made, fuel shrinkage was allowed for the case of compressible fuel and no fuel shrinkage was allowed for the case of incompressible fuel. The overpower transients were obtained from the steady-state BEMOD program by assuming quasi-steady-state conditions. This assumption was based on the short residence time ( $\approx 0.05$  sec) of the coolant in passing



the fuel-bearing section of the element, the relatively short time constant ( $\approx 0.3$  sec) of the fuel and cladding, and the relatively slow power addition (0.8%/sec) for a credible malfunction at power.

Figure I.D.7 shows the calculated increase in plenum pressure with burnup in a Mark-IA fuel element containing low-swelling fuel and an average and a high sodium level. The calculations were made for the center element in the 1N1 position at 62.5-MWt power. For the low-swelling fuel, the pressure and level of sodium in the gas plenum of the element at 1.8 at. % burnup (maximum) are such that an increase in power would not cause a large increase in pressure. For powers as high as 170% of the normal power, the pressure would increase from 120 psi to 270 psi. Since the stresses associated with these pressures are negligible, it is concluded that the design of the Mark-IA fuel element with low swelling fuel is adequate for large overpowers at 1.8 at. % maximum burnup.

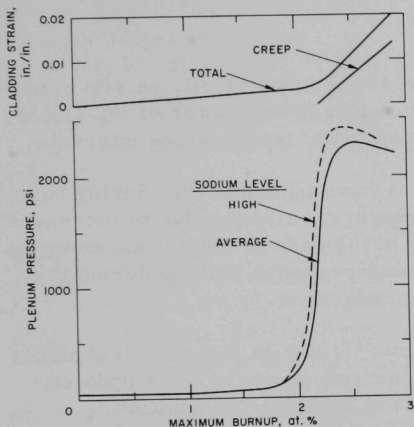


Fig. I.D.7. Calculated Increase in Plenum Pressure and Cladding Strain with Burnup of a Mark-IA Fuel Element Containing Low-swelling Fuel

#### c. BEMOD Modifications (C. C. Ford)

A substantial number of modifications have been made in the BEMOD code that was described by Jankus.\* The main purpose of the modifications has been for diversification, generalization, and updating of the program.

The first modification has been the incorporation of a compressible and temperature-dependent fuel-swelling model that can be used for both the core and blanket material. This model has a maximum limit of gas pressure corresponding to an upper limit on fuel compression and incorporates a pressure factor. The equation is

$$\text{TRIG} = \text{XING}(N) + \text{BU} * \text{Q}(N) * \text{TFB1} * \text{EXP}(\text{TFB2} * (\text{TFB3} - \text{TFB}(N))^2) / (1 + (\text{P}/\text{TFB4}) * (1 - \text{TFB5} * (\text{TFB3} - \text{TFB}(N))^2)), \quad (1)$$

where

TRIG = fuel swelling,

XING(N) = inexorable fuel growth for fuel section N,

\*Jankus, V. Z., BEMOD, A Code for the Lifetime of Metallic Fuel Elements, ANL-7586 (July 1969).



BU = burnup,

Q(N) = ratio of local linear power in section N to the average linear power of the whole fuel rod,

TFB(N) = average temperature of the fuel for section N,

P = pressure being exerted on section N, and

TFB

through TFB5 = constants.

The constants for the core have not been refined sufficiently as yet. The pressure-dependent compressibility factor [the denominator of Eq. (1)] is used to restrain the swelling during a prescribed temperature interval.

Previous BEMOD calculations have indicated that during burnup the fuel compresses when the plenum pressure increases due to increased operating temperatures. A modification of the code prevents this compression to allow determination of the maximum pressure buildup during temperature increases resulting from power increases.

Harkness has improved his model, now an iterative technique, for determining cladding swelling due to neutron fluence. This updated version has replaced his previous routine in BEMOD. In addition, a cladding-swelling data fit developed by PNL\* for annealed Type 304 or 316 stainless steel has been placed with Harkness' routine, with the option of using either one. PNL's equation is

$$\Delta V/V = 4.9 \times 10^{-49} \times (\text{nvt})^{1.71} \times 10 [(1.55 \times 10^4/T) - (5.99 \times 10^6/T^2)], \quad (2)$$

where  $\Delta V/V$  is the cladding swelling in percent and T is the average temperature of the cladding in °K.

A plotting program which uses the Calcomp plotter has been added to BEMOD.

Modifications also have been made that give the user the capability to read in change-case data (e.g., a different  $\Delta T$  for the coolant or a higher flux) after a specified limit has been reached and to continue calculations until a new limit is reached. Furthermore, the user now can stack two or more problems for processing at one time.

Other minor changes have been made involving a few output formats and control statements to provide a better-working program.

---

\*Claudson, T., PNL, private communication (Oct 1969).

d. Post-incident Recall System (J. R. Karvinen)

Temperature, flow, and neutron-flux data have been logged by the post-incident recall system (PIRS) during two recent scrams. Figure I.D.8 illustrates the information recorded from the instrumented sub-assembly (ISA) during the first of these scrams.\* This scram originated from an inadvertent disconnect of the excitation power to primary pump No. 1. Scaling factors, given in engineering units in the figure, may be used for amplitude conversion. With the exception of the ISA flow sensor, all channels operated satisfactorily. The flowmeter registered a decrease to 80% flow before the tape recorder reached saturation. However, the flow through the ISA actually dropped to zero. The large amount of noise recorded approximately 12 sec after the scram is the result of a splice in the magnetic tape.

The second scram was caused by an electrical-noise burst that tripped the reactor on a rate-of-change-of-flow safety circuit. The PIRS information demonstrated conclusively that the flow rate, as sensed by the flow sensors of the No. 1 primary pump and the ISA, did not change until after the scram. The ISA flowmeter registered an increase of 3.2% at 240 msec after the trip and a return to normal flow 160 msec later. Such behavior is expected because scrambling of the control rods from the core causes a momentary 3% increase in back pressure which, in turn, is manifested by an increase in flow through the ISA. Such information is reassuring because it indicates that the response times of the flow sensor and recording system are acceptably short.

Other ISA information recorded during the scram were temperature values for FCTC7, CTC7, and CTC3. For FCTC7, a time constant of 3.84 sec was measured. The changes in the readings for CTC3 and CTC7 were too small to permit an evaluation. The recordings for these two thermocouples, however, did display essentially the same characteristics as the recordings for FCTC7. In no case was a significant transport lag noted.

The readout from the ISA self-powered ion chamber registered a prompt drop of 8.5% during the scram. Since the output of the chamber depends on the neutron-activation rate for  $^{103}\text{Rh}$  (half-life of  $^{104}\text{Rh} = 42$  sec), the drop gives an accurate measurement of the prompt-gamma component. By subtracting background effects after a complete  $^{104}\text{Rh}$  decay from the decay data, it was shown that the signal from the ion chamber decayed with a 42-sec half-life. The contribution of fission-product gammas to the output measured 135 sec after the scram was shown to be approximately 15%. A check was made to compare the operating sensitivity of the chamber with the sensitivity reported by the manufacturer of the chamber. Assuming a neutron flux of  $2.5 \times 10^{15}$  n/cm<sup>2</sup>-sec at the chamber location and using the

\*The designations for the prefixes used in Fig. I.D.8 are: CTC--Cladding temperature; FCTC--Fuel-centerline temperature; ITC--Inlet-coolant temperature; N(T)--Ion-chamber current; and OTC--Outlet-coolant temperature.

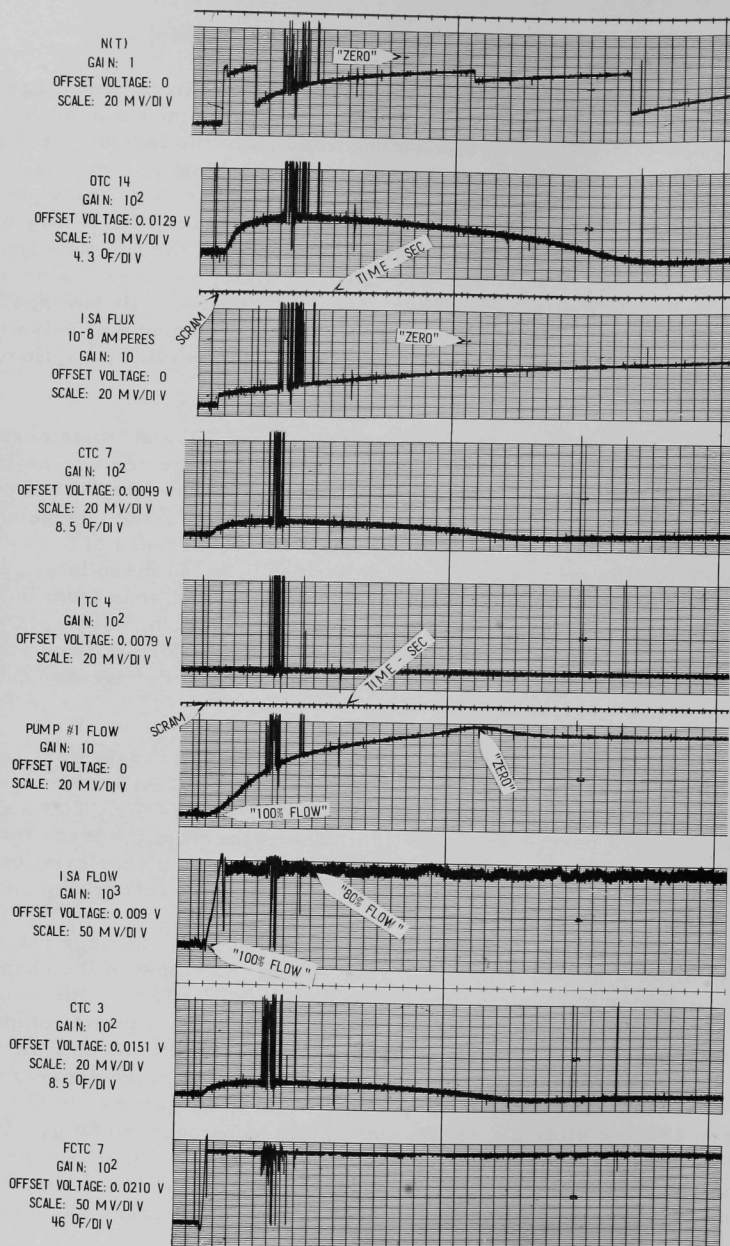


Fig. I.D.8. Output Data from the Instrumented Subassembly during a Scram as Logged by the Post-incident Recall System

manufacturer's reported sensitivity of  $1.2 \times 10^{-21}$  A/nv, a current of  $3 \times 10^{-6}$  A was expected at 58 MWt. The actual current output, as measured with an EG&G Model 920 picoammeter, was  $6 \times 10^{-8}$  A.

e. Data for ISA Sensors during a Reactor Transient  
(J. R. Karvinen)

Recordings of data from various ISA sensors were made during rod drops at 50 MWt in Run 38A. Three tests were conducted. These are designated as test numbers 1, 2, and 4 in Table I.D.7, which summarizes the ISA readout information. On some occasions, system noise obscured temperature data, making it impossible to establish the transport lag associated with the thermocouple response. Such instances are identified by a question mark in the column listing transport lags.

TABLE I.D.7. Readout of Data from Instrumented Subassembly during 50-MWt Rod Drops in Run 38A

| Test Number | Channel | Sensor      | Offset (mV)            | Steady-state Value (°C) <sup>a</sup> | Transient Amplitude (mV) | Transient (°C) | Transport Lag (sec) | Total Time (sec) |
|-------------|---------|-------------|------------------------|--------------------------------------|--------------------------|----------------|---------------------|------------------|
| 1           | 2       | OTC-5       | 16.55                  | 404                                  | $18 \times 10^{-2}$      | -4.3           | ?                   | 51.0             |
| 2           | 2       | OTC-5       | 16.55                  | 404                                  | $21 \times 10^{-2}$      | -5.0           | ?                   | 74.5             |
| 4           | 2       | OTC-5       | 16.55                  | 404                                  | $18 \times 10^{-2}$      | -4.3           | ?                   | 50.0             |
| 1           | 3       | OTC-14      | 16.33                  | 398                                  | $16 \times 10^{-2}$      | -3.8           | ?                   | 51.0             |
| 2           | 3       | OTC-14      | 16.33                  | 398                                  | $18.5 \times 10^{-2}$    | -4.4           | ?                   | 74.5             |
| 4           | 3       | OTC-14      | 16.33                  | 398                                  | $16 \times 10^{-2}$      | -3.8           | ?                   | 50.0             |
| 1           | 4       | FCTC3       | 24.39                  | 1326                                 | $95 \times 10^{-2}$      | -51.0          | 1                   | 51.0             |
| 2           | 4       | FCTC3       | 24.39                  | 1326                                 | $115 \times 10^{-2}$     | -61.0          | 1                   | 74.5             |
| 4           | 4       | FCTC3       | 24.39                  | 1326                                 | $100 \times 10^{-2}$     | -53.0          | 1                   | 50.0             |
| 1           | 5       | SWTC3       | 16.20                  | 395                                  | $9 \times 10^{-2}$       | -2.1           | 0                   | 51.0             |
| 2           | 5       | SWTC3       | 16.20                  | 395                                  | $12 \times 10^{-2}$      | -2.8           | 0                   | 74.5             |
| 4           | 5       | SWTC3       | 16.20                  | 395                                  | $9 \times 10^{-2}$       | -2.1           | 0                   | 50.0             |
| 1           | 6       | FCTC7       | 23.26                  | 1256                                 | $95 \times 10^{-2}$      | -50.0          | 1                   | 51.0             |
| 2           | 6       | FCTC7       | 23.26                  | 1256                                 | $115 \times 10^{-2}$     | -61.0          | 1                   | 74.5             |
| 4           | 6       | FCTC7       | 23.26                  | 1256                                 | $95 \times 10^{-2}$      | -50.0          | 1                   | 50.0             |
| 1           | 7       | SWTC7       | 13.92                  | 341                                  | $7 \times 10^{-2}$       | -1.7           | 0                   | 51.0             |
| 2           | 7       | SWTC7       | 13.92                  | 341                                  | $10 \times 10^{-2}$      | -2.4           | 0                   | 74.5             |
| 4           | 7       | SWTC7       | 13.92                  | 341                                  | $7 \times 10^{-2}$       | -1.7           | 0                   | 50.0             |
| 1           | 8       | FCTC17      | 20.7                   | 1124                                 | $66 \times 10^{-2}$      | -34.0          | 0                   | 51.0             |
| 2           | 8       | FCTC17      | 20.7                   | 1124                                 | $78 \times 10^{-2}$      | -40.0          | 0                   | 74.5             |
| 4           | 8       | FCTC17      | 20.7                   | 1124                                 | $70 \times 10^{-2}$      | -36.0          | 0                   | 50.0             |
| 1, 2, 4     | 9       | ITC4        | No change during drops |                                      |                          |                | 0                   | -                |
| 1           | 10      | SWTC17      | 17.4                   | 423.7                                | $14 \times 10^{-2}$      | -3.3           | 0                   | 51.0             |
| 2           | 10      | SWTC17      | 17.4                   | 423.7                                | $22 \times 10^{-2}$      | -5.2           | 0                   | 74.5             |
| 4           | 10      | SWTC17      | 17.4                   | 423.7                                | $14.5 \times 10^{-2}$    | -3.4           | 0                   | 50.0             |
| 1, 2, 4     | 11      | Total Flow  | No change during drops |                                      |                          |                | 0                   | -                |
| 1           | 12      | Ion Chamber | 6.125                  | 50 MWt                               | 390 <sup>b</sup>         | -6.36 MWt      | 0                   | 51.0             |
| 2           | 12      | Ion Chamber | 6.125                  | 50 MWt                               | 440 <sup>b</sup>         | -7.17 MWt      | 0                   | 74.5             |
| 4           | 12      | Ion Chamber | 6.125                  | 50 MWt                               | 410 <sup>b</sup>         | -6.7 MWt       | 0                   | 50.0             |

<sup>a</sup>Add 24.5°C for junction temperature.

<sup>b</sup>Instant drop of 220 mV, equivalent to 1.8 MWt.

f. Prediction of Temperature and Burnup of  $B_4C$  of 50% and 90% Enrichment in a Seven-tube Absorber-Follower Control Rod  
(R. K. Lo)

An analysis was made to predict the burnup and axial temperature distribution in  $B_4C$  of 50 and 90% enrichment in a seven-tube absorber-follower control rod when the cluster is placed in the following three positions: (1) tubes fully inserted into the reactor core, (2) bottom of tubes 4 in. above midcore, and (3) bottom of tubes at top of the reactor core.

The central tube of the cluster was considered because it is likely to be the hottest one among the seven tubes. The reactor was assumed to be operating at 62.5 MWt.

For the analysis, the absorber section of the control rod consisted of a seven-tube cluster of  $B_4C$ , approximately 36.5 in. long. Each stainless steel tube had an outside diameter of 0.625 in. and an inside diameter of 0.555 in. Each contained a stack of fourteen 1-in.-long, 0.549-in.-dia  $B_4C$  pellets; a  $1\frac{1}{8}$ -in.-long preloading spring to prevent the  $B_4C$  pellets from shifting when the control rod moved and to permit  $B_4C$  growth; and an 8-in.-high stainless steel shield section to protect the upper part of the reactor structure from radiation. The balance of the space within the tube--a  $9\frac{1}{2}$ -in.-high gas volume--was used to accommodate the helium given off by neutron-induced transmutation of the boron-10. Each tube was approximately 36.5 in. long, was filled with helium, and had a 0.030-in.-dia spacer wire wrapped helically around its exterior.

The theoretical density of natural  $B_4C$  is 2.52 g/cc; of  $B_4C$  with 50% enrichment, 2.45 g/cc; and of  $B_4C$  with 90% enrichment, 2.39 g/cc. The packing density was assumed to be 93%. The thermal conductivity of  $B_4C$  was taken to be 13.9 Btu/hr-ft-°F and was assumed to remain constant.

At 62.5-MWt reactor operation, the rate of gamma-ray heating of stainless steel at the midcore was taken to be 29.5 W/cc.\* The rate of heat generation due to  $(n, \alpha)$  reaction at the midcore was taken to be 35.5 W/cc for  $B_4C$  with 50% enrichment and 63.8 W/cc for  $B_4C$  with 90% enrichment, at a packing density of 93%. The rate of gamma-ray heating of  $B_4C$  at the midcore was calculated to be 9.08 W/cc.

The axial variation of heat generation due to  $(n, \alpha)$  reaction and gamma-ray heating was taken from results computed with the DOT 5 neutron-transport computer code.\*\*

The design flow rate of sodium through the control-rod sub-assembly is 61 gpm. Assuming the flow rate of sodium around the central

\* Guide for Irradiation Experiments in EBR-II, Revision 3 (July 1969).

\*\* Miller, L. B., private communication (Jan. 27, 1970).

tube to be 70% of the average and accounting for the variation of flow rate with respect to the control-rod positions,\* the following rates of sodium flow around the central tube were calculated:

| Position of B <sub>4</sub> C Absorber | Flow Rate    |                   |
|---------------------------------------|--------------|-------------------|
|                                       | Relative (%) | Actual (gpm/tube) |
| Fully in Core                         | 68           | 4.2               |
| 4 in. above Midcore                   | 92           | 5.6               |
| Top of Core                           | 100          | 6.1               |

The total power of the 61-pin control-rod subassembly is 519 kW. The temperature of the sodium rises 232°F when the fuel pins are fully inserted into the core.

Using the information given above as input to a heat-transfer computer code, the temperatures of the sodium, the cladding, and the B<sub>4</sub>C pellets with 50 and 90% enrichment at the three control-rod positions were calculated. The highest temperatures were found to occur when the B<sub>4</sub>C absorber is at the top of the core. It appears that the maximum center temperature of the B<sub>4</sub>C is about 1000 to 1050°F, which is well below the melting point (~3700°F) of B<sub>4</sub>C.

Pitner of Battelle Northwest Laboratory recently reported experimental results of irradiation of natural B<sub>4</sub>C in EBR-II. After six months of irradiation at temperatures of about 1100°F, the fission-gas release was about 30% at 1.58 at. % burnup.

With allowable stress of 9400 psi and 30% fission-gas release, the B<sub>4</sub>C containment tube could sustain 3.1 at. % burnup for B<sub>4</sub>C with 50% enrichment and 1.7 at. % burnup for B<sub>4</sub>C with 90% enrichment.

- g. Reactivity Effect of Radial Movement of Nickel Reflector in EBR-II (D. E. Meneghetti and K. E. Phillips)

The calculations reported in ANL-7661, pp. 55-56, were repeated using the 22-group set 238. The reactivity effects calculated in S<sub>2</sub> and S<sub>4</sub> approximations are -0.056%  $\Delta k/k$  and -0.059%  $\Delta k/k$ , respectively.

- h. Spatial Variation of Flux Spectrum in Calculations for Stainless Steel Damage (J. Honecamp and G. H. Golden)

A series of calculations is being made in which different correlations and models are being used to deduce shapes of axial flux from

\*Hutter, E., "Higher Worth Control Rod, Task 12," EBR-II Technical Memo, Transmittal No. 25 (May 29, 1969).



measured values of  $\Delta D/D$  and corresponding computed wall temperatures. The resulting flux distributions tend to be more peaked than the total flux distributions given by neutronics calculations. This suggested that the spatial variation of the flux distribution with energy must be accounted for in rigorous treatments of swelling of stainless steel induced by fast flux.

To examine this hypothesis further, a calculation was made to estimate the ratio of the rate of damage production at  $x/\ell = 0.464$  to that at  $x/\ell = 0.036$  in Row 4 of the EBR-II core. Group fluxes were taken from an r-z diffusion-theory calculation for the Run-31F core. In this calculation, a special 22-group cross-section set (JM31F) was used that has 0.125 lethargy spacing for  $E \geq 1.35$  MeV.\* Group damage cross sections for iron were estimated from work of Jenkins,\*\* who used the Kinchin-Pease model to estimate the number of secondary displacements caused by a primary knock-on.

The ratio of total flux at  $x/\ell = 0.464$  to that at  $x/\ell = 0.036$  was found to be 1.31. The corresponding ratio of total damage rates, however, was computed to be 1.48. This supports the contention that consideration should be given to spatial variation of neutron spectrum in a rigorous treatment of swelling of stainless steel induced by fast flux.

i. Analysis of a Mixed Core (J. L. Gillete)

Neutronic and thermal-hydraulic analyses have been made of an EBR-II core loading similar to that in Run 37A. The power level was set at 50 MWt, and the loading was as shown in Table I.D.8. The driver,

TABLE I.D.8. Loading for Analysis of Mixed Core

| Row No. | Subassembly Numbers and Types                    |
|---------|--|
| 1       | 1 driver   |
| 2       | 3 driver and 3 structural experiment             |
| 3       | 9 driver, 2 safety, and 1 oxide                  |
| 4       | 11 driver and 7 oxide                            |
| 5       | 10 driver, 11 control, 2 oxide, and 1 structural |
| 6       | 23 driver, 5 oxide, and 2 blanket                |
| 7       | 2 oxide, 9 structural, and 25 blanket            |
| 8-16    | All blanket                                      |

\*Madell, J. T., et al., Analysis of Recent Dosimetry Experiments in EBR-II, Trans. Am. Nucl. Soc. 12(2), 939 (1969).

\*\*Jenkins, J. D., Primary Recoil Atom Spectra and Displacement Damage Cross Sections from ENDF/B Data (draft submitted to Nucl. Sci. and Eng. for publication).



control, safety, and blanket subassemblies were of the usual construction, and the oxide subassemblies were assumed to have 61 fuel pins containing a mixture of  $\text{UO}_2$  and  $\text{PuO}_2$ .

The neutronics analysis was made through the use of the MACH-1 diffusion-theory code.\* The method of analysis was first to do a composition search in radial geometry with the first six rows homogenized, the seventh row as is, and the remaining rows considered together (i.e., a three-region problem was solved, with composition searches made for the  $^{235}\text{U}$  in the first two regions). The buckling ( $B_z$ ) in this problem was considered to be independent of both region and group, and was determined by the relation

$$B_z^2 = \pi^2 / H_{\text{ext}}^2,$$

where the extrapolated height ( $H_{\text{ext}}$ ) is estimated on the basis of previous work. The results of this problem include information for deducing bucklings in the radial direction.

A second MACH-1 problem then was run with the homogenized core (Rows 1 through 6) and the homogenized axial reflector. A  $k$  calculation was made in axial geometry, using the composition and the transverse buckling in the core region as determined in the previous problem and the transverse buckling in the axial reflector given by the group-independent equation

$$B_r^2 = 2.4048^2 / R_{\text{ext}}^2,$$

where the extrapolated radius ( $R_{\text{ext}}$ ) is estimated from previous work. This calculation yielded group-dependent bucklings in the axial direction, which were in turn read into the next problem, a composition search in radial geometry with the isotope concentrations given on a row-by-row basis. The search in this problem was made only for the uranium in the oxide subassemblies so that the enrichment necessary for criticality could be easily seen.

The thermal-hydraulic analysis was done with the SNAFU code. This code was used because of the various orificing options available and because of its ability to consider the various kinds of subassemblies within a row independently of each other.\*\*

The power apportionment was determined on the basis of the fission integrals and atom-number densities in each region. This apportionment showed that a total of 35.162 MWt was generated in the driver subassemblies, 7.305 MWt in the oxides, and the remainder of the 50 MWt in the control, safety, and blanket subassemblies.

\* Meneley, D. A., et al., MACH 1, A One-dimensional Diffusion-theory Package, ANL-7223 (June 1966).

\*\* Reactor Development Program Progress Reports for November 1969, ANL-7640, pp. 65-66, and for December 1969, ANL-7655, pp. 72-73.

The first thermal-hydraulics problem considered was that of the metal driver subassemblies. Coolant mass-flow rates were taken from the EBR-II Hazards Report Addendum.\* The resulting mean coolant-outlet temperatures under nominal design conditions were:

| <u>Row</u> | <u>Temperature (°F)</u> |
|------------|-------------------------|
| 1          | 852.8                   |
| 2          | 852.6                   |
| 3          | 865.5                   |
| 4          | 898.2                   |
| 5          | 906.7                   |
| 6          | 882.4                   |

These outlet temperatures then were used as input to additional thermal-hydraulics problems in which the oxide subassemblies were considered. The subassemblies were considered to be orificed to produce a uniform outlet temperature from all subassemblies of the row, and the flow rates were determined accordingly. The mean coolant-outlet temperatures for the oxide subassemblies will of course be the same as those for the drivers in the same row, but other temperatures may be examined. Table I.D.9 gives the maximum cladding temperature, maximum fuel temperature, and peak coolant-outlet temperature for both types of subassemblies. The maximum fuel temperatures in the oxide subassemblies were determined through the use of the General Electric oxide-restructuring model, which predicts somewhat higher maximum fuel temperatures than other available models. The peak coolant temperatures differ from the mean coolant-outlet temperatures recorded above because of the lower mass-flow rates in the center of a subassembly. These lower flow rates result from the can-wall effects and are analyzed in the FLODIST subroutine.

TABLE I.D.9. Calculated Temperatures (°F)  
in Mixed Core at 50 MWt

| Row No. | Drivers           |                   |                   | Oxides            |                   |                   |
|---------|-------------------|-------------------|-------------------|-------------------|-------------------|-------------------|
|         | T <sub>Cool</sub> | T <sub>Clad</sub> | T <sub>Fuel</sub> | T <sub>Cool</sub> | T <sub>Clad</sub> | T <sub>Fuel</sub> |
| 1       | 891.7             | 932.7             | 1044.7            | -                 | -                 | -                 |
| 2       | 891.5             | 932.0             | 1041.9            | -                 | -                 | -                 |
| 3       | 907.7             | 946.9             | 1050.4            | 918.0             | 971.6             | 3449.0            |
| 4       | 948.7             | 984.8             | 1076.3            | 961.0             | 1010.1            | 3300.6            |
| 5       | 959.4             | 991.0             | 1070.2            | 972.2             | 1015.0            | 3072.8            |
| 6       | 928.9             | 955.4             | 1021.1            | 940.2             | 975.9             | 2625.7            |

\*Koch, L. J., et al., Hazards Summary Report, EBR-II (Addendum), ANL-5719 (Addendum) (June 1962).

The temperatures calculated indicate that under nominal conditions no adversely high temperatures are encountered in either type of subassembly and that the coolant-outlet temperatures from adjacent subassemblies are not so different as to cause undue thermal bowing effects.

Each of the thermal-hydraulic problems was solved with an overpower factor of 1.25, which increases the reactor power to 62.5 MWt. The temperature calculations then were repeated for this power level, with the coolant flow rates remaining at the values calculated for 50-MWt operation. Table I.D.10 lists the resulting temperatures of interest. (Note that the mean coolant-outlet temperature,  $T_{\text{bulk}}$ , is again the same in the drivers and oxides.)

TABLE I.D.10. Calculated Temperatures ( $^{\circ}\text{F}$ ) in Mixed Core at 62.5 MWt

| Row No. | Drivers           |                   |                   |                   | Oxides            |                   |                   |                   |
|---------|-------------------|-------------------|-------------------|-------------------|-------------------|-------------------|-------------------|-------------------|
|         | $T_{\text{Bulk}}$ | $T_{\text{Cool}}$ | $T_{\text{Clad}}$ | $T_{\text{Fuel}}$ | $T_{\text{Bulk}}$ | $T_{\text{Cool}}$ | $T_{\text{Clad}}$ | $T_{\text{Fuel}}$ |
| 1       | 891.0             | 939.7             | 990.1             | 1130.0            | -                 | -                 | -                 | -                 |
| 2       | 890.8             | 939.4             | 989.2             | 1126.4            | -                 | -                 | -                 | -                 |
| 3       | 906.9             | 959.6             | 1007.8            | 1137.1            | 906.9             | 972.5             | 1038.2            | 3969.3            |
| 4       | 947.7             | 1010.9            | 1055.2            | 1169.5            | 947.8             | 1026.3            | 1086.3            | 3781.9            |
| 5       | 958.3             | 1024.2            | 1063.0            | 1162.0            | 958.4             | 1040.3            | 1092.6            | 3483.5            |
| 6       | 928.0             | 986.2             | 1018.7            | 1100.9            | 928.0             | 1000.3            | 1044.0            | 3126.7            |

j. Rate of Gamma-heat Generation in EBR-II with Stainless Steel and Nickel Reflectors (L. B. Miller and R. E. Jarka)

The rate of energy deposition in the EBR-II core, reflector, and blanket regions as a function of radius is shown in Figs. I.D.9 and I.D.10. The heat-generation rate, in  $\text{kW}/\text{cm}^3$ , is shown for the core mid-plane, along the top of the core, and 18 cm above the top of the core.

These results were obtained by first calculating the neutron flux as a function of RZ for 22 energy groups. The gamma source rate produced by this neutron flux then was calculated and used as the source for a 20-energy-group gamma-transport problem. The two-dimensional multigroup photon flux was used with gamma-energy absorption coefficients to compute the heat-generation rates shown in the figures. The neutron-transport problem was solved with transport cross sections, using the  $S_2$  approximation. The photon-transport problem was solved with  $P_3$  scattering in the  $S_6$  approximation.

The compositions of all the subassemblies in each row were averaged in computing the atomic densities used for each row in the calculation. This results in some variation of atomic density from one row to the next. The discontinuities in heating rate shown in the figures are due to this variation in atom densities. Table I.D.11 lists the atomic densities that were used in the calculations.

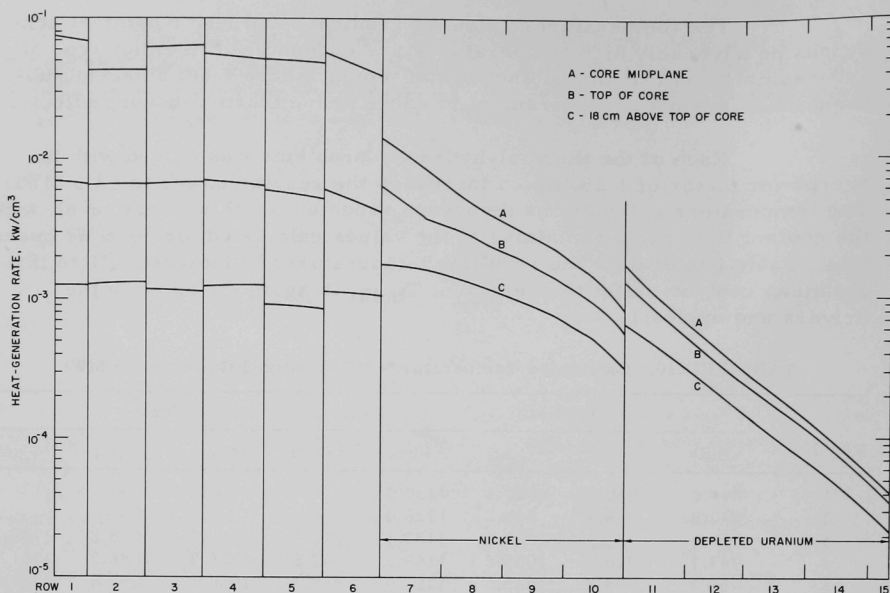


Fig. I.D.9. Rate of Gamma-heat Generation in EBR-II with Four Rows of Nickel

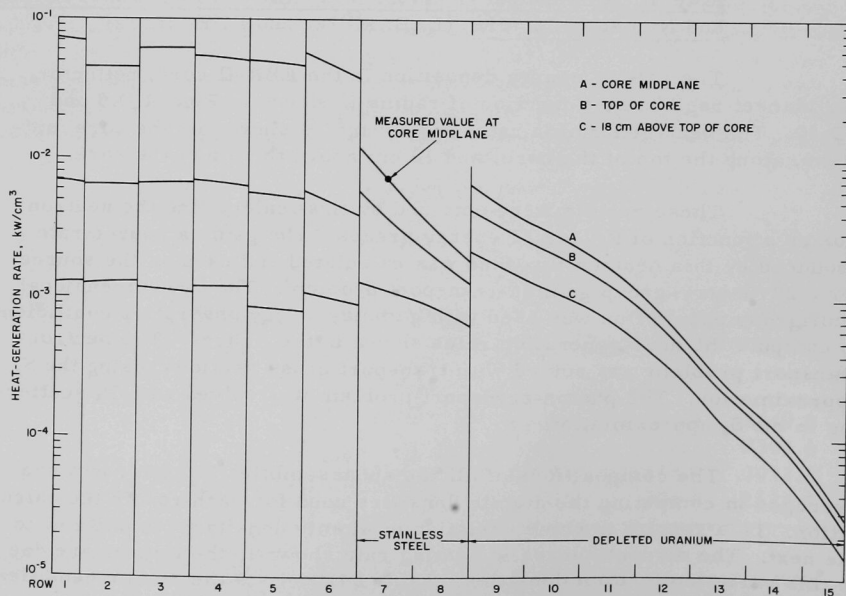


Fig. I.D.10. Rate of Gamma-heat Generation in EBR-II with Two Rows of Stainless Steel

TABLE I.D.11. Atomic Densities of Ni, Fe, Cr, and Na in the Nickel and Stainless Steel Reflector Regions

|    | Nickel Reflector |           |           | Stainless Steel Reflector |
|----|------------------|-----------|-----------|---------------------------|
|    | Center           | Upper     | Lower     |                           |
| Ni | 0.0703897        | 0.0384    | 0.0239    | 0.00615                   |
| Fe | 0.0049416        | 0.029     | 0.0399    | 0.0485                    |
| Cr | 0.001389         | 0.0079    | 0.0196    | 0.0139                    |
| Na | 0.0031553        | 0.0031553 | 0.0031553 | 0.00432                   |

Figure I.D.9 shows the gamma-heating rate in EBR-II with four rows of nickel reflector, as a function of R and Z. Figure I.D.10 shows the gamma-heating rate with the stainless steel reflector.

The calculated value for gamma-heating rate at the center of the reactor is  $75 \text{ W/cm}^3$ . The heating rate calculated from the curves in the current Guide for Irradiation Experiments in EBR-II would be  $58 \text{ W/cm}^3$ . However, the calculated value for the gamma-heating rate in Row 7 is within a few percent of the value determined by melt-wire experiments, which was  $0.85 \pm 0.20 \text{ W/g}$  of iron at 45 MWt.\* This is equivalent to a gamma-heating rate in the stainless steel reflector of  $7.32 \text{ W/cm}^3$  at 50 MWt, which is identified as the measured value in Fig. I.D.10. The agreement between the calculated and measured value is considered good.

The neutron-transport problems were normalized to a total reactor power of 50 MWt based on 200 MeV/fission. The central fission rate was found to be  $2.8246 \times 10^{13}$  fissions/sec-cc, or  $0.970 \times 10^{13}$  fissions/sec-g of pure  $^{235}\text{U}$ . (The Guide for Irradiation Experiments in EBR-II shows  $0.893 \times 10^{13}$  fissions/sec-g of pure  $^{235}\text{U}$ --a difference of 8.5%.)

The eigenvalue of the neutron-transport problem for EBR-II with four rows of nickel is 1.07204. This is 5.0% higher than the eigenvalue for the same core configuration (Run 31F) with a depleted-uranium blanket. If the core loading used in the calculation is adjusted to critical by removing fuel elements at the edge of the core, the neutron flux will be 10% higher. Since the gamma-heating rate is directly proportional to the neutron flux, the gamma-heating rates shown in Fig. I.D.9 also will be 10% higher.

- k. Flux and Power Contours in a Typical EBR-II Core Loading  
(L. B. Miller, R. E. Jarka, and P. Fullerton)

Further studies have been made of the asymmetry of the flux and fission rate in EBR-II. Figure I.D.11 shows the microscopic  $^{235}\text{U}$

\*Bloom, E. E., ORNL, private communication (Sept. 22, 1967).

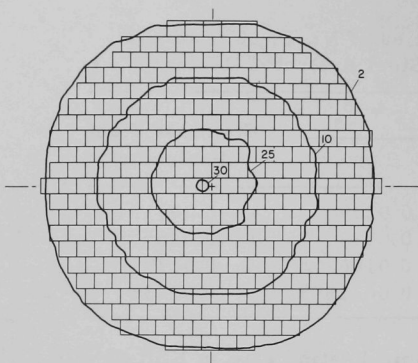


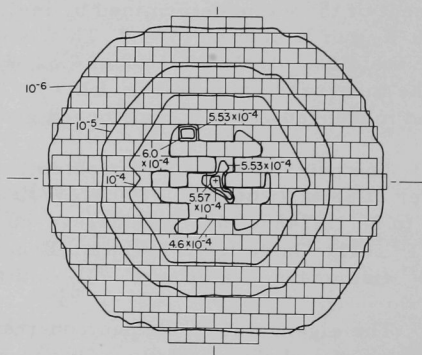
Fig. I.D.11. Contour Map of Microscopic  $^{235}\text{U}$   
Fission Rate at Core Midplane in  
EBR-II Run 29D

evident in this figure is due to variations in the amount of fissile material in the subassemblies in the core.

fission-rate contours at the core midplane in Run 29D. The peak is located at the boundary between Rows 1 and 2, as is typical in recent core loadings. Near the core center, points of equal fission rate lie on contours approximating circles centered on the peak. Near the interface of the core and blanket, the contours tend to assume the hexagonal shape of the interface. In the blanket region, the contours are nearly circular, with foci at the reactor center.

Figure I.D.12\* shows the rate of fission-neutron emission in Run 32B. The larger asymmetry

Fig. I.D.12  
Contour Map of Rate of  
Fission-neutron Emission  
in EBR-II Run 42B



1. Flux and Fission-rate Depression in B7, A19, B37, and F37 Subassemblies (L. B. Miller and R. E. Jarka)

Flux-depression factors have been computed for a number of typical experimental subassemblies by comparing the flux in each experimental subassembly with the flux that would be present in a driver subassembly located at the same position.

First, a neutron-transport (DOT 5) calculation was made to determine the six-group flux in each of the subassemblies in EBR-II Run 38B.

\*A figure (I.D.7) having the same caption was in the Progress Report for December 1969, ANL-7655, p. 67. That figure inadvertently was a repeat of Fig. I.D.6 on the same page of ANL-7655, the contour map of low-energy flux in EBR-II Run 32B.

Then, a second calculation was made to determine what the flux in each subassembly would be if experimental-irradiation Subassemblies XO54 and XO51, located on opposite sides of the core center, were replaced by driver subassemblies. A third calculation was performed with the isolated experimental-irradiation subassemblies--XO57, XO50, XO64, XO40, and XO58--replaced by driver subassemblies. All the problems were run in 360° XY geometry with cross-section set 23806.

The ratio of the flux in each experimental subassembly to the flux in the driver subassembly replacing it in the core is considered to be the flux-depression factor. Table I.D.12 shows a flux-depression factor for each of six neutron-energy regions in each subassembly. The table also shows the depression in the  $^{235}\text{U}$  fission rate per atom.

TABLE I.D.12. Flux- and Fission-rate-depression Factors for EBR-II Run 388

| Type of Subassembly | Subassembly No. | Fuel Loading (g) |                   |                  | Subassembly Position | Environmental Subassemblies <sup>a</sup>     | <sup>235</sup> U Fission-rate-depression Factor | Flux-depression Factor      |       |       |       |       |      |  |
|---------------------|-----------------|------------------|-------------------|------------------|----------------------|--|---|-----------------------------|-------|-------|-------|-------|------|--|
|                     |                 | <sup>235</sup> U | <sup>239</sup> Pu | <sup>238</sup> U |                      |  |   | Lower Energy of Group (MeV) |       |       |       |       |      |  |
|                     |                 |                  |                   |                  |                      |  |   | 2.23                        | 0.821 | 0.302 | 0.111 | 0.041 | 0    |  |
| B7                  | XO57            | 0                | 0                 | 0                | 2B1                  | D, D, L, D, D, D                             | 0.961   | 0.70                        | 0.84  | 0.95  | 1.01  | 1.07  | 1.34 |  |
| F37                 | XO51            | 14               | 556               | 1966             | 3A2                  | L, D, C, D, D <sup>2</sup> , D               | 0.972   | 0.83                        | 0.87  | 0.93  | 1.02  | 1.08  | 1.23 |  |
| A19                 | XO50            | 737              | 203               | 80               | 4C2                  | D, D, D, L, C, D <sup>2</sup>                | 0.995   | 0.92                        | 0.94  | 0.96  | 1.02  | 1.06  | 1.19 |  |
| A19                 | XO64            | 939              | 311               | 108              | 4F2                  | D, D, L, D, C, D                             | 1.001   | 0.94                        | 0.95  | 0.96  | 1.03  | 1.07  | 1.21 |  |
| F37A                | XO54            | 1747             | 553               | 213              | 4E1                  | D <sup>1</sup> , D <sup>2</sup> , D, C, D, L | 1.013   | 1.03                        | 0.98  | 0.97  | 1.03  | 1.05  | 1.13 |  |
| F37                 | XO58            | 1811             | 581               | 201              | 6F1                  | C, D, B, B, B, D                             | 1.041   | 1.05                        | 1.01  | 0.99  | 1.04  | 1.07  | 1.16 |  |
| B37                 | XO40            | 1918             | 581               | 180              | 5B2                  | D, D <sup>1</sup> , C, D, D, C               | 1.019   | 1.04                        | 0.99  | 0.97  | 1.03  | 1.06  | 1.15 |  |

<sup>a</sup>Six subassemblies surrounding the position of interest (clockwise starting with S/A nearest the center of the core: B = Blanket; C = Control rod; D = Driver; D<sup>1</sup> = 66%-enriched driver; D<sup>2</sup> = 1/2 driver fuel--1/2 stainless steel; H = Heavily loaded fueled experimental S/A; and L = Lightly loaded fueled experiments or structural S/A.

The flux-depression factor depends primarily on the amount of fissile and fertile isotopes in the experimental subassembly relative to the amount of fissile and fertile material in the dominant driver subassemblies. Although the experimental subassemblies contain less fissile material than normal driver subassemblies, the more heavily loaded experiments produce local peaks rather than depressions in the flux and fission rates. These peaks are due to the greater worth of the plutonium relative to the  $^{235}\text{U}$  in the drivers and to the smaller amount of  $^{238}\text{U}$ , both of which contribute to an increase in the average value of  $\eta$  (neutrons emitted per neutrons absorbed).

The high-energy ( $>2.23$  MeV) flux-depression factor ranges between 0.70 in the structural test Subassembly XO57 and 1.05 in the highly enriched Subassembly XO58. The high-energy  $^{235}\text{U}$  fission-rate-depression factor ranges between 0.961 in XO57 and 1.041 in XO58.

The effect of environment on the flux depression in an experimental subassembly is most obvious in the case of XO58, which was located on the edge of the core and adjacent to three blanket subassemblies. Since the fuel loading in XO58 is similar to the fuel loading in XO54 and XO40, the



subassembly would have produced a similar flux perturbation if it had been located in Row 4 or 5. It produced a larger relative flux perturbation than XO54 or XO40 because in Row 6 it tends to dominate its environment. This same phenomena (an unusually large flux perturbation) also will occur to a smaller degree in Rows 1 to 5 if the experimental subassembly is surrounded by structural test subassemblies.

These flux- and fission-rate-depression factors are average values which apply to each experimental subassembly as a whole. The flux and fission-rate perturbation is of the order of 20 to 30% greater at the center of each subassembly.

#### 8. Driver Fuel Development (C. M. Walter)

##### a. High Burnup Encapsulated Irradiations

Last Reported: ANL-7661, p. 67 (Jan 1970).

##### (i) Analytical Burnup Results of Encapsulated Elements (W. N. Beck)

Selected sections of Mark-IA and Mark-II fuel pins have been chemically analyzed for technetium-99, and the respective fuel burnups have been calculated. A fission-yield value of 5.8% was used. The burnups of two Mark-IA elements, BF02 and BF03, represent the highest burnup this element design has achieved. The Mark-II elements, 207 and 213, were removed from irradiation Subassembly XO53 for interim examination. The results of the burnup analyses are as follows:

| <u>Element Type</u> | <u>Element Number</u> | <u>Irradiation-subassembly Number</u> | <u>Measured Max Burnup (at. %)</u> | <u>Calculated Max Burnup (at. %)</u> |
|---------------------|-----------------------|---------------------------------------|------------------------------------|--------------------------------------|
| Mark IA             | BF02                  | XO66                                  | 3.38                               | 3.7                                  |
| Mark IA             | BF03                  | XO66                                  | 3.63                               | 3.7                                  |
| Mark IA             | BF08                  | XO52                                  | 2.54                               | 2.7                                  |
| Mark II             | 207                   | XO53                                  | 3.00                               | 3.5                                  |
| Mark II             | 213                   | XO53                                  | 3.61                               | 4.2                                  |

The measured burnup values are consistently lower than the calculated values. For the Mark-IA elements, the measured values differ by less than 10% from the calculated ones, but the Mark-II elements show nearly a 20% difference.

(ii) Swelling of Stainless Steel in Mark-II Capsule Material  
(R. V. Strain)

Density determinations (see Fig. I.D.13) of 1-in. samples of stainless steel capsule material surrounding Mark-II Element 262 in Subassembly XO53 (burnup  $\sim 3.6$  at. %) have been made to determine the amount of swelling of the steel. The capsule material had been irradiated to a maximum total fluence of  $\sim 3.1 \times 10^{22}$  total nvt. In Fig. I.D.14 a comparison is made of the percent volume change based on the density determinations with the percent volume change based on diameter measurements made previously. (The volume changes based on diameter measurements were obtained by multiplying the diameter changes by three.) In both cases, the volume changes are relative rather than absolute, because the original diameters and densities are based on readings from the upper blanket region of the capsule.

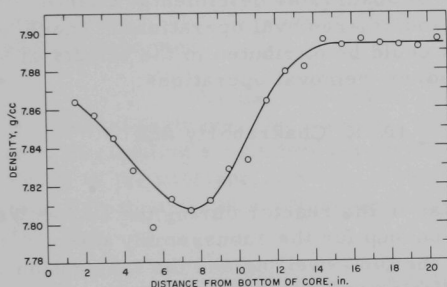


Fig. I.D.13. Density Profile of Samples from Capsule 262, Subassembly XO53 (total neutron fluence  $\sim 3.1 \times 10^{22}$  n/cm<sup>2</sup>)

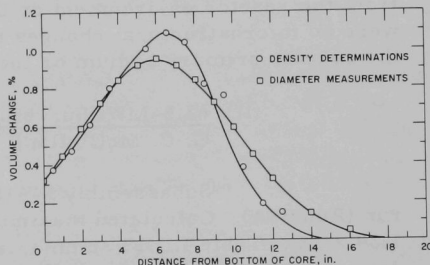


Fig. I.D.14. Volume Change of Capsule 262 from Subassembly XO53 (total neutron fluence  $\sim 3.1 \times 10^{22}$  n/cm<sup>3</sup>)

The relatively good agreement between the volume changes based on diameter and on density indicates that the swelling of stainless steel is isotropic and that diameter measurements are a reliable means of determining cladding swelling.

b. Fuel and Cladding Surveillance

Last Reported: ANL-7661, pp. 67-70 (Jan 1970).

(i) 70%-enriched Experiments (R. V. Strain)

Cladding samples from 70%-enriched Element 24, Subassembly C-2193S, were examined for evidence of grain-boundary corrosion or cracking as part of the fuel and cladding surveillance program. This subassembly had been irradiated to a maximum burnup of 1.5 at. % ( $\sim 1.4 \times 10^{22}$  total nvt) in two steps. The element was subjected to two sodium-removal operations, one during the interim inspection at 1.2 at. % burnup

and one after irradiation to 1.5 at. % burnup. The fuel in the subassembly was 70%-enriched uranium-fission alloy, which was used to simulate 62.5-MWt operating conditions for the fuel elements at a 50-MWt power level. The maximum cladding temperature of the element was about 1040°F as opposed to 950°F for a 52%-enriched element in the same position.

The samples of cladding were examined in the as-polished condition after etching in a ferric chloride solution (0.1 g of  $\text{FeCl}_3$  in 60 cc of lactic acid, 30 cc of  $\text{HCl}$ , and 10 cc of  $\text{HNO}_3$ ) and after electroetching in 10% oxalic acid. The examination in the as-polished condition following etching in ferric chloride solution revealed no evidence of grain-boundary corrosion or cracking. The examination following the oxalic acid etch revealed a sensitized microstructure in all the samples except the one from near the bottom of the element. Although the sensitized structure was more extensive than observed for normal, 52%-enriched elements operated at a reactor power of 50 MWt, there were no observable detrimental effects from the reactor environment or the sodium-removal operations. There were no microstructural changes that could be attributed to the effects of the reactor primary sodium or the sodium-removal operations.

(ii) 62.5-MWt Surveillance (A. K. Chakraborty and G. C. McClellan)

Subassembly S-618 was in the reactor during the 62.5-MWt run (Run 38A). Calculated maximum burnup for the subassembly was 1.39 at. %. Table I.D.13 summarizes the fuel-swelling and the fabrication data for this subassembly. Postirradiation examination showed that two of the three cold-line batches represented in S-618 exhibited fuel swelling similar to that shown by past data for Mark-IA fuel operated at 50 MWt. The third batch exhibited fuel swelling slightly higher than the other two batches, but the swelling is still within the scatter in swelling values obtained with low-swelling fuel operated at 50 MWt.

TABLE I.D.13. Summary of Fabrication and Irradiation Data for Subassembly S-618

(Burnup: 1.39 at. % max; 1.26 at. % avg)

| Injection-casting Batch No. | Silicon Content of Fuel (ppm) | Number of Elements | Range of Element Burnup (at. %) | Total Volume Fuel Swelling ( $\Delta V/V$ , %) |            |
|-----------------------------|-------------------------------|--------------------|---------------------------------|--|------------|
|                             |                               |                    |                                 | Average  | Range      |
| 14IH                        | 377                           | 2                  | 1.34-1.37                       | 5.54   | 5.0-6.1    |
| 115IH                       | 416                           | 21                 | 1.29-1.39                       | 6.40   | 5.03-7.32  |
| 121IH                       | 266                           | 8                  | 1.29-1.38                       | 9.40   | 9.40-10.38 |
| For subassembly             |                               |                    |                                 | 7.12   |            |

## 9. Operation with Failed Fuel (R. R. Smith)

### a. TREAT Simulations of EBR-II Fuel Failures

Last Reported: ANL-7640, pp. 73-74 (Nov 1969).

- (i) Postirradiation Examination of Element EBR-MF-2, a Partially Bonded EBR-II Driver Element Irradiated in TREAT (D. L. Mitchell, R. V. Strain, and D. M. Cheney)

A flat-topped transient in TREAT, as discussed in ANL-7640 and in the Progress Reports for Sept 1969, ANL-7618, pp. 65-69, and for August 1969, ANL-7606, p. 63, was carried out with test element EBR-MF-2 in an attempt to evaluate the effects of power operation on an element containing substantial voids in the sodium. The element was bonded in such a way that the lower portion of the fuel was completely bonded, the midportion was partially bonded, and the upper portion (above midsection) was completely unbonded.

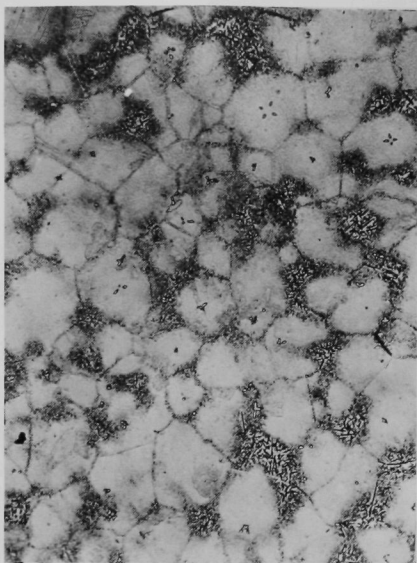
Visual examination of the element after irradiation revealed no unusual features, and diameter measurements of the element indicated that no cladding strain had occurred. Eddy-current bond testing and radiography of the element, however, showed that the element had shortened more than 1/2 in. and had slumped against the jacket above the midlength of the fuel pin.

Five samples from the element were examined metallographically to observe the condition of the fuel and cladding in the bonded, partially bonded, and unbonded regions of the element. Microhardness measurements also were made of each of the samples; Table I.D.14 gives the results of these measurements. Figure I.D.15 shows micrographs of typical areas of the fuel from the three regions of the element. The fuel in the bonded region of the element had an as-cast structure, and the microhardness indicated that it contained alpha-phase uranium in the alloy.

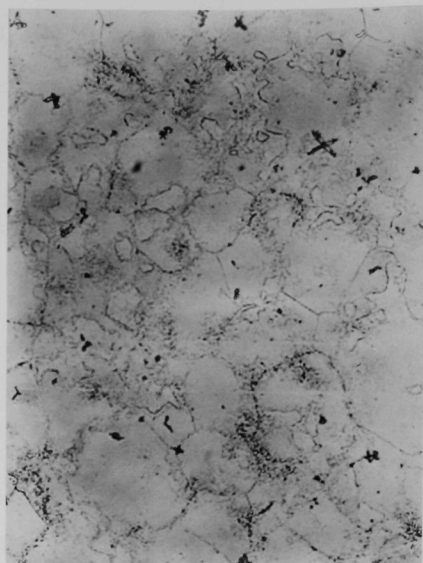
TABLE I.D.14. Microhardness of  
Samples from EBR-MF-2

| Sample | Distance from<br>Bottom (in.) | DPH Microhardness <sup>a</sup><br>(500-g load) |
|--------|-------------------------------|--|
| 192B1  | 2½                            | 463  |
| 192B2  | 5                             | 233  |
| 192B3  | 6½                            | 241  |
| 192B4  | 9                             | 244  |
| 192B5  | Top                           | 238  |

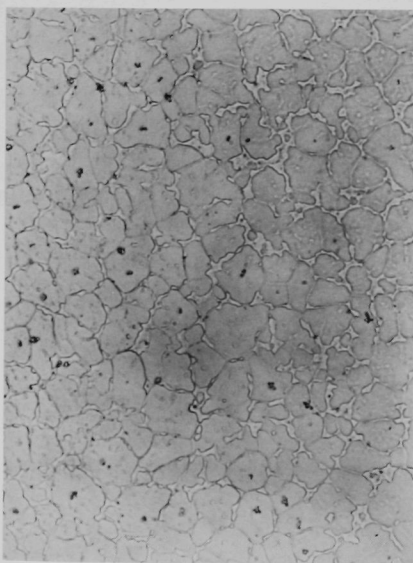
<sup>a</sup>Average of five measurements.



Microstructure of Fuel Pin in  
Fully Bonded Region of Element



Microstructure of Fuel Pin in Partially  
Bonded Region of Element



Microstructure of Fuel Pin in  
Unbonded Region of Element

Fig. I.D.15

Photomicrographs of Fuel from Element EBR-MF-2 after Transient Irradiation in TREAT. Samples were etched in a solution of 0.5 g of EDTA, 5 ml of  $\text{HNO}_3$ , 10 ml of 30%  $\text{H}_2\text{O}_2$ , and 100 ml of  $\text{H}_2\text{O}$ . Mag. 500X.

The fuel in the partially bonded region appears to have reached a temperature sufficient to cause the fission-alloy elements near the grain boundaries to go into solid solution in the matrix and the uranium to transform to the gamma phase, as indicated by the low hardness for this sample (see Table I.D.14). The microstructure of the fuel in the unbonded region shows that melting had begun to occur at the grain boundaries, thus indicating that the temperature of the fuel nearly reached 1000°C in that region. Two areas of interaction between the fuel and the cladding were found in the samples from near the top of the fuel pin. The deepest penetration observed of the interaction of the cladding into the fuel was about 0.004 in. The thickness of the cladding wall appeared to be reduced by about 0.001 in. in this area.

The results of this examination show that, although very high fuel temperatures caused slumping of the fuel above the midlength of the pin, very little interaction occurred between the fuel and the cladding. The fuel pin in the bonded region exhibited no apparent change during the test, and the partial bond apparently provided sufficient heat transfer to prevent slumping of the fuel.

#### 10. Physics Mock-up Studies

Last Reported: ANL-7661, pp. 74-76 (Jan 1970).

##### a. EBR-II Critical-assembly Studies (D. Meneghetti)

Experimental results for ZPR-3 Assembly 60, the first of the series of the EBR-II critical assemblies, are reported in Sect. I.A.4.

# E. EBR-II--Fuel Fabrication

## 1. Cold Line Operations (D. L. Mitchell)

Last Reported: ANL-7661, p. 76 (Jan 1970).

The cold-line equipment for producing Mark-IA fuel elements has been placed on a standby basis.

Table I.E.1 summarizes the production activities for January 16 through February 15, 1970, and for the current year to date.

TABLE I.E.1. Production Summary for Cold Line  
(All fuel-element production equipment is on standby status)

|   | 1/16/70<br>through<br>2/15/70 | Totals for<br>CY 1970 |
|---|-------------------------------|-----------------------|
|   | Mark IA                       | Mark IA               |
| Subassemblies Fabricated  |                               |                       |
| With cold-line elements   | 5                             | 12                    |
| With vendor elements  | 0                             | 0                     |
| Preirradiation Treatment of Vendor Fuel                               |                               |                       |
| Impact bonding of unbonded elements (11,853 <sup>a</sup> )            |                               |                       |
| Impact bonded, inspected, and accepted                                | 2230                          | 4209                  |
| Impact bonded, inspected, and rejected                                | 91                            | 281                   |
| Total Elements Available for Subassembly<br>Fabrication as of 2/15/70 |                               |                       |
| Cold-line fuel: Mark IA   |                               | 392                   |
| Mark II   |                               | 234                   |
| Vendor fuel (Mark IA)   |                               | 22,645 <sup>b</sup>   |

<sup>a</sup>This is the total number of unbonded vendor Mark-IA fuel elements scheduled for impact bonding by ANL. All unbonded elements expected have been received at ANL. Ten of them have been set aside as historical samples.

<sup>b</sup>Accepted by FCF verification inspection but not yet approved for general use in the reactor. This figure does not include vendor elements that were impact bonded by ANL.

Five Mark-IA subassemblies containing fuel elements made in the cold line were fabricated in the cold line during the month.

Of the 2321 unbonded vendor elements that were impact bonded and inspected during the month, 2230 were accepted. Void size was the primary cause for rejection. Data relating to the receipt, impact bonding, and acceptance of these elements are included in Table I.E.1.



The current number (as of February 15) of vendor-fabricated elements available after verification inspection is 22,645. This figure does not include vendor elements impact bonded by ANL.

The first of preliminary tests of the equipment for the heat-treatment reclamation of vendor-fabricated fuel were completed, using depleted-uranium Mark-I elements. For these tests, the treatment consisted of heating the elements at 660°C for 1/2 hr, air quenching (at 20-cfm flow) to room temperature, heating again at 500°C for 1/2 hr, and then air quenching (at 20-cfm flow) again to room temperature. Eddy-current traces of the sodium bond before heat treatment, after the treatment at 660°C, and after the two cycles of heat treatment are being compared and evaluated.

#### F. EBR-II--Operations

##### 1. Reactor Plant (G. E. Deegan)

Last Reported: ANL-7661, pp. 76-78 (Jan 1970).

From January 21 through February 20 the reactor was operated for 1334 MWd in Runs 39C, 40A, and 40B. The cumulative total of EBR-II operation is 32,361 MWd.

Before the start of Run 39C, the lower-leaky-weld-test subassembly was removed from the core. During that run, the  $^{133}\text{Xe}$  and  $^{135}\text{Xe}$  cover-gas activities returned to normal equilibrium values. The run was ended on January 28 after a cumulated 1371 MWd in all parts of Run 39.

At the start of Run 40A, rod-drop experiments were conducted at 500 kW and 50 MWt. After nine days of this run, the reactor scrambled because of an indicated high rate of change of primary flow; there was no actual flow change. The plug-in components in the rate-of-change amplifier were replaced. During this shutdown, the lower-leaky-weld-test subassembly was returned to the core, in the Row-1 position. Under the designation of Run 40B, operation at 50 MWt was resumed, and cover-gas activities increased, as predicted, by a factor of about three.

Fuel handling during the period consisted mainly of the loading changes for Run 40A. In addition to the experimental subassemblies reported under Sect. I.D.5.a, the following special subassemblies were involved. Two vendor-fuel surveillance subassemblies that had been reconstituted from previously irradiated subassemblies were installed in the grid. The subassemblies removed included the 70%-enriched subassembly, two controlled-flow subassemblies, two vendor-fuel surveillance subassemblies, a recycled fuel-surveillance subassembly, and an inner-blanket depleted-uranium surveillance subassembly.

The loading change for Run 40B consisted only of the installation of the lower-leaky-weld-test subassembly in place of a standard driver-fuel subassembly.

## 2. Fuel Cycle Facility (M. J. Feldman)

### a. Surveillance (M. J. Feldman, J. P. Bacca, and E. R. Ebersole)

Last Reported: ANL-7661, pp. 79-81 (Jan 1970).

#### (i) Postirradiation Analysis of EBR-II Fuel (J. P. Bacca)

##### (a) Surveillance of Vendor-fabricated Fuel (A. K. Chakraborty and G. C. McClellan)

##### (1) Fuel-characterization Studies

(A) Subassembly C-2211S. Samples from fuel element 24 from irradiated driver Subassembly C-2211S (0.39 at. % maximum burnup) were metallographically examined. The element had been fabricated by the vendor and heat treated by ANL. The examinations were made to see if there was any evidence of fuel-cladding interactions or of cladding degradation which could be attributed to the ANL preirradiation "remedial" heat treatment that was given to the vendor-fabricated elements in this subassembly. The elements of the subassembly had been heat treated at 660°C for 1½ hr, air quenched to room temperature, reheated to 500°C in the bonders, and held for 2 hr while being subjected to 500 impacts. The purpose of the heat treatment was to remove a texture (preferred orientation) in the vendor-fabricated fuel elements that had caused dimensional instability (axial shortening) during irradiation.

No evidence of fuel-cladding interaction was found; the normal 0.006-in.-thick annulus between the fuel and cladding had been retained over the full length of the pin after irradiation to this level of burnup. The samples of cladding (Type 304L stainless steel) from this element exhibited sensitization (carbide precipitation at the grain boundaries) over the entire length of the element. No grain-boundary corrosion or cracking, however, was observed in any of the samples. The sensitization near the bottom of the element appears to have resulted from the heat treatment, because sensitization has not been observed previously in this region with irradiated elements that had been produced by normal ANL procedures. This sensitization at the bottom of the element is not considered detrimental. Regions of driver-fuel cladding exposed to high temperature and flux normally become sensitized during irradiation. Such sensitization has caused no obvious adverse effects.

(b) Postirradiation Surveillance (A. K. Chakraborty and G. C. McClellan)

Table I.F.1 summarizes the surveillance performed on subassemblies received from the reactor and dismantled in the FCF air cell prior to carrying out the indicated postirradiation examination. (Results of the examinations are reported in Sect. I.D.8.)

TABLE I.F.1. Postirradiation Surveillance Performed

| Subassembly No.    | Program                  | Burnup (at. % max or nvt) | Surveillance Performed   |
|--------------------|--------------------------|---------------------------|--|
| C-2173             | Extended burnup          | 1.73                      | Fuel swelling; cladding straining  |
| C-2176             | Extended burnup          | 1.71                      | Fuel swelling; cladding straining  |
| C-2193S            | 70%-enriched fuel        | 1.5                       | Metallographic examination of cladding for irradiation-induced changes in microstructure |
| XO53 (Capsule 262) | Stainless steel swelling | $\sim 3.1 \times 10^{22}$ | Density determinations on cladding   |

b. Fuel Handling and Transfer (N. R. Grant, W. L. Sales, and K. DeCoria)

Last Reported: ANL-7661, p. 81 (Jan 1970).

Table I.F.2 summarizes the fuel-handling operations performed.

c. Experimental Support (J. P. Bacca, N. R. Grant, V. G. Eschen, R. V. Strain, J. W. Rizzie, and C. L. Meyers)

Last Reported: ANL-7661, p. 82 (Jan 1970).

Subassembly XO75, a Mark-A19 irradiation subassembly, was assembled in the air cell with 18 UNC mixed-carbide capsules from previously irradiated Subassembly XO33 (calculated maximum burnup of 6 at. %) and one dummy element.

Subassembly XO65B, a Mark-B37 irradiation subassembly, was sent to the reactor after reassembly in the air cell. It contains 21 helium-pressurized structural elements previously irradiated in Subassembly XO65A

to a calculated total fluence of  $0.4 \times 10^{22}$  nvt, 5 new capsules containing temperature monitors, and 11 previously irradiated dummy elements.

TABLE I.F.2. Summary of FCF Fuel Handling

|  | 1/16/70<br>through<br>2/15/70 | Totals for<br>CY 1970    |
|--|-------------------------------|--------------------------|
| <u>Subassembly Handling</u>  |                               |                          |
| Subassemblies received from reactor  |                               |                          |
| Driver fuel (all types)  | 4                             | 10                       |
| Experimental   | 0                             | 0                        |
| Other (blanket)  | 1                             | 1                        |
| Subassemblies dismantled for surveillance,<br>examination, or shipment to experimenter |                               |                          |
| Driver fuel  | 1                             | 3                        |
| Experimental   | 0                             | 0                        |
| Other (blanket)  | 1                             | 1                        |
| Driver-fuel elements to surveillance   | 31                            | 92                       |
| Number from subassemblies  | 1                             | 3                        |
| Subassemblies transferred to reactor   |                               |                          |
| Driver fuel  |                               |                          |
| From air cell  | 2                             | 2                        |
| From cold line <sup>a</sup>  | 10                            | 10                       |
| Experimental   | 3                             | 4                        |
| <u>Fuel-alloy and Waste Shipments<sup>b</sup></u>                                      |                               |                          |
| Cans to burial ground  | 0                             | 0                        |
| Skull oxide and glass scrap to ICPP  | 0                             | 0                        |
| Recoverable fuel alloy to ICPP   |                               |                          |
| Fuel elements  | 1 (17.47 kg<br>of alloy)      | 4 (69.75 kg<br>of alloy) |
| Subassemblies  | 3 (17.58 kg<br>of alloy)      | 7 (38.13 kg<br>of alloy) |
| Nonspecification material  | 0                             | 0                        |

<sup>a</sup>Cold-line subassemblies, following fabrication and final tests, are transferred either directly to the reactor or to the special-materials vaults for interim storage until needed for use in the reactor.

<sup>b</sup>Figure outside parentheses is number of shipments made. Figure inside parentheses is weight of alloy shipped.

Encapsulated Mark-II fuel elements previously irradiated to an accumulated maximum burnup of 4.3 at. % in Subassemblies XO29 and XO53 were loaded into a new subassembly (XO71) in the air cell. Also loaded into the subassembly were nine new capsules containing Mark-II fuel elements fabricated in the FCF cold line. This is a Mark-B37 irradiation subassembly.

A Mark-B61 irradiation subassembly (XO68) was assembled with 61 new encapsulated Mark-IA driver elements.

d. Reactor Support (N. R. Grant and V. G. Eschen)

Last Reported: ANL-7655, p. 81 (Dec 1969).

Nine new control-rod thimbles and two new safety-rod thimbles were fabricated. After being tested and dimensionally inspected, they all were found acceptable for reactor use.

## PUBLICATIONS

### Leakrate Testing of the EBR-II Reactor Building

H. W. Buschman

ANL/EBR-008\* (October 1969)

### Design Parameters and Performance Characteristics of a Miniature Pressure-transducer System Using a Fluid-filled Bellows Sensor

John R. Folkrod

ANL-7574 (October 1969)

### Transition Kinetics during Linear to Parabolic Oxidation of Chromium

R. E. Grace\*\* and T. F. Kassner

Acta Met. 18, 247-251 (February 1970)

### Signal Transmission Line with Low Attenuation and Wide Frequency Passband

K. G. Porges, W. C. Corwin, L. P. Burkell, and E. Lewandowski

Rev. Sci. Instr. 41, 138-139 (January 1970) Note

### Reduction of Processing Losses in On-line or Off-line Acquisition of Random Counts at High Rates

K. G. Porges, C. J. Rush, and G. E. Caya

Nucl. Instr. Methods 78(1), 115-119 (1970)

### Mechanical Improvements of the EBR-II Fuel Unloading Machine

J. B. Waldo

ANL-7585 (November 1969)

### The Eddy-current Flowmeter: An Analysis Giving Performance Characteristics and Preferred Operating Conditions

D. E. Wiegand

ANL-7554 (August 1969)

---

\*One of a series of "blueback" topical reports prepared by the EBR-II Project.

\*\*Purdue University.

## II. OTHER FAST REACTORS--OTHER FAST BREEDER REACTORS--FUEL DEVELOPMENT

### A. Irradiation Effects, Mechanical Properties, and Fabrication

#### 1. Swelling in the Dimple Region of Subassembly XA08 (S. D. Harkness)

Not previously reported.

The dimples that serve as the points of contact between subassemblies are being studied to determine whether they suffer either more or less swelling than adjacent areas. Swelling in the region of the dimple might be expected to be different for at least two reasons:

- (1) The dimple is under a compressive stress during irradiation.
- (2) The dimple area is more cold worked because of the forming operation.

The source of material for the present study was the hexagonal guide thimble of Subassembly XA08, which was irradiated in EBR-II in position 4F2 for a total of 19,280 MWd. The peak midplane fluence for this exposure has been estimated as  $8.5 \times 10^{22}$  n/cm<sup>2</sup>. A 3-in. section that contains the dimple was cut from two flats of the hexagonal can. The dimples are located about 1.5 in. from the reactor midplane. To date both micrometer and immersion-density profiles of the pieces have been completed. Transmission electron microscopy is planned for the near future.

The general result of the micrometer trace was that the face of the dimple had been forced almost flat to the wall of the hexagonal can, with a resultant depressed area around the edge of the dimple. The distance between the top of the dimple and the plate was only 0.002 in., but in the unirradiated sample this distance was about 0.017 in. Evidence that the subassemblies were pushing against each other with considerable force was indicated by the presence of axial gouges along the hexagonal can, which were formed during extraction of the subassembly from the reactor.

The density measurements for the two samples showed a small but significant reduction in swelling in the region of the dimple. To obtain these measurements, the 3-in. section was cut into six 1/2-in. pieces. Each piece was electropolished, placed in a water bath, and its density measured. The density results are the average of three successive measurements of a particular sample. The precision within any particular series is about 4 parts in 10,000. To check the accuracy of the results, density measurements were repeated by a different operator on a different day. These results indicated that an uncompensated constant error occurs in the measurement,

which could stem from changes in bath temperature or the level of water within the bath. The fact that the shape of the density curve was reproduced is considered significant. Figure II.A.1 is presented to emphasize that the presence of the dimple reduced the swelling. Whether this reduction in swelling is due to the cold work created during the forming operation or the application of stress

during irradiation cannot be stated at this time. Transmission electron microscopy should help to distinguish between these possibilities.

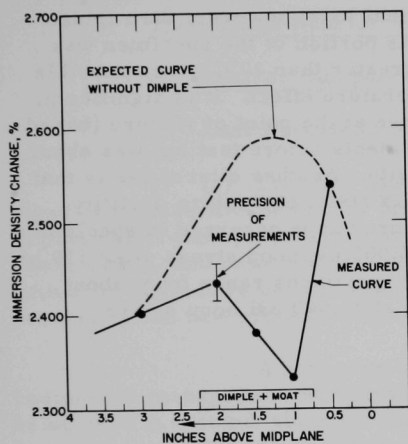


Fig. II.A.1. A Comparison of Expected and Measured Density Changes in the Dimple Region of a Guide Thimble Irradiated in EBR-II

liminary data indicate an apparent steady-state creep rate of about  $2-3 \times 10^{-5} \text{ hr}^{-1}$ . This test will be terminated at the first signs of tertiary creep, or at about 450 hr, whichever occurs first. More detailed information regarding the creep test will be presented when the experimental data are analyzed.

### 3. Surface Defects as Failure Sites in Type 304 Seamless Stainless Steel Fuel-clad Tubing (F. L. Yaggee)

Last Reported: ANL-7661, p. 86 (Jan 1970).

Biaxial creep tests have been initiated on artificially defected, thin-wall, Type 304 stainless steel tubes at  $650^{\circ}\text{C}$  and calculated nominal hoop stresses of 7500, 10,000, 15,000, and 20,000 psi. Twenty-four specimens divided into four groups of six specimens each will be tested. Each group is being creep tested at a common temperature and one of the four nominal hoop stresses. Each group contains specimens with identical artificial defects both with regard to location and to orientations with respect to the longitudinal tube axis. The purpose of the tests is to

### 2. Mechanical Properties of Cladding Materials (F. L. Yaggee)

Last Reported: ANL-7661, p. 86 (Jan 1970).

The creep apparatus previously mentioned in ANL-7661 has been assembled and calibrated. The first creep test is in progress at  $550^{\circ}\text{C}$  and 25,000 psi stress, and is being conducted in the absence of cyclotron radiation. The 0.007-in.-thick, Type 304 stainless steel specimen (HT 890810) is identical to specimens that will be used in the cyclotron experiments. After 330 hr the pre-



determine whether test temperature and applied stress can influence the effect of artificial defects on rupture ductility.

After 17.2 hr, a rupture occurred in one specimen in the group of six specimens stressed at 20,000 psi (spec. 6AD4I) at a diametral strain of about 17%. This specimen had an artificial defect located on the bore at midlength, oriented  $45^\circ$  to the longitudinal axis; however, the rupture occurred away from the defect. Since this portion of the specimen was hotter (estimated temperature gradient greater than  $10^\circ\text{C}$ ), it is possible that the failure at this location is a temperature effect. It is significant, however, that the cross-sectional wall area at the point of rupture (based on inside- and outside-diameter measurements before testing) was about 1.8% smaller than the area at the defect site. Another alternative is that the  $45^\circ$  orientation of the defect reduces its effect on rupture ductility ( $\Delta D/D_0$  at defect site was 11.6%). No failures have occurred in specimens being creep tested at 7500, 10,000, and 15,000 psi hoop stress after 110 hr of testing. Specimen strains in the latter specimens range from about 0.35% at 7500 psi hoop stress to about 5% at 15,000 psi hoop stress.

### III. GENERAL REACTOR TECHNOLOGY

#### A. Applied and Reactor Physics Development

##### 1. Theoretical Reactor Physics--Research and Development

###### a. Theoretical Reactor Physics

###### (i) Reactor Computation and Code Development (B. J. Toppel)

Last Reported: ANL-7661, pp. 88-92 (Jan 1970).

(a) The ARC System. The ARC system production cataloged procedure ARCSP004 for burnup has been revised to simplify its use. In particular, the symbolic parameters related to composition cross sections, fluxes, and power-normalized region fluxes for the second through fifth time steps have been eliminated. An internal-user memorandum describing the new procedure has been distributed.

A nonassembler language version of the POINTR subroutine for management of dynamic data storage has been prepared and is being used in a stand-alone version of the MC<sup>2</sup> code. This all-Fortran version of POINTR will facilitate code exchange with non-IBM/360 users.

(ii) MC<sup>2</sup> Capability in the ARC System. The four modules CSI001, CSC001, CSC002 and CSC003 which represent the MC<sup>2</sup> capability in the ARC system that have been variably dimensioned (see Table III.A.1, p. 90, ANL-7661) are being incorporated into a stand-alone overlaid code package, being developed for the de facto Computer Code Coordination Committee. The committee wants the MC<sup>2</sup> code capability to execute in 45K of 64-bit words and produce the interface MULTIGRP which will contain the microscopic group cross sections. The limitation of 45K word size will severely limit the type of problem that can be run. The MC<sup>2</sup> code in the stand-alone package will require 25K words for code and fixed-dimensioned quantities, and this leaves 20K words for the container array plus the buffer areas. Problems of interest to code users will require a container array of from 40-60K words.

The ARC modules SNIFF\* and P~~Q~~INTER\*\* are being modified so that they may be integrated into this stand-alone MC<sup>2</sup> code package.

---

\*Just, L. C., and Sparck, S. D., The ARC System, Applied Mathematics Division ANL Technical Memorandum No. 157 (May 1, 1968).

\*\*Kennedy, A. S., A Dynamic Storage Allocation Program, Applied Mathematics Division ANL Technical Memorandum No. 98 (February 28, 1967). Kennedy, A. S., Corrections to P~~Q~~INTER for LCS, Applied Mathematics Division, ANL Technical Memorandum (January 28, 1969). Henryson, H. and Toppel, B. J., Modifications to P~~Q~~INTER--A Dynamic Storage Allocation Program Utilizing Bulk Memory, October 6, 1969 (Internal Memorandum).

Both of these modules taken out of the ARC environment and modified in this way will lose some of their flexibility and usefulness.

(iii) Fuel-cycle Calculations for Fast Reactors in ARC  
(B. J. Toppel and L. J. Hoover)

The fuel-cycle package has been christened REBUS, an acronym for REactor BURNup System. A catalog procedure for STP004, a nonmnemonic name for REBUS, has been written, debugged, and is now available to users. With the exception of the real-time accounting, REBUS has been debugged and is ready for user testing. A report with a thorough description of the capability, the method, and the code is being prepared for release.

Representative running times on the System 360 Model 75 for REBUS are given in Table III.A.1. By means of REBUS, the equilibrium conditions for two typical 1000-MWe, oxidized-fueled reactors were computed in 2-dimensional geometry. One of these reactors has a higher core-to-blanket leakage fraction than the other. The burn time was divided into two subintervals; fluxes were computed, therefore, at three time nodes. The burn time was adjusted to achieve a core-average burnup of 100,000 MWd/T at discharge. Feed enrichment was varied to obtain a critical system at the end of cycle. Control densities were fixed at cycle-averaged values. DIF2D was used for the neutronics solution.

TABLE III.A.1. Representative Running Times for REBUS

| Reactor             | Mesh Points<br>r-z | Groups | Time (min) |      |       | DIF2D                         |
|---------------------|--------------------|--------|------------|------|-------|-------------------------------|
|                     |                    |        | CPU        | Wait | Total | Time/Outer Iteration<br>(sec) |
| Design I            |                    |        |            |      |       |                               |
| 18-in. core height; |                    |        |            |      |       |                               |
| 924 mesh points     |                    |        |            |      |       |                               |
|                     | 42 x 22            | 6      | 55         | 18   | 73    | 19                            |
|                     | 42 x 22            | 7      | 62         | 18   | 80    | 21                            |
|                     | 42 x 22            | 8      | 69         | 20   | 89    | 23                            |
|                     | 42 x 22            | 13     | 105        | 20   | 125   | 39                            |
| Design II           |                    |        |            |      |       |                               |
| 36-in. core height; |                    |        |            |      |       |                               |
| 486 mesh points     |                    |        |            |      |       |                               |
|                     | 27 x 18            | 6      | 22         | 12   | 34    | 11                            |
|                     | 27 x 18            | 7      | 22         | 12   | 34    | 12                            |
|                     | 27 x 18            | 8      | 26         | 13   | 39    | 13                            |
|                     | 27 x 18            | 13     | 36         | 14   | 50    | 17                            |

Computation times for the two designs with different numbers of neutron groups are shown in Table III.A.1. If 8 neutron groups are used, the sequence of calculations burnup → neutronics solution requires 3.5 min for the 18-in. core with 924 mesh points and 1.6 min for

the 36-in. core with 486 mesh points. These are average times over the whole equilibrium computation. Of this time, the burnup module uses less than 10%. Note that the problems were run in r-z geometry; however, the neutronics solution time was decreased by 5% using z-r geometry.

(iv) Reactor Computations. Computation of elastic-scattering transfer cross sections has been incorporated into the RABBLE code.\* The elastic-scattering cross section for neutrons being scattered from broad group I to broad group J by nuclide k is

$$\Sigma_{sk}(I \rightarrow J) = \frac{\int_{u_{J-1}}^{u_J} du \int_{u_{I-1}}^{u_I} P_k(u - u') \Sigma_{sk}(u') \phi(u') du'}{\int_{u_{I-1}}^{u_I} \phi(u') du'} \quad (1)$$

where  $P_k(u - u')$ , the probability per unit lethargy that a neutron is scattered from lethargy  $u'$  to  $u$ , is given by

$$P_k(u - u') = \begin{cases} \frac{1}{1 - \alpha} e^{-(u - u')} & \text{for } u - u' \leq \epsilon_k \\ 0 & \text{otherwise;} \end{cases} \quad (2)$$

here  $\epsilon_k$  is the maximum lethargy open per collision. In RABBLE, a broad group is divided into thousands of very narrow fine groups of equal lethargy width. Hence, Eq. (1) becomes

$$\Sigma_{sk}(I \rightarrow J) = \frac{\sum_{n=1}^{N_I} P_k(n, J) \Sigma_{sk}(u_n) \phi(u_n)}{\sum_{n=1}^{N_I} \phi(u_n)} \quad (3)$$

where  $N_I$  is the number of fine groups in broad group I and  $P_k(n, J)$  is the probability of a neutron being scattered from fine group  $n$  into broad group J in a scattering collision with nuclide  $k$ . The form of  $P_k(n, J)$  depends upon the difference in lethargy between fine group  $k$  and the

---

\*Kier, P. H., and Robba, A. A., RABBLE, A Program for Computation of Resonance Absorption in Multiregion Reactor Cells, ANL-7326 (1967).

boundaries of broad group J. It can have the following forms, where  $u_n$  is the lower lethargy of the fine group and  $\Delta u$  is its width:

I. If  $u_I > u_n + \epsilon$ ,

$$P_k(n, I) = 1. \quad (4a)$$

II. If  $u_I \leq u_n + \epsilon$ ,

$$P_k(n, I) \Delta u = \frac{1}{1 - \alpha} \int_{u_n}^{u_n + \Delta u} du' \int_{u'}^{u_I} du e^{-(u - u')} = \frac{1}{1 - \alpha} \left[ \Delta u - e^{-(u_I - u_n)} (e^{\Delta u} - 1) \right]. \quad (4b)$$

III. If  $u_J < u_n + \epsilon_k$ ,

$$P_k(n, J) \Delta u = \frac{1}{1 - \alpha} \int_{u_{J-1}}^{u_J} du \int_{u_n}^{u_n + \Delta u} du' e^{-(u - u')} = \frac{(e^{\Delta u} - 1)}{1 - \alpha} \left[ e^{-(u_{J-1} - u_n)} - e^{-(u_J - u_n)} \right]. \quad (4c)$$

IV. If  $u_{J-1} < u_n + \epsilon_k$ ,  $u_J > u_n + \epsilon_k$ ,

$$P_k(n, J) \Delta u = \frac{1}{1 - \alpha} \int_{u_n}^{u_n + \Delta u} du' \int_{u_{J-1}}^{u' + \epsilon} du e^{-(u - u')} \\ = \frac{(e^{\Delta u} - 1)}{1 - \alpha} e^{-(u_{J-1} - u_n)} - \frac{\alpha \Delta u}{1 - \alpha}. \quad (4d)$$

V. If  $u_{J-1} < u_n + \epsilon_k$ ,

$$P_k(n, J) = 0. \quad (4e)$$

## B. Reactor Fuels and Materials Development

### 1. Fuels and Claddings--Research and Development

#### a. Behavior of Reactor Materials

##### (i) Fuel Behavior

##### (a) Solid-fission-product Swelling

(A. E. Dwight and D. R. O'Boyle)

Last Reported: ANL-7640, pp. 98-99 (Nov 1969).

Previous work by Bramman et al.\* and by O'Boyle et al.\*\* has shown that the white, metallic fission-product inclusions observed in  $\text{UO}_2\text{-PuO}_2$  fuel irradiated in a fast-neutron flux have a close-packed hexagonal crystal structure, and have a wide range of solid solubility for molybdenum, ruthenium, and rhodium. An isothermal section through the Mo-Ru-Rh system at  $1140^\circ\text{C}$  established the solid solubility limits of the Mo-Rh epsilon phase, and the adjacent Mo +  $\epsilon$  and  $\epsilon$  + Rh two-phase regions.

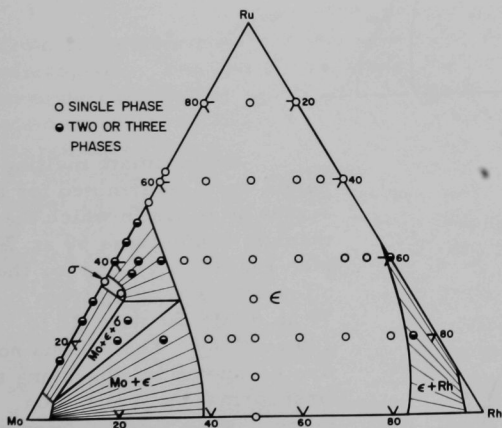


Fig. III.B.1. Mo-Ru-Rh Isotherm at  $1525^\circ\text{C}$

Since the metallic inclusions are commonly seen in the mixed-oxide fuel at temperatures above  $1140^\circ\text{C}$ , additional X-ray diffraction studies were carried out to establish the phase relations at a higher temperature. Recent work with additional alloys and at higher annealing temperatures has resulted in the  $1525^\circ\text{C}$  isothermal section (see Fig. III.B.1). The  $\epsilon$ -phase field shows an increased solid solubility for molybdenum and rhodium (compared with the  $1140^\circ\text{C}$  isothermal section), and the sigma phase<sup>†</sup> is

\* Bramman, J. I., Sharpe, R. M., Thom, D., and Yates, G., Metallic Fission-product Inclusions in Irradiated Oxide Fuels, J. Nucl. Mater. 25, 201 (1968).

\*\* O'Boyle, D. R., Brown, F. L., and Sanecki, J. E., Solid Fission Product Behavior in Uranium-Plutonium Oxide Fuel Irradiated in a Fast Neutron Flux, J. Nucl. Mater. 29, 27 (1969).

† Anderson, E., and Hume-Rothery, W., The Equilibrium Diagram of the System Molybdenum-Ruthenium, J. Less-Common Metals 2, 443 (1960).

present in the Mo-Ru binary system. A small amount of rhodium can be substituted for ruthenium in the sigma phase.

The lattice parameters of the  $\epsilon$ -phase were measured over the entire single-phase region. The lattice parameters  $a_0$  (see Fig. III.B.2) and  $c_0$  (see Fig. III.B.3) increase as the molybdenum content increases, but  $c_0$  increases more rapidly than  $a_0$ . Lattice parameters of the binary Mo-Rh  $\epsilon$ -phase were taken from Pearson's handbook of lattice spacings.\*

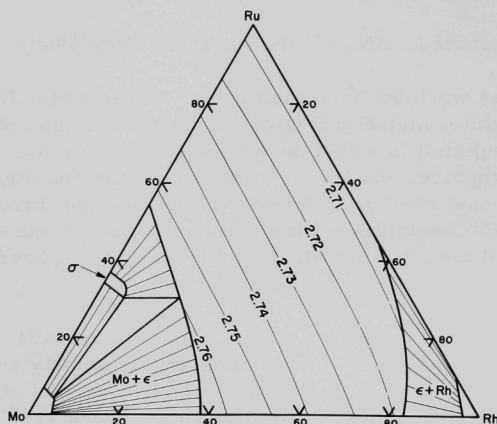


Fig. III.B.2

Lattice Parameter  $a_0$  (Å) of the Mo-Ru-Rh  $\epsilon$  Phase, Annealed at 1525°C

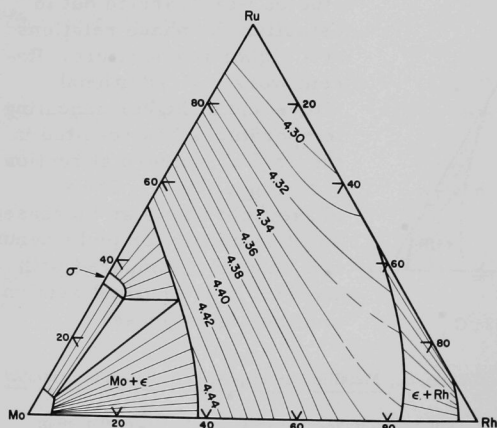


Fig. III.B.3. Lattice Parameter  $c_0$  (Å) of the Mo-Ru-Rh  $\epsilon$  Phase, Annealed at 1525°C

Approximate melting points were determined for a series of alloys in which the ruthenium content was 60 at. % (see Fig. III.B.4), and for the alloy series ranging from 50 at. % Mo-50 at. % Rh to 100 at. % Ru. The solidus point was estimated by observing the first formation of liquid on heating, when the specimen was resting on a resistance-heated tungsten strip. Temperatures were measured with an optical pyrometer and the melting experiment was carried out in an argon atmosphere. The white metallic inclusions found in irradiated  $\text{UO}_2$ -Pu $\text{O}_2$ , which are

\*Pearson, W. B., Handbook of Lattice Spacings and Structures of Metals, Pergamon Press (1967).



the Mo-Ru-Rh  $\epsilon$ -phase with some technetium and palladium in solid solution, probably have a melting point that ranges between 2000 and 2300°C.

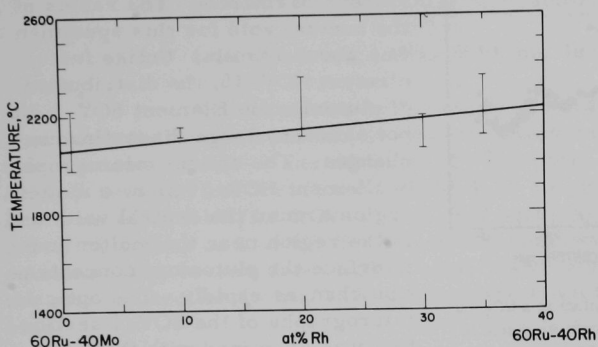


Fig. III.B.4  
Approximate Melting Temperatures of Mo-Ru-Rh Alloys with 60 at. % Ruthenium

(b) Migration of Major Fuel Constituents (R. Natesh and D. R. O'Boyle)

Last Reported: ANL-7606, pp. 95-96 (Aug 1969).

The radial redistribution of plutonium in a specimen from fuel element SOV-1 was studied by means of a shielded electron microprobe. The fuel element contained  $\text{UO}_2$ -20 wt %  $\text{PuO}_2$  (fully enriched uranium) and had an initial smear density of 80% of theoretical. The fuel element was irradiated in EBR-II to a burnup of about 5.0 at. % in two increments burnup (of 3.6 at. % at a peak linear power rating of 20.1 kW/ft in Subassembly XO11, and burnup of 1.4 at. % at an estimated peak linear power rating of 19.5 kW/ft in Subassembly XO39). Metallographic study of the fuel element indicated that the fuel operated with a molten center during the first period in the reactor, and operated in the solid state during the second period in the reactor (see Progress Report for October 1969, ANL-7632, pp. 109-110). The specimen examined in the microprobe was a transverse cross section located 1/2 in. from the bottom of the fuel element. Simultaneous measurements were made of uranium and plutonium along a radii at intervals of about 0.7 mil. The measured X-ray intensities were corrected for (1) background due to the continuous spectrum, (2) background due to scattered secondary and to fluorescent radiation, (3) beam-current drift, (4) detector dead-time losses, (5) absorption effects, (6) characteristic line fluorescence, and (7) atomic number effects, using the MAGRAM computer program.

Figure III.B.5 shows the distribution of plutonium along a radius of the specimen. In agreement with previous results (see Progress Reports for August 1969, ANL-7606, pp. 95-96; February 1968, ANL-7427, pp. 102-104; and September 1967, ANL-7382, pp. 76-77), the

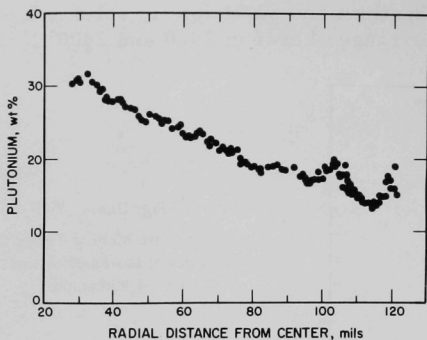


Fig. III.B.5. Distribution of Plutonium in a  $\text{UO}_2$ -20 wt %  $\text{PuO}_2$  Fuel Element Irradiated in EBR-II to a Burnup of 5.0 at. %

plutonium concentration increased at higher irradiation temperature regions of the fuel. The radius of the central void for this specimen was about 30 mils. Unlike fuel element HOV-15, the distribution of plutonium in Element SOV-1 did not show any large discontinuous changes. The optical micrographs of Element HOV-15 show a molten region around the central void, and in the region near the molten fuel interface the plutonium concentration changes rapidly. The optical micrographs of the SOV-1 section that was examined with the microprobe did not show any evidence of

molten fuel near the central void and does not show any sharp changes in the plutonium concentration.

(c) Studies of Fuel-element Modeling (R. W. Weeks and V. Z. Jankus)

Last Reported: ANL-7655, pp. 101-102 (Dec 1969).

The LIFECODE is in a prove-out stage, which involves an extensive literature review to choose the "best available" values for input data for materials properties. Required input data for restructuring rates are being derived by calibration against results from short-term fuel-element irradiations for which the power history is known. When the input-data requirements have been satisfied as well as possible, further calibration runs will be made to compare code predictions with results from actual long-term fuel-element irradiations.

A study of potential long-term fuel-element irradiations suitable for code calibration revealed that most of the resulting elements had been encapsulated. To expedite analysis of these elements, the heat-transfer portion of the LIFECODE has been modified to include encapsulated elements. In addition, a revised heat-transfer coefficient for the fuel-clad gap which is a function of the gap width, is now being used.

A plotting routine is being incorporated into LIFECODE to save time in interpreting output results.

b. Chemistry of Irradiated Fuel Materials (C. E. Crouthamel)

(i) Postirradiation Studies of Reactor Fuel and Cladding

Last Reported: ANL-7640, pp. 101-102 (Nov 1969).

Recent efforts in the electron microprobe analysis of irradiated fuels have concentrated on two mixed-oxide ( $\text{UO}_2$ -20 wt %  $\text{PuO}_2$ ) fuel elements, TVOV-1 and HOV-15. TVOV-1 was clad with vanadium-20 wt % titanium and irradiated in EBR-II to 3.6-at. % burnup at a linear heat rate of 19.6 kW/ft; HOV-15 was clad with Hastelloy and irradiated to 3.5-at. % burnup at 21.4 kW/ft. The specimens examined were both radial sections. The section from HOV-15 was taken from near the midplane of the pin; the section from TVOV-1 was taken from the lower quarter of the pin.

Examination of these specimens has shown that both uranium and plutonium redistributed in an unusual manner in the bulk fuel. The material nearest the cladding was found to be virtually free of plutonium; its general composition was a mixture of uranium oxides and oxides of the cladding components. These data are in contrast with those for SOV-6, which showed no significant deviation from the original composition ( $\text{UO}_2$ -20 wt %  $\text{PuO}_2$ ) in the region near the cladding. For TVOV-1 and HOV-15, appreciable concentrations of plutonium begin to appear in the unrestructured region of the irradiated fuel, about 0.2 mm from the cladding edge. As one moves toward the center of the pins from the unrestructured region, the plutonium concentration rises and reaches a plateau. This plateau extends through the equiaxed-grain region and the cooler half of the long columnar-grain region. At this point, the plutonium concentration again increases and reaches a maximum at the central void.

In TVOV-1, the plutonium concentration was 31 wt % in the plateau region and 39 wt % at the central void; in HOV-15, the plutonium concentration was 26 wt % in the plateau region and 37 wt % at the central void.

If one postulates that oxides of uranium are migrating in the fuel (as either  $\text{UO}_2$  or  $\text{UO}_3$  vapor species), this migration could be due to many parameters. The only known parameter that is common to the two fuels and could be expected to produce this effect is low smear density. This particular factor appears to be contributing significantly to fission-product migration in HOV-15.

The titanium-vanadium cladding of TVOV-1 is known to be an oxygen sink and is expected to have lowered the oxygen-to-metal ratio in the fuel considerably. This change may have enhanced the migration of oxygen-bearing species in the fuel and contributed to uranium migration.

Work is now in progress to calculate plutonium material balances in these fuel specimens.

c. Thermodynamics of Fuel Materials

- (i) Total Vapor Pressures and Carbon Potentials in the Ternary U-C-Pu System (P. E. Blackburn and M. Tetenbaum)

Last Reported: ANL-7640, pp. 102-103 (Nov 1969).

A program for investigating the carbon potentials and total pressures of the U-Pu-C system is in progress. Total pressure of actinide metal species as well as carbon activity are being measured by a transpiration technique. Activity measurements over a wide range of temperature and with well-defined composition are needed to establish reliable thermodynamic quantities, as well as to define phase-boundary composition. In particular, carbon activity data are important in predicting possible carbon embrittlement of cladding by carbide fuel, the chemical state of fission products, and effects of additives on the properties of fast reactor fuels.

Attempts were made to establish the congruent vaporization composition of uranium carbide by flowing an inert gas over uranium carbide at high temperature, using the transpiration technique. These data provide a method for corroborating the carbon and uranium activities measured in the U-C system at the congruent vaporizing composition. The argon carrier-gas flow rate was approximately 200 ml/min. At various intervals (after cooling to room temperature), small portions of the uranium carbide residue were removed from the transpiration apparatus for analysis. The results are summarized in Table III.B.1. It should be noted that the congruent composition was approached from both hypostoichiometric and hyperstoichiometric compositions relative to carbon. From the results given in Table III.B.1, one can conclude that the congruent composition lies near  $C/U = 1.05$ . In the temperature range 2255-2455°K, the congruent composition appears to be insensitive to temperature. For comparison, between 2200 and 2500°K, a congruently vaporizing composition of  $C/U = 1.07 \pm 0.05$  was obtained by Leitnaker and Witteman\* from Langmuir vaporization experiments; Vozzella et al.\*\* obtained  $C/U = 1.09 \pm 0.003$ , and Bowman and Krupka† obtained  $C/U = 1.065$ . It is apparent that the congruent composition derived from our studies is in reasonable agreement with those obtained by means of Langmuir vaporization. The compositions also agree with those calculated from our uranium and carbon activities and literature data for uranium and carbon pressures.

\*Leitnaker, L. M., and Witteman, M. G., *J. Chem. Phys.* **36**, 1445 (1962).

\*\*Vozzella, P. A., Miller, A. D., and DeCrescente, M. A., *J. Chem. Phys.* **49**, 876 (1968).

†Bowman, M. G., and Krupka, M. C., the Fourth Uranium Carbide Conference, TID-7676 (1963), p. 128.

TABLE III.B.1. Determinations of the Congruent Vaporization Composition for the Uranium Carbide System  
(Argon carrier gas, flow rate  $\sim 200$  ml/min)

| Temperature<br>(°K)                         | Carrier Gas<br>Volume (liters) | C/U             |
|---|--------------------------------|-----------------|
| (A) Initial Carbide Composition, C/U = 0.95 |                                |                 |
| 2355  | 26.3                           | $0.95 \pm 0.02$ |
| 2355  | 35.1                           | $1.00 \pm 0.01$ |
| 2355  | 66.3                           | 1.04            |
| 2355  | 28.0                           | $1.05 \pm 0.01$ |
| 2355  | 40.4                           | 1.05            |
| (B) Initial Carbide Composition, C/U = 1.37 |                                |                 |
| 2255  | 104                            | 1.15            |
| 2255  | 104                            | 1.09            |
| 2255  | 134                            | 1.06            |
| 2255  | 91                             | 1.04            |
| 2355  | 72                             | 1.05            |
| 2455  | 67                             | 1.06            |

The study of the vaporization behavior of the uranium-carbon system is continuing. Current emphasis has been placed on the effects of oxygen contamination in uranium carbide on the system uranium, carbon, and oxygen potentials. This is important in establishing allowable levels of oxygen impurity in carbide fuels.

In the initial experiments on the effects of oxygen contamination, argon-carbon monoxide mixtures are being used as the equilibrating gas. Exploratory runs at 1973°K with a carrier-gas mixture having a carbon monoxide partial pressure of approximately 19 Torr yielded a condensed material containing approximately 1.5 at. % oxygen and having an average composition of  $UC_{1.05}O_{0.03}$ . Two measurements of the total pressure of uranium-bearing species over this composition (carrier-gas flow rate  $\sim 180$  ml/min, plateau not established) yielded values for  $\log p(U)$  of -6.62 and -6.69, respectively. These values are considerably higher than the total pressure of uranium-bearing species over the corresponding "oxygen-free" carbide  $UC_{1.05}$ . From Storms' data,\*  $\log p(U) \cong -9.30$  at 1973°K for  $UC_{1.05}$ .

\*Storms, E. K., The Refractory Carbides, Academic Press, N.Y. (1967), Ch XI, p. 205.

We plan to measure the  $\text{CO}/\text{CO}_2$  and  $(\text{CO})^2/\text{CO}_2$  ratios in the equilibrating gas by means of gas chromatography. From these ratios, estimates of the carbon and oxygen activities can be obtained.

d. Oxide Fuel Studies

(i) Studies of Fuel Swelling (L. C. Michels and T. W. Latimer)

Last Reported: ANL-7655, p. 103 (Dec 1969).

Additional evidence for the existence of subgrain boundaries in the equiaxed to columnar-grain transition regions and in the columnar regions of SOV-6 and HOV-15 has been obtained by optical metallography. The subgrain boundaries were first found by replica electron microscopy. Etching times of up to 135 min using an etchant developed at BNWL were required to bring out the subgrain boundaries in optical metallography. The observations (see Fig. III.B.6) indicate that these subgrain

boundaries migrate sidewise as well as up the temperature gradient, and are usually decorated with gas bubbles and solid fission-product precipitates. These subboundaries could form as the result of dislocation multiplication and reorganization during swelling-induced creep.

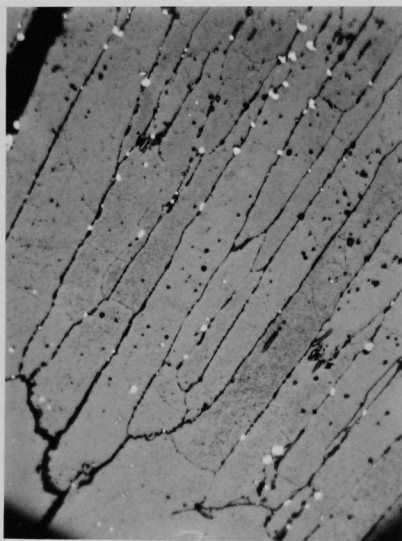


Fig. III.B.6. Area near the End of the Columnar Region in HOV-15. Fuel center is toward lower left. Mag. 150X.

There are two other possibilities for the formation of the observed subgrain boundaries. In general, growth of subgrains during solidification can be ruled out because subgrain boundaries were also observed in the structure of Element SOV-6, which did not operate in the molten condition. The second possibility is that the subgrain boundaries formed as a result of the sintering of microcracks formed during reactor cycling. The stress and temperature gradients present in the fuel could provide the driving forces necessary for the migration of the subgrain boundaries once they are formed. This situation

is further complicated by the possibility that gas bubbles and solid fission-product precipitates can either retard or enhance the subboundary migration



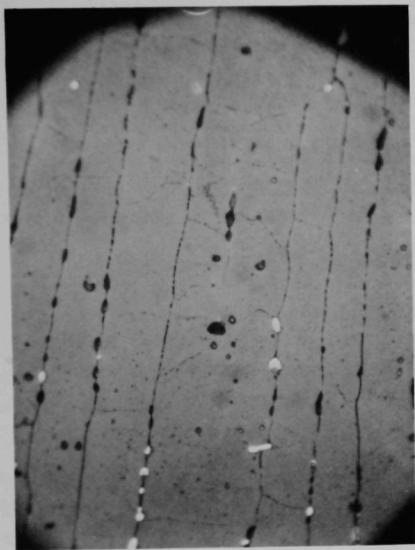


Fig. III.B.7. Area in the Columnar Region of HOV-15. Fuel center is toward the top. Mag. 300X.

depending upon local conditions, as shown in Fig. III.B.7. The sub-boundary migration can also be retarded by interaction with other boundaries (see Fig. III.B.7).

The generation of creep-induced or sintered-microcrack subgrain boundaries and their migration would be expected to be a continually recurring process throughout the lifetime of the fuel. Fission-product sweeping toward the fuel center as well as sideways into existing cracks and columnar boundaries would be one important result of the process, and would account for the numerous findings of solid fission-product ingots at the base of the central void. Another result would be the continuous regeneration of the columnar-grain structure without the necessity of the migration of lenticular voids. No lenticular voids were found in

the structure of Element HOV-15, although this fuel had restructured in the solid state in one day after an initial period of irradiation with a molten center.

An additional observation is that the columnar grain boundaries are apparently capable of sideways migration throughout the columnar region. This would also contribute to the sideways sweeping of fission products.

(ii) Fuel-element Performance (L. A. Neimark and W. F. Murphy)

(a) Irradiation of Group 0-3 Fuel Elements

Last Reported: ANL-7661, p. 101 (Jan 1970).

The eighteen mixed-oxide fuel elements of Group 0-3 are being irradiated in the EBR-II in Subassembly XO72. The subassembly was put into position 6E2 at the beginning of Run 39. During Run 39 (A, B, and C) the subassembly accumulated 1371 MWd of exposure. At the end of Run 39, the subassembly was moved to position 6B2, maintaining the same orientation with respect to the reactor core center. As of



February 12, 1970, the subassembly had acquired 517 MWd in Run 40. The total accumulated MWd is 1888, which is ~20% of the first target irradiation of 9500 MWd ( $3\frac{1}{2}$  at. % burnup).

e. Irradiation Effects in Creep of Oxide Fuels

- (i) Fission-induced Creep of Ceramic Fuels (A. A. Solomon and R. H. Gebner)

Last Reported: ANL-7487, pp. 87-88 (Aug 1968).

The in-pile creep of enriched  $\text{UO}_2$  helical springs presents a number of problems, both practical and theoretical. In order to demonstrate the feasibility of this experiment and to obtain unusual low strain-rate data, a series of thermal-creep experiments has been initiated utilizing depleted  $\text{UO}_2$  helical springs.

The creep apparatus consists of a dead-weight loading system that is completely enclosed in a vacuum furnace to avoid the problems of sealing the load train. Vacuums of  $5 \times 10^{-7}$  in. Hg have been achieved.

The furnace employs a  $7\frac{1}{4}$ -in.-long tantalum element that yields a heat zone of  $\pm 2\frac{1}{2}^\circ\text{C}$  over 2 in. Long-term control is  $\pm 1/4^\circ\text{C}$  over 24 hr. This heat zone was measured by attaching three Pt-10 Rh thermocouples to a deformed  $\text{UO}_2$  spring, as shown in Fig. III.B.8. Also shown is an undeformed  $\text{UO}_2$  spring.

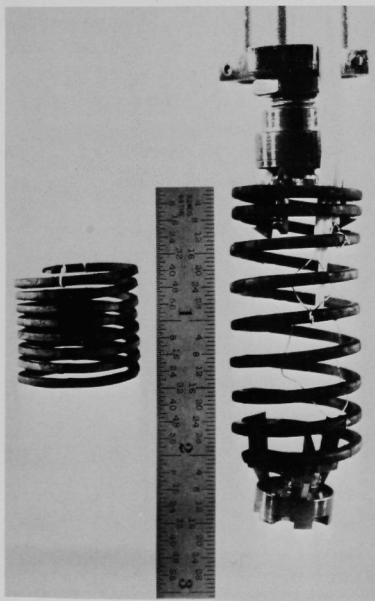


Fig. III.B.8. Deformed and Undeformed Slip-cast Helical Springs of Stoichiometric  $\text{UO}_2$

The springs shown in this figure were produced by the slip-cast technique. This method, at present, has the disadvantage that an additional plastic deformation of the sintered spring prior to creep testing is required to permit gripping. A second disadvantage of this technique is that it yields a trapezoidal cross section. Solutions are not presently available for the stress distribution during time-dependent deformation of a helical spring of trapezoidal cross section; therefore, only estimates can be made of the maximum fiber stress. A comparison of the maximum fiber stress with the results for compression of stoichiometric  $\text{UO}_2$  reveals that the

helical spring geometry yields consistent results for the strain rate within an order of magnitude. For these reasons, an extrusion technique has been developed to produce helical  $\text{UO}_2$  springs with circular cross section. These fabrication techniques will be described in a future report.

The helical spring configuration was selected because of the large magnification factors of  $\sim 3000$  mm that are possible between specimen shear strain and spring deflection. This magnification offers the possibility of studying very small strain rates of  $10^{-9} \text{ hr}^{-1}$  within reasonable times, and permits the determination of activation energies at relatively low temperatures. Because of the magnification factor, however, even after 100% deflection of the spring, only  $\sim 0.5\%$  strain is sustained by the material. All of the measurements, therefore, are probably made during primary creep of the  $\text{UO}_2$ . The experiments conducted on slip-cast springs reveals the presence of this primary creep region in  $\text{UO}_2$ .

Creep experiments with polycrystalline metals have shown that the apparent activation energy  $Q_C$  for creep may be determined by the instantaneous-temperature-change technique during both primary and steady-state creep, since the measured activation energy is independent of strain. The helical-spring geometry is particularly suitable for measuring  $Q_C$  during primary creep, since the specimen strain changes very little during a temperature change. At present, specimen temperature changes of  $\sim 20^\circ\text{C}$  can be made such that the new temperature is within  $1/2^\circ\text{C}$  of the control temperature in  $1\frac{1}{2}$  min. Measurements of  $Q_C$  from 1200 to  $1350^\circ\text{C}$  have yielded a value of  $90 \pm 5 \text{ kcal}$ . This value corresponds quite well with other published results for compression and bend tests of stoichiometric  $\text{UO}_2$ . Measurements of stoichiometry for the helical spring specimens indicate that the oxygen-to-metal ratio, before and after creep testing, is  $2.002 \pm 0.002$ .

Future experiments will be conducted to determine  $Q_C$  at lower temperatures that are more relevant to the in-pile creep program. In addition, the present capability of changing load during a creep test will be used to study the deformation dynamics at low strain rates in  $\text{UO}_2$  and, thus, help elucidate the mechanism of deformation in this regime.

## 2. Radiation Damage on Structural Materials--Research and Development

### a. In-reactor Creep Studies (J. A. Tesk, R. Carlander, and Che-Yu Li)

Last Reported: ANL-7632, pp. 112-113 (Oct 1969).

Data obtained by Walter, Walters, and Pugacz (EBR-II Project) from the second series of postirradiation measurements of the diameters of pressurized tubes in the Subassembly XO65 (Creep-1) have been analyzed.

The tubes are Type 304 stainless steel in roughly the annealed condition, under hoop stresses of 25-28 ksi, and irradiated at an average flux of  $6 \times 10^{14}$  n/cm<sup>2</sup>-sec  $E > 0.1$  MeV to a fluence of  $2 \times 10^{21}$  nvt. Analysis shows a radiation-induced average creep rate of  $2.2 \times 10^{-6}$  hr<sup>-1</sup>. This is of the same magnitude as reported by the British in their creep studies of loaded springs. It agrees with the value of  $3 \times 10^{-6}$  hr<sup>-1</sup> predicted by our computerized model of radiation-enhanced climb-controlled creep.

Based on the model, an additional creep deformation of  $\sim 3 \times 10^{-4}$  in. should occur during the next reactor cycle. This deformation and the previous deformation of  $5 \times 10^{-4}$  in. are small enough to consider that creep occurs under nearly constant stress conditions.

Future experiments are needed to obtain more accurate creep data, and to investigate the stress dependence and temperature dependence of the creep rate. The refined subassemblies necessary to continue this work are under design and construction.

### 3. Techniques of Fabrication and Testing--Research and Development

#### a. Nondestructive Testing Research and Development

##### (i) Neutron Radiography (H. Berger)

##### (a) Fast-neutron Techniques

Not previously reported.

A review of fast-neutron radiographic studies in the MeV energy range has indicated that good sources of neutrons in this energy range were available, both from machine types such as the low acceleration voltage reaction  $H^3(d,n)He^4$  and from radioactive sources. Detection methods include relatively fast direct-film methods with scintillator intensifying screens, and the gamma-insensitive detection methods that employ radioactive transfer or track-etch techniques. The transfer methods appear most useful with 14-MeV neutrons; the activation reaction  $Cu^{63}(n,2n)Cu^{62}$  provides a good method. Track-etch techniques with the alpha-sensitive material cellulose nitrate has also provided good gamma-free fast-neutron images; however, the image contrast of these track-etch results are thus far inferior to those obtained by the film detectors. For both of these gamma-insensitive detectors, total detector exposures of the order of  $10^{10}$  n/cm<sup>2</sup> are required. Conversely, the direct-film techniques have produced useful fast-neutron images for total exposures lower by approximately three orders of magnitude. An important characteristic of the high-sensitivity images is that the image contrasts are very similar to those obtained with the transfer technique and are, therefore, relatively true fast-neutron images.

Fast-neutron cross sections in the MeV energy range are not particularly attractive for radiography. Since cross sections are all low and similar to each other, radiographic discrimination between different materials becomes very difficult. Cross sections of several materials in the fast-neutron energy range are shown in Fig. III.B.9.

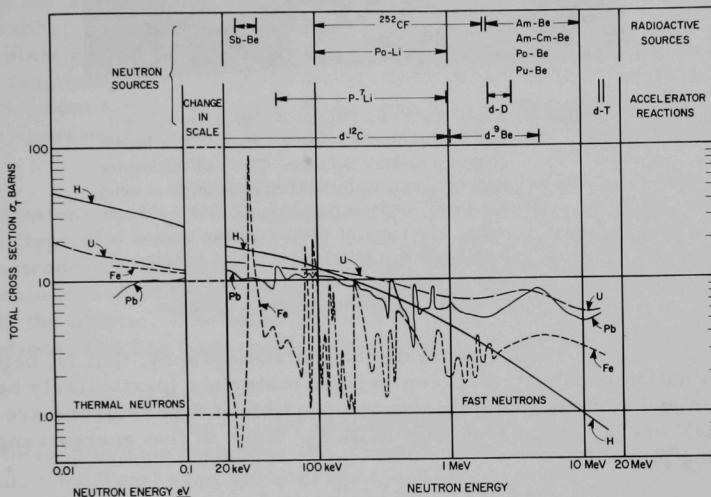


Fig. III.B.9. Total Cross Sections for Several Materials over the Fast-neutron Energy Range. Thermal-neutron cross sections (left) and the approximate spectrum range of several accelerator and radioactive fast-neutron sources (upper) are shown for information.

The advantages of fast-neutron radiography in the MeV range are:

- (1) Sources are readily available.
- (2) Large radiographic areas are available because of the point-source geometry.
- (3) Gamma-insensitive detection methods are possible. Radiography of radioactive materials is possible, for example, in a hot cell.
- (4) Knock-on protons are readily obtainable from hydrogenous radiators such as a Bakelite cassette front; therefore, proton radiography of thin objects is possible. A test-object example is shown in Fig. III.B.10. There appears to be some biological interest in this technique.



Fig. III.B.10. A Radiograph of a Stepped Wedge of Lead Taken with Protons from a Bakelite Cassette Front Irradiated with 14-MeV Neutrons. The lead thicknesses right to left are 0.25 mm (first grey image at right), 0.375 mm, 0.50 mm (about center) and 0.625 mm (left). The range of 14-MeV protons in lead is  $0.6385 \text{ g/cm}^2$ , equivalent to a lead thickness of slightly less than 0.6 mm. The radiograph shows penetration at 0.50 mm but not at 0.625 mm.

More generally useful radiography, that is, better discrimination capability between various materials (particularly between hydrogen and various metals), appears possible if fast neutrons are used in the keV energy range (see Fig. III.B.9). Work in that energy range is now being planned.

#### (b) Neutron Television System

Last Reported: ANL-7478, pp. 108-109 (July 1968).

Plans are presently under way to test a new neutron television system assembled by the Rauland Corporation. This new system makes use of an SEC vidicon camera tube. The high-resistivity target within the tube allows electronic storage of image information.\* Anticipated storage periods are in excess of 10 sec, an increase by a factor of  $\geq 300$  over rates for normal television frames.

The system, therefore, becomes attractive for use with neutron sources of lower intensity. Plans to couple this television system to a  $^{252}\text{Cf}$  thermal-neutron source are proceeding. A new moderation tank using water to bring a horizontally oriented thermal-neutron beam from the source is under construction.

---

\* Mesmer, M. H., Electronics 38, 80-90 (May 1965).

(c) Track-etch Detection Methods

Last Reported: ANL-7419, pp. 111-112 (Jan 1968).

Recently some experiments have been performed to enhance the image contrast obtained with track-etch thermal-neutron radiographs. The experiments were made with a thin ( $10\ \mu\text{m}$ ) polycarbonate plastic (Kimfoil, Kimberly-Clark Corp.) and a  $^{235}\text{U}$  foil to generate fission fragments for damage of the plastic. After etching in a 6.5 N NaOH solution (room temperature for 20 hr), the plastic was subjected to a high-voltage sparking technique in an attempt to produce a high-contrast replica.

In the spark technique, a small hole or track will exist where fission-fragment damage has occurred, and the application of a voltage (typically about 500 V) will cause a spark to puncture the hole. If one electrode in the system is aluminized Mylar, the spark will burn away the aluminum and produce a hole in the aluminum film for each fission track in the plastic. The technique was developed by Cross\* for dosimetry applications, and has been applied to autoradiographic images by Becker et al.\*\*

Our results indicated that it was possible to produce gross images by this technique (the neutron-induced fission image of the  $^{235}\text{U}$  foil, 5 by 5 cm) even for average track densities as low as a few hundred tracks per square centimeter; this result would tend to confirm the work of Becker et al. However, it was not possible to observe radiographic shadows within the radiographic area because of statistical limitations. For track densities of several thousand tracks per square centimeter or more, the uranium shadow could again be observed, but no satisfactory radiographic images were found. For the tracks of higher densities, the number of holes produced electrically isolates image areas in the aluminum replica before the image reproduction is completed. Although some control over this can be obtained by voltage settings, capacitance, spacing, etc., in order to decrease the hole size in the aluminum replica, the same limitations would be present, namely, statistical limitations at the low-exposure end of the scale and electrical continuity problems at the higher end of the scale.

---

\*Cross, W. G., Rapid Reading Techniques for Nuclear Particle Damage Tracks in Insulating Foils, Intl. Topical Conf. on Nuclear Track Registration in Insulating Solids and Applications, Clermont-Ferrand, France, May 6-9, 1969.

\*\*Becker, K., Boyett, R. H., and Johnson, D. R., Some Applications of the Track Etching Process in Radiation Protection, Intl. Topical Conf. on Nuclear Track Registration in Insulating Solids and Applications, Clermont-Ferrand, France, May 6-9, 1969.



Fortunately, some useful results continue to be obtained by photographic printing of track-etch images. A result is shown in Fig. III.B.11; the average track density for that result is of the order of millions of tracks per square centimeter.

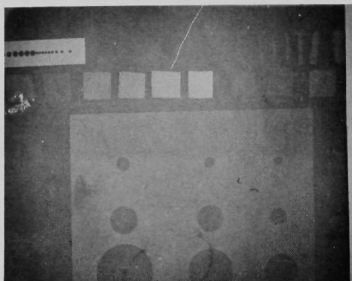


Fig. III.B.11

A Track-etch Thermal-neutron Image Taken with a  $^{235}\text{U}$  Foil and the Polycarbonate Plastic, Makrofol. Total exposure was  $10^9 \text{ n/cm}^2$ . Object imaged in the lower area is a Masonite stepped wedge; thicknesses are 2.5, 2.0, and 1.5 mm, left to right. Hole diameters are T, 2T, and 4T, where T is the step thickness. Upper objects are, for example, cadmium, plastic, and indium.

#### 4. Engineering Properties of Reactor Materials--Research and Development

##### a. High Temperature Mechanical Properties of Ceramic Fuels

##### (i) High-temperature Mechanical Properties of Fuel Oxides (J. T. A. Roberts, D. G. Pilney, and B. J. Wrona)

##### (a) Fractography

Not previously reported.

A study of the influence of grain size, strain rate, and temperature on the brittle-ductile transition in  $\text{UO}_2$  (97% TD) was made by using the 4-point bend test.\* The major findings of this work will be summarized. The curves of modulus of rupture, plastic strain, and proportional limit versus temperature (see Fig. III.B.12) are characteristic of three grain sizes (9, 15, and  $31 \mu\text{m}$ ) and three strain rates (0.092, 0.92, and 9.2/hr) tested. The transition from brittle-to-ductile behavior was marked by a sharp rise in both modulus of rupture and plastic strain. A second "transition" occurred at a higher temperature,  $T_t$ , beyond which the modulus of rupture and proportional limit fell sharply. Both the brittle-ductile transition temperature and  $T_t$  increase with an increase in strain rate. This effect was greater than was caused by a change in grain size.

\* Beals, R. J., and Canon, R. F., paper presented at Fall Mtg. of Nuc. Div. of Amer. Cer. Soc., Seattle, Washington, Oct. 15-17, 1969; 28th High Temperature Fuels Committee Mtg., May 13-15, 1969, p. 47.



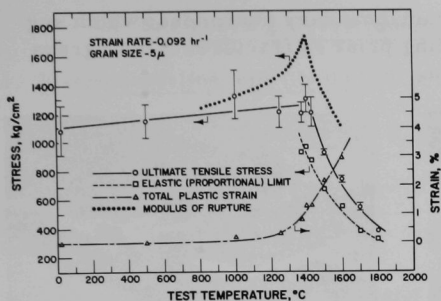


Fig. III.B.12. Temperature Dependence of the 4-point Bend Properties of  $\text{UO}_2$

each grain size and strain rate), which can be divided into three different regions of deformation behavior (see Fig. III.B.13). In region A, the material was strong but fractured without any measurable plastic deformation, i.e., in a brittle manner; in region B, the first signs of plastic deformation were measured, but fracture occurred after only small strains; in region C, extensive plastic deformation was measured and large plastic strains preceded fracture.

An insight into the mechanism(s) of fracture might well be obtained by a study of the fracture surface. The recently installed scanning electron microscope is most suitable for such an examination, since its depth of focus and the ease of specimen preparation are both far superior to electron-microscope techniques. Preliminary pictures of representative areas of samples from the three regions are presented in Fig. III.B.14. Only a qualitative discussion can be presented at this time. The differences in surface appearance are apparent.

The fracture in region A is featureless, except for pores and cracks, which indicates a brittle, trans-granular type of fracture. In contrast, in region C, the fracture occurred along grain boundaries, i.e., intergranular type, and was preceded by extensive grain-boundary shearing, as is evidenced by the smooth, rounded grain boundaries. A mixed type of fracture was observed in region B; the

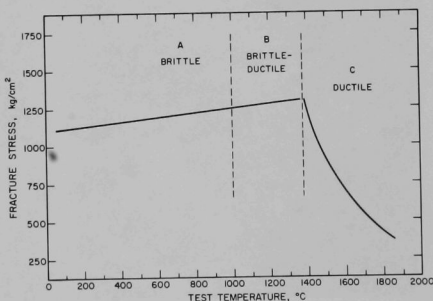
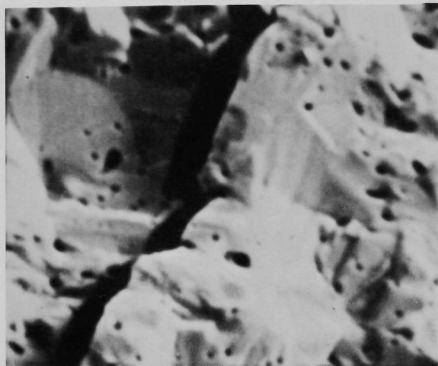


Fig. III.B.13. Temperature Dependence of Fracture Stress

\*Nadai, A., *Theory of the Flow and Fracture of Solids*, McGraw-Hill Book Company, New York (1950), p. 353.

intergranular area is marked by a grain-boundary sharpness, which suggests little or no grain-boundary sliding prior to fracture. This agrees with the small observed plastic strain.



(a) Region A--500°C, 0.092/hr



(b) Region B--1250°C, 0.092/hr



(c) Region C--1600°C, 0.092/hr

Fig. III.B.14

Fracture Surfaces Obtained by Scanning  
Electron Microscope. Mag. 2000X.

In summary, these preliminary results illustrate the potential of the scanning electron microscope in a study of fracture mechanisms.

## C. Engineering Development--Research and Development

### 1. Instrumentation and Control (T. P. Mulcahey)

#### a. Boiling Detector (T. T. Anderson)

Last Reported: ANL-7655, pp. 108-109 (Dec 1969).

#### (i) Acoustic Method

#### (a) Irradiation and Resistance Tests of Piezoelectric and Insulator Materials (S. L. Halverson, A. P. Gavin, and T. T. Anderson)

Evaluation of lithium niobate as a high-temperature, radiation-tolerant piezoelectric transducer material\* has led to the design of several transducer test assemblies, the latest of which is designated H-5.

Based upon experience with earlier crystal-holding devices, the H-5 assembly incorporates, as a new feature, optically flat stainless steel surfaces in contact with the lithium niobate crystal to minimize cracking. It is designed to facilitate testing the crystal at temperatures up to 1200°F in a gamma-radiation environment. To achieve these temperatures, the assembly is installed in a low-gamma-attenuation furnace (see Progress Report for October 1969, ANL-7632, p. 114). Acoustic excitation is supplied by an ultrasonic transducer shielded from gamma rays and located outside the furnace. Electrical output from the crystal is conducted by a MgO-insulated cable to instrumentation outside the radiation environment.

Preliminary furnace test of the assembly between room temperature and 1050°F showed no degradation in acoustic response or electrical properties of the lithium niobate crystal. As expected, the only changes were shifts in modal frequencies due to changes in applied pressure. The mechanical quality factor  $Q_m$  of the crystal was constant, of the order of  $10^3$ , in contrast to much lower pressure-dependent values reported for earlier holders. A possible explanation for the marked change is that surface irregularities assist in dissipating the acoustic energy, thereby reducing  $Q_m$ . Subsequent disassembly revealed slight chipping of crystal edges, but no internal cracking as had been experienced with a previous holder without optical flats.

The furnace, H-5 assembly, and same lithium niobate crystal were then reassembled and placed in the center of a cylindrical

---

\*Primak, W., Anderson, T. T., and Halverson, S. L., Radiation Damage in Lithium Niobate (Abstract), Bull. Am. Phys. Soc. 15(1), 52 (1970).

array of cobalt-60 rods in the Chemistry Division Gamma Facility. An equilibrium crystal temperature of 540°F was achieved, without auxiliary heating. The crystal was irradiated for 117 hr at this temperature and removed for examination. The only change in appearance of the crystal was a slight brownish discoloration in a mottled pattern, which appeared to be a surface condition.

Before resumption of the test, a cobalt-glass dosimeter was irradiated at the crystal location in the furnace. Dosimeter temperature was monitored to make certain that the glass did not heat up sufficiently to anneal out the discoloration. Based on standard procedure for color density, the dose rate was  $1.75 \times 10^7$  rad/hr.

The lithium niobate crystal was reinserted in the holder and irradiated for ~120 hr at ~1000°F maintained by combined gamma and electrical heating. During this period, slight degradation of acoustic output occurred. Shift of antiresonance frequency with temperature agreed closely with results of other investigators.\* Upon cooling after the test, a definite shift of antiresonance frequency was observed.

Subsequent examination of the crystal revealed that the upper face of the crystal had become bonded to the stainless steel over approximately 20% of the contact area and had broken away from the remainder of the crystal. A reaction between the stainless steel of the contact disk and the crystal was clearly evident; this reaction may have been aggravated by a 25-VDC potential applied to the crystal overnight during resistivity monitoring.

From these tests, we conclude that lithium niobate will function effectively as a transducer element in a 1000°F,  $1.75 \times 10^7$ -rad/hr environment, provided suitable precautions are taken to protect the crystal from stainless steel interfaces, and expertise is used in matching crystal-to-metal surfaces to minimize shear stresses.

(b) Development of High-temperature Detector  
(T. T. Anderson and A. P. Gavin)

Specifications have been prepared for commercial procurement of a high-temperature acoustic sensor, using piezoelectric material and 30-ft-long integral-sheathed leads for service when immersed in sodium.

In support of ANL fabrication of a clamped-construction sensor, the services of O. E. Mattiat\*\* were obtained for the design and

---

\*Fukumoto, A., and Watanabe, A., Temperature Dependence of Resonant Frequencies of LiNbO<sub>3</sub> Plate Resonators, Proc. IEEE 56(10), 1751 (Oct 1968).

\*\*Consultant, Aquasonics Inc., Portsmouth, Rhode Island.

analysis aspects of acoustic sensors. On the basis of his recommendations, two prototype sensors have been fabricated, using the fluid-backed, two-crystal approach for broad frequency response from near DC. Briefly, each prototype consists of a stack of components mounted in a brass housing, from which issues a vacuum line to provide clamping action, and an MgO-insulated signal cable. Construction of the assembly is such that the lithium niobate crystals could be completely isolated, electrically, from the housing, if desired. When the first assembly was evacuated, a strong signal was noted with the high-temperature cable attached directly to oscilloscope input. Immersion in water revealed a leak at the O-ring seals. This leakage problem has been eliminated in the second assembly, and tests are being set up for pulsed-wave calibration in a water tank. Also, an all-stainless steel model is being fabricated to determine construction problem areas.

(c) Tests of High-temperature Detectors in Water, Furnace, and Sodium (T. T. Anderson)

Absolute calibrations of acoustic sensors in small liquid volumes are complicated by tank-wall reflections of incident pressure waves. To circumvent this difficulty, particularly in sodium systems, a pulsed sine-wave hydrophone calibration system has been assembled. All electronic components have been procured and after some improvements by the vendor to meet specifications, the system is now operational.

b. Flow Monitor (T. T. Anderson)

Last Reported: ANL-7581, p. 102 (June 1969).

(i) Two-thermocouple Method (A. E. Knox and C. W. Michels)

(a) Temperature Variation of Coolant Sodium at the Outlet of the EBR-II Instrumented Subassembly. Various aspects of the two-thermocouple (transit-time) method of flow measurement are being investigated, using data obtained from instrumented subassemblies installed in EBR-II. Noise-analysis techniques will be used to measure the transit time of small variations of sodium temperature in instrumented subassembly channels.

Data have been taken from four thermocouples and the flowmeter in the Test II (XX01) EBR-II Instrumented Subassembly. Signals from outlet thermocouple No. 5 (OTC 5), inlet thermocouple No. 4 (ITC 4), outlet thermocouple No. 14 (OTC 14), and spacer-wire thermocouple No. 17 (SWTC 17) were recorded in the frequency range from 0 to 100 Hz, with most of the steady-state component removed to allow maximum amplification of the data. OTC 5 and ITC 4 are in the same channel; OTC 14 and SWTC 17 are in another channel, with expected channel transit-times of 0.346 and 0.224 sec, respectively (for an assumed subassembly flow of 29.6 gpm).

Data recorded during reactor conditions of zero flow to full flow and from zero power to 50 MW are being analyzed to determine feasibility of transit-time flow measurement, using the normal coolant temperature variation in an operating LMFBR.

## 2. Heat Transfer and Fluid Flow (M. Petrick)

### a. LMFBR Burnout Limitations (R. J. Schiltz and R. Rohde)

Last Reported: ANL-7661, p. 110 (Jan 1970).

(i) Preparation of Apparatus. The preheater and five of the six  $1\frac{1}{2}$ -in. valves have been welded into the main loop. The electromagnetic, helical induction pump coil has been assembled, insulated, instrumented with thermocouples, and the pump is ready to be welded into the main loop. The main  $1\frac{1}{2}$ -in.-loop piping is 75% complete.

Thermocouple instrumentation for the heat exchanger has been connected to the thermocouple junction box for the loop. The control panel for the variable autotransformers for the electrical trace-heating system has been prepared for mounting of the autotransformers.

Connection of the heat-exchanger resistance heaters into three groups of five heaters has been completed preparatory to installation of three-phase, electric power.

### b. Nonboiling Transient Heat Transfer (R. P. Stein)

Last Reported: ANL-7661, pp. 110-112 (Jan 1970).

(i) Analyses of Heat-flux Transients. Construction of the test section and modifications of the existing flow loop to be used for the transient experiments (see Progress Report for December 1969, ANL-7655, p. 110) have been postponed until FY 1971 because of budgetary revisions. However, the remaining design work is being completed.

An available computer program\* which solves the problem of transient heat transfer for a fluid flowing between heat-generating parallel plates has been tested successfully and revised slightly. The basic program uses finite differences to solve the associated energy equations for both the plates and the fluid; profiles of turbulent fluid velocity and eddy diffusivities are accounted for. It has been revised slightly to handle specified, but arbitrary, wall heat fluxes into the fluid and thus simplify

---

\*Gopalakrishnan, A., Transient Heat Transfer Performance of a Reactor Coolant Channel During Accidental Power Excursions, Ph.D. Thesis, University of California, Berkeley (1969).



comparisons of predictions of proposed transient engineering relationships (see Progress Report for August 1969, ANL-7606, p. 105) with more exact predictions of the reference program. Attempts are being made to incorporate these engineering relationships in fast reactor codes like the SAS1A; as yet these attempts have not been successful.

c. Liquid-metal Heat Transfer in Pin Bundles (T. Ginsberg)

Last Reported: ANL-7655, pp. 111-113 (Dec 1969).

A literature review of liquid-metal heat transfer in pin bundles, including current and planned investigations at other AEC Laboratories, is nearly complete. Recommendations for ANL participation in this area of heat transfer are being prepared.

d. Electron-Bombardment-Heater Development (R. D. Carlson)

Last Reported: ANL-7661, p. 112 (Jan 1970).

(i) Preparation and Test of Single Pin (1/4 in. OD x 24 in.).

Work on these tests has been delayed because several cathode materials ordered from General Electric have not been received because of the strike.

(ii) Preparation of Single Pin (1/4 in. OD x 36 in.). Apparatus for testing this pin in sodium at 1200°F and heat fluxes up to  $5 \times 10^6$  Btu/(hr)(ft<sup>2</sup>) has been completed, and is being assembled in the vacuum chamber.

(iii) Preparation of 7-pin Clusters (1/4 in. OD x 36 in.).

Preparation of this 7-pin cluster has been held at the design stage pending the results of tests with the single pin (1/4-in. OD x 36 in.), which will begin soon.

(iv) Preparation of Tubular Heaters for Burnout and Nonboiling Transient Tests. The tubular heater for the transient test loop is 90% complete. Remaining tasks include final cleaning of the assembly and installation of 20 filaments.

3. Engineering Mechanics (G. S. Rosenberg)

a. Advanced Thermoelasticity (R. A. Valentin)

Last Reported: ANL-7655, p. 115 (Dec 1969).

(i) Solution of End-effect Problems Involving Nonplane Stress Fields in Short Cylinders and Contact Stresses between Cladding and Fuel. Mathematical analysis of the symmetric deformation of a clad, finite cylinder with interface boundary conditions of zero shear has been completed.



Numerical results for the limiting cases of a very weak cladding and a rigid cladding agree with previous solutions. However, numerical difficulties with intermediate cases have resulted in a slight reformulation of the problem. Needed changes in the analysis have been initiated.

(ii) Techniques of Numerical Approximation. A general-purpose finite-element code has been used to analyze certain aspects of the perfectly bonded clad cylinder. The results indicate that such analyses are of sufficient accuracy to justify a redirection of the analytical effort on those boundary conditions for which general-purpose numerical methods are not feasible (e.g., the case of zero interface shear).

b. Structural Dynamics Studies--Structure-Fluid Dynamics  
(M. W. Wambsganss, Jr.)

(i) Preparation of Two Structural-dynamics Test Loops  
(B. L. Boers and P. L. Zaleski)

Last Reported: ANL-7661, p. 115 (Jan 1970).

Start-up procedures for the large test loop have been written. Start-up and preliminary check-out tests are pending approval of the procedures.

A flowtest was performed to determine the characteristics of the pressure field in the test section of the small test loop prior to installation of the upstream and downstream acoustic filter systems. The data were recorded on magnetic tape, and will be used to evaluate the effectiveness of the filters in reducing acoustic disturbances induced by loop components and other sources. The upstream filter system is being installed in the loop.

(ii) Mathematical Modeling of Parallel-flow-induced Vibration  
(S. S. Chen)

Last Reported: ANL-7661, pp. 114-115 (Jan 1970).

An analytical expression for the root-mean-square (rms) values of the displacement of a simply supported rod in parallel flow was obtained based on the following observations:

(1) First bending-mode response is dominant (see Progress Report for November 1969, ANL-7640, pp. 120-123).

(2) Effective ranges of Strouhal numbers for planned parallel-flow-induced vibration tests and typical reactor conditions are

$0.02 < \nu < 0.52$ ,  $10 < \gamma < 180$ , and  $0.004 < S < 0.25$ . Here,  $\nu = 0.275(\omega D/V_c)$ ,  $\gamma = \ell \omega/V_c$ , and  $S = \omega \delta^*/V$ , where  $\omega$  is the frequency,  $D$  is the rod diameter,  $V_c$  is the convection velocity,  $\ell$  is the rod length,  $\delta^*$  is the displacement thickness of the boundary layer, and  $V$  is the mean axial flow velocity.

(3) The power-spectral density of the turbulent-boundary-layer wall pressure is approximated by

$$\Phi_{pp}(\omega) = k_1(\omega \delta^*/V)^{-k_2}(\rho^2 V^3 \delta^*), \quad (1)$$

where  $\rho$  is the fluid density, and  $k_1$  and  $k_2$  are constants which depend on the particular system flow conditions.

The resulting expression for the rms displacement is

$$\begin{aligned} \bar{y}(x) = & (1.225)(10^{-3})[(k_1)^{1/2}/\Omega_1^{1.5+0.5k_2}] G(k_2, \xi) \sin [(\pi x)/\ell] \\ & D^{-0.5} \ell^4 (M+m)^{-[(1-k_2)/2]} M^{[(5-k_2)/4]} (EI)^{-[(3+k_2)/4]} V^{[(3+k_2)/2]} \\ & \delta^* [(1-k_2)/2], \end{aligned} \quad (2)$$

where

$$\Omega_1^2 = \pi^2 \left\{ [1 - (\ell^2/\pi^2 EI)] \left\{ T - MV^2 [1 - (\epsilon C_T/4)] \right\} \right\},$$

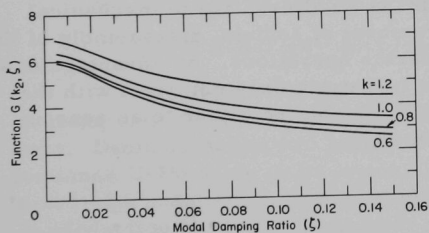


Fig. III.C.1. Dependence of Function  $G(k_2, \xi)$  on  $k_2$  and Modal Damping Ratio

$G(k_2, \xi)$  is a function depending on  $k_2$  and modal damping ratio  $\xi$  (see Fig. III.C.1),  $m$  and  $M$  are the mass and added mass per unit length of the rod,  $EI$  is the flexural rigidity of the rod,  $T$  is the initial axial tension in the rod,  $\epsilon$  is the  $\ell/D$  ratio, and  $C_T$  is the drag coefficient. For known system properties, the rms displacement is easily calculated.

In typical reactor systems, the coolant velocity is relatively low compared to the critical flow velocity; therefore the frequency  $\Omega_1$  is a weak function of  $V$ . In general,  $k_2$  varies from 0 to 1.0. With these observations, Eq. (2) can be expressed

$$\bar{y} \propto D^{\alpha_1} \ell^{\alpha_2} V^{\alpha_3} (EI)^{\alpha_4}, \quad (3)$$

where

$$\alpha_1 = 1.0-1.5;$$

$$\alpha_2 = 4.0;$$

$$\alpha_3 = 1.5-2.0;$$

$$\alpha_4 = -0.75-1.0.$$

Equation (3) is reasonably well related to Paidoussis' empirical equation

$$\bar{y} \propto D^{\alpha_1} l^{3.5} V^{1.6} (EI)^{-0.8}, \quad (4)$$

where in the two experimental correlations reported\*  $\alpha_1 = 0.35$  and  $1.0$ . Since development of Eq. (4) is based on experimental results and Eq. (3) represents analytical reduction of a mathematical model, the general agreement between both equations supports the validity of the mathematical model.

#### D. Chemistry and Chemical Separations

##### 1. Fuel Cycle Technology--Research and Development

###### a. Molten Metal Decladding (R. D. Pierce)

Last Reported: ANL-7655, pp. 116-117 (Dec 1969).

Decladding with molten metal is an alternative to mechanical decladding schemes,\*\* which require removal of sodium, disassembly of the fuel assembly, and fuel chopping as separate operations. An advantage of a molten metal decladding step is that the fuel oxide does not react with the decladding chemicals and, once separated, can be fed either to an aqueous dissolution step or to another interfacing step.

###### (i) Engineering Development

(a) Plutonium and Uranium Recovery. The LiF-35 mol % NaF-10 mol % CaF<sub>2</sub> eutectic is under consideration as a cover salt for a decladding process in which stainless steel (or Zircaloy) cladding is dissolved in liquid zinc and the resulting metal solution is then separated from the unreacted oxide fuel. A cover salt would suppress

\*Paidoussis, M. P., An Experimental Study of Vibration of Flexible Cylinders Induced by Nominally Axial Flow, Nucl. Sci. Eng. 35(1), 127-138 (1969).

\*\*Watson, C. E., et al., "Head-End Processing of Spent LMFBR Fuel," in Proceedings of 16th Conference on Remote Systems Technology, pp. 19-38, American Nuclear Society, Hinsdale, Ill. (1969).

vaporization of zinc; also, agitation of the zinc-salt system would cause any fuel fines originally in the zinc to be collected in the salt.

Results have been obtained for an experiment (see ANL-7655) to measure the cosolubility of powdered uranium oxide and plutonium oxide in this fluoride salt. A high-purity  $\text{Al}_2\text{O}_3$  crucible contained in a tantalum secondary crucible was charged with 2.0 kg of the  $\text{LiF-NaF-CaF}_2$  salt, 100 g of powdered  $\text{PuO}_2$ , and 400 g of powdered  $\text{UO}_2$ . The charge was held at  $\sim 800^\circ\text{C}$  for 4 hr with agitation at 300 rpm and for about 16 hr without agitation. After the addition of 6.25 kg of zinc, the  $800^\circ\text{C}$  melt was agitated at 300 rpm for  $4\frac{1}{2}$  hr and at 600 rpm for  $1\frac{1}{2}$  hr.

The rate of dissolution of  $\text{PuO}_2$  powder in the salt was low. Although samples were taken at intervals during the run, it is now believed that the system did not reach equilibrium until the end of the run, when two duplicate salt samples were taken that were found to contain  $\sim 0.4$  wt % dissolved plutonium. This concentration of plutonium in a cover salt is considered satisfactorily low. The plutonium loss per run, however, will be considerably smaller because the cover salt will be reused for many runs. Since this experiment involved finely divided  $\text{PuO}_2$  in an agitated system, whereas plant operation would be with either no agitation or mild agitation and sintered pellets and fragments which will sink through the zinc, the observed plutonium dissolution would probably be negligible in plant operations.

In all salt samples, the uranium concentration was below the detection limit (0.01 wt %).

b. Continuous Conversion of U/Pu Nitrates to Oxides (N. M. Levitz)

Last Reported: ANL-7661, pp. 118-119 (Jan 1970).

Denitration of mixtures of uranium-plutonium nitrate solutions or plutonium nitrate solutions is to be demonstrated in fluidized-bed equipment. Denitration has two potential applications: (1) production of either combined U-Pu oxide or of plutonium oxide that could be mechanically mixed with uranium oxide and fabricated into fast reactor fuel; and (2) production of plutonium in powder form (i.e., oxide) which could be shipped more safely and in smaller volumes than the nitrate solutions that are currently being shipped.

In three laboratory-scale experiments (see ANL-7661), 1.2M uranyl nitrate-0.3M plutonium nitrate-2 to 4M nitric acid solutions were fed dropwise on to a hot surface at approximately 300, 450, and  $600^\circ\text{C}$  to form oxide. Samples were examined to determine whether plutonium was uniformly distributed in the oxide produced at  $450^\circ\text{C}$ . Preliminary data with an electron microprobe indicate that overall homogeneity is good. Preliminary results of autoradiographic examination also indicate uniform plutonium distribution in the oxide powder prepared at  $450^\circ\text{C}$ .

Dissolution of the oxide powder in nitric acid systems is being studied as a method of recycling the denitration product to minimize the plutonium inventory in the glovebox in future larger-scale experiments. Dissolution experiments of a scoping nature were performed on a gram scale with a U-20% Pu oxide produced by dropwise denitration at 300°C. About 95% of the oxide was dissolved by stirring for 2 hr in concentrated  $\text{HNO}_3$  at 95°C to yield a solution approximately 0.35M in heavy metal. Smaller percentages of oxides produced at 450 and 600°C were dissolved in the same time interval. The results for oxide powder prepared at 300°C are encouraging. Future experiments will evaluate dissolution characteristics of the prepared oxides under typical process conditions.

The fluid-bed pilot plant for denitrating solutions of uranium-plutonium nitrates or plutonium nitrate alone is being constructed. A 4-in.-dia plastic fluid-bed column (i.e., a mockup of the denitrator) was constructed to evaluate the denitrator design. Results with an inert fluidized bed suggested a change in the design of the product-withdrawal tube. In work to determine whether an increase in the quantity of  $\text{PuO}_2$  in a process vessel could be measured with external instrumentation, experiments were run with  $\sim 1/2$  to 1 kg  $\text{UO}_2$ -1.78 wt %  $\text{PuO}_2$  and  $\text{UO}_2$ -20 wt %  $\text{PuO}_2$  powder (shielded with  $1/4$ -in. stainless steel to simulate the effect of a vessel wall). A scintillation-type counter fitted with a gamma probe was found to be promising for this application.

c. In-Line Analyses in Fabrication (M. J. Steindler)

Last Reported: ANL-7655, p. 119 (Dec 1969).

The accuracy and precision of analytical methods affect the fraction of acceptable material produced in large-capacity fabrication plants and thus influence the cost of the fabricated fuel. Continuous in-line non-destructive analytical methods capable of determining the physical and chemical properties of FBR fuel are under development.

The determination of the U/Pu ratio in fuel, which will be a part of any conceivable fabrication procedure, is being studied.  $\text{ThO}_2$ - $\text{UO}_2$  is being used as a stand-in for  $\text{UO}_2$ - $\text{PuO}_2$  in evaluating X-ray fluorescence as an in-line analytical method, since the relationship of the appropriate emission peaks for thorium and uranium is similar to that for uranium and plutonium (ANL-7655, p. 119). Powder mixtures containing 10, 20, 30, and 40 wt %  $\text{UO}_2$  and the remainder  $\text{ThO}_2$  have been examined with the X-ray spectrograph. Smooth curves have been obtained that relate line intensity to the concentration of each heavy element. Further, the intensity ratio of the signals for the two heavy elements showed a smooth and rapidly changing variation with  $\text{UO}_2$  content of the mixture in the concentration region of interest (10-40%  $\text{UO}_2$ ). These data indicate that measurement of heavy

element ratios by X-ray fluorescence appears feasible. Future work will be aimed at demonstrating analytical sensitivities which meet existing fuel specifications.

An important property affecting changes in fuel during irradiation is the initial ratio of oxygen to metal (O/M) of the fuel material. The O/M ratio is presently determined by a thermogravimetric method. A method that may be adaptable for in-line use is now being tested for the determination of the O/M ratio. This method depends upon the measurement of lattice parameters of the fuel material by X-ray-diffraction techniques. Information has been obtained on the variation of lattice parameters of single-phase (U,Pu)O<sub>2-x</sub> with variation of the O/M ratio at several plutonium concentrations.

## 2. General Chemistry and Chemical Engineering--Research and Development

### a. Thermophysical Properties

#### (i) Oxygen Gradients, Total Vapor Pressures, and Oxygen Potentials in Reactor Fuels (P. E. Blackburn and A. J. Becker)

Last Reported: ANL-7640, p. 124 (Nov 1969).

Oxygen potentials and total pressures are being measured over (U,Pu)O<sub>2±x</sub> fuel as functions of temperature and composition. These data are required to aid in limiting cladding corrosion, fuel swelling, and fissile element segregation either by fixing initial fuel composition, by adding oxygen buffers, or by other suitable measures. The oxygen potential of the fuel will help to establish the chemical state of fission products, especially those contributing to cladding corrosion or fuel swelling. In the first phase of the program, the pure oxide fuel corresponding to that with zero irradiation will be investigated. These studies will be followed by measurements of the fuel containing fission products.

The data obtained by the transpiration method for calculating oxygen potentials and total pressures over U-Pu-O will be in terms of pressures, temperatures, and weights. At equilibrium, the rate of weight loss can be shown to be constant both for U-O and U-Pu-O provided the sample geometry does not change. Therefore, one criterion for equilibrium is that the weight-loss curve must approach a straight line.

In the series of experiments designed to test the apparatus, attention has been shifted from the hyperstoichiometric two solid-phase U-O system to the single solid phase on either side of O/U = 2. In experiments in which the sample was heated to 1653°K and in which the sample



and argon carrier gas equilibrated, the O/U ratio was 2.165 and oxygen partial pressure was  $3.0 \times 10^{-4}$  atm. The vapor pressure of the uranium-bearing species was calculated to be  $7.6 \times 10^{-6}$  atm. The latter number should be considered tentative. It was found experimentally that when constant oxygen pressure was observed, the rate of weight loss approached a straight line, as predicted.

Work with the U-O system should be completed soon and work with the U-Pu-O system initiated.

(ii) Phase-diagram Studies of the Ternary System U-Pu-O  
(P. E. Blackburn and A. E. Martin)

Last Reported: ANL-7632, pp. 124-125 (Oct 1969).

Oxygen-rich and metal-rich phase boundaries are being determined for the  $(\text{U,Pu})\text{O}_{2\pm x}$  LMFBR fuel. The boundaries are required to establish criteria for initial concentrations of oxygen in the fuel. The boundaries also establish the capacity of the fuel for oxygen. This information is important since oxygen concentrations may change during burnup of the fuel. Data on the ternary system of pure uranium, plutonium, and oxygen will serve as a base line for interpreting the phase diagram of fuel and fission products.

The hypostoichiometric boundary of the fluorite phase,  $(\text{Pu}_y, \text{U}_{1-y})\text{O}_{2\pm x}$ , for  $y = 0.198$  was previously reported in ANL-7632 for the temperature range from about 1860 to 2170°C. The data were obtained from the oxygen analyses of mixed-oxide crucibles that had been equilibrated with liquid plutonium-uranium alloys. An attempt was made to obtain similar data at the higher temperatures of 2207 to 2247°C. The O/M ratios of 1.398 and 1.278, respectively, of the product crucibles were considerably smaller than an extrapolation of the data to lower temperature would have predicted. Metallographic examinations of the product crucibles indicated that, at these higher temperatures, the overall composition was in a three-phase region of the U-Pu-O phase diagram instead of a two-phase region. The third phase, an oxide liquid, which has a lower oxygen concentration than the fluorite phase, had apparently been absorbed into the oxide crucible. Thus, the analyses of the crucibles did not represent the compositions of the solid fluorite phase at the equilibration temperatures, as had been the case at the lower temperatures. Consequently, the highest temperature at which the equilibration technique can be used to establish the hypostoichiometric boundary of the oxide phase with  $y = 0.198$  is approximately 2170°C.

Efforts are being made to prepare sintered mixed-oxide pellets with various  $y$  values, but initially with  $y = 0.198$ . These pellets will have O/M ratios that are stable at room temperature. X-ray-diffraction



and other studies will be carried out with these pellets. For the oxygen-rich range, the pellets are being produced by partial oxidation by air at 1000°C. For the hypostoichiometric region, the pellets are being produced by partial reduction with uranium-plutonium alloys at 2000°C.

Some oxidation tests have been carried out on sintered mixed-oxide pellets of compositions  $y = 0.198, 0.441, 0.643,$  and  $0.804$ , which had initial O/M analyses of 2.00, 1.99, 1.99, and 2.00, respectively. Recorded in Table III.D.1 are the weight increases, in O/M units, following oxidation by flowing dry air. The values in the temperature range 800 to 1200°C are in essential agreement with literature data;\* the values at the lower temperatures represent new data. However, equilibria with the oxygen of the air were probably not reached in the temperature range from 200 to 400°C in spite of the extended periods of oxidation.

TABLE III.D.1. The Oxygen Pickup Resulting from the Air Oxidation of Sintered Mixed-oxide Pellets at Various Temperatures

| Oxidation Conditions |           | Oxygen Increases (in O/M units) at Indicated Pellet Compositions |             |             |             |
|----------------------|-----------|--|-------------|-------------|-------------|
| Temp (°C)            | Time (hr) | $y = 0.198$  | $y = 0.441$ | $y = 0.643$ | $y = 0.804$ |
| 200                  | 146       | 0.01   | 0.00        | 0.00        | 0.00        |
| 300                  | 144       | 0.36   | 0.05        | 0.07        | 0.02        |
| 400                  | 95        | 0.34   | 0.31        | 0.19        | 0.03        |
| 600                  | 71        | 0.49   | 0.27        | 0.21        | 0.09        |
| 800                  | 27.5      | 0.35   | 0.27        | 0.18        | 0.07        |
| 1000                 | 21.5      | 0.36   | 0.26        | 0.17        | 0.08        |
| 1200                 | 23        | 0.54   | 0.30        | 0.18        | 0.10        |

\*Brett, N. H., and Fox, A. C., *J. Inorg. Nucl. Chem.* 28, 1191 (1966); Sari, C., Benedict, U., and Blank, H., *Thermodynamics of Nuclear Materials*, IAEA, Vienna (1967), p. 587.

## PUBLICATIONS

A Model for Void Formation in Metals Irradiated in a Fast-Neutron Environment

S. D. Harkness and C. Y. Li

Proc. IAEA Symp. on Radiation Damage in Reactor Materials, Vienna, June 2-6, 1969. Int. Atomic Energy Agency, Vienna, 1969, Vol. II, pp. 189-213

The Ternary System Copper-Magnesium-Zinc

K. M. Myles

J. Less-Common Metals 20, 149-154 (February 1970)

Liquidus and Eutectic Phase Equilibria in the Systems  $\text{CaI}_2$ - $\text{CaCl}_2$ ,  $\text{CaI}_2$ - $\text{CaF}_2$ , and  $\text{CaI}_2$ - $\text{MgCl}_2$

R. A. Sharma

High Temp. Sci. 1(4), 423-429 (1969)

The Influence of Local Thermal Stresses on Pore Deformation and Migration in Ceramic Fuel Elements

R. W. Weeks and C. Y. Li

J. Nucl. Mater. 33(3), 318-319 (1969)

Analysis of Bubble Release from Dislocations in Nuclear Fuels

R. W. Weeks and R. O. Scattergood

J. Nucl. Mater. 33(3), 333-336 (1969)

The EBR-II Skull Reclamation Process. Part IV. Pilot-plant Development

I. O. Winsch, R. D. Pierce, D. E. Grosvenor, L. Burris, Jr.,

T. F. Cannon, P. J. Mack, K. Nishio, and K. R. Tobias

ANL-7614 (September 1969)

Foreseeable Application of  $^{252}\text{Cf}$  to Neutron Radiography

J. P. Barton

Isotopes Radiat. Technol. 7(3), 285-291 (Spring 1970)

Argonne Code Center: Compilation of Program Abstracts

M. K. Butler, Marianne Legan, L. Ranzini, and William J. Snow

ANL-7411 Supplement 3 (October 1969)

## IV. NUCLEAR SAFETY RESEARCH AND DEVELOPMENT

### A. LMFBR Safety--Research and Development

#### 1. Reactor Control and Stability (W. C. Lipinski)

##### a. Transfer-function Techniques to Measure Large Fast Reactor Stability (L. J. Habegger)

Last Reported: ANL-7640, pp. 128-129 (Nov 1969).

A computer code has been written for solving one-dimensional, nonlinear, space-time equations. The forms of equations to which the code is applicable represent models of power reactors that include coupling of space-dependent reactor-power densities with various nonlinear feedbacks, such as feedback from fuel and coolant temperatures. The intended applications of the code to the current LMFBR control and stability program are twofold:

1. In the analysis of transfer-function techniques to measure large fast reactor stability, the code will be used in conjunction with Galerkin's method\* (see Progress Report for May 1968, ANL-7457, pp. 137-138) for computing space-dependent transfer-functions for various source-detector configurations. Galerkin's procedure is limited to linear systems.

2. The code can be used for the verification of theoretical stability domains derived for nonlinear reactor systems (see Progress Report for December 1967, ANL-7403, p. 147).

The computational procedure used in the code is based on a straightforward extension of the quasi-linearization procedure for solving steady-state nonlinear reactor equations (see Progress Report for June 1969, ANL-7581, pp. 118-119). The form of equations solved is

$$\frac{1}{v} \frac{\partial \phi}{\partial t} = \frac{\partial}{\partial x} \left[ D(x,t) \frac{\partial \phi}{\partial x} \right] + A(x,t)\phi + \lambda(x)C + S_1; \quad (1)$$

$$\frac{\partial C}{\partial t} = B(x,t)\phi - \lambda(x)C + S_2; \quad (2)$$

$$M \frac{\partial T}{\partial t} = -\frac{\partial T}{\partial x} + \xi(x)\phi + S_3, \quad (3)$$

where each equation may be scalar or vector. Equation (1) represents the equation for neutron flux (or power density). The second equation can be

---

\*Kantorovich, L. V., and Kryloff, V. I., Approximate Methods of Higher Analysis, Interscience, New York (1959).

associated with concentrations of delayed-neutron precursors and/or other feedback variables. The variable  $T$  in Eq. (3) represents coolant temperature. The functions  $S_i$  are arbitrary forcing functions and/or nonlinear functions of the various variables. Appropriate boundary conditions must also be given.

Using operator notation, the above equations can be written in the compact form

$$\frac{\partial u}{\partial t} = L(x,t)u + S. \quad (4)$$

The discrete-time approximation is used to give

$$\frac{u_i - u_{i-1}}{t_i - t_{i-1}} = \theta \{L(x,t)u + S\}_{i-1} + (1 - \theta) \{L(x,t) + S\}_i, \quad (5)$$

where the subscript  $i$  represents the time step and  $\theta$  is a constant with  $0 \leq \theta \leq 1$ . Upon starting with known values for  $u$  at  $t_0$ , Eq. (5) is solved at each time step, using the quasi-linearization procedure.

The code is operational except for some necessary minor revisions. Accuracy of the code is being checked by running cases that have known solutions.

## 2. Coolant Dynamics (H. K. Fauske)

### a. Sodium Superheat (R. E. Holtz and R. M. Singer)

Last Reported: ANL-7661, pp. 122-123 (Jan 1970).

#### (i) Boiling from Surface Cavities

##### (a) Out-of-pile Superheat Tests with Sodium from EBR-II.

Fabrication of the shipping cask for the sodium from EBR-II has been completed. The cask is being prepared for shipment to Idaho for filling.

### b. Sodium Expulsion (R. M. Singer and R. E. Holtz)

#### (i) Static Expulsion Tests

##### (a) Analysis of Data and Interpretation in Terms of Physical Models

Last Reported: ANL-7661, p. 123 (Jan 1970).

These tests have been completed. A topical report is being prepared.

(ii) Forced-convection Expulsion Tests

Last Reported: ANL-7661, p. 123 (Jan 1970).

(a) Preparation of Transient Test Loop. The tubular test section has been welded into the system and helium-leakchecked. Safety interlock systems and sensors are being installed.

(b) Modification of Transient Test Loop for 7-Pin Tests

Not previously reported.

Design of an increased-capacity heat exchanger for the 7-pin tests has commenced. The design load for this unit will be 1000 kW in order to accommodate the increased power dissipation required when the test section is expanded from a single pin to seven pins.

c. Liquid-Vapor Dynamics (H. K. Fauske and M. A. Grolmes)(i) Liquid-film Breakup

Not previously reported.

In fast reactor accident analysis concerning the hydrodynamic behavior of the coolant, a slug-type ejection process is considered likely. An important and as yet undefined physical characteristic of this process is the thickness and eventual breakup (or dryout) of the liquid film that remains on the heated channel wall during the ejection process. The characteristics of this film and its behavior must be understood so that proper analytical models can be constructed to determine the time between sodium nucleation (slug formation) and failure of the cladding. The cladding probably will fail immediately after film dryout. To assess the film-dryout time, the film thickness must be known. To date no direct experimental information is available concerning the film thickness in an accelerating system such as that involved in superheat sodium-slug ejection. To this end, experiments have been initiated in which film thickness will be measured directly in the slug expulsion of superheated Freon-11 in a uniform-diameter precision-bore glass tube. Preliminary experiments indicate that film thickness can be measured directly by measuring the motion of the vapor slug and the upper free surface. These initial experiments will be refined and extended to more complex geometries and heated sections, and then will be compared to analytical models currently being formulated.

### 3. Violent Boiling (R. O. Ivins)

#### a. Violent Boiling with Molten Fuel and Sodium (D. R. Armstrong)

##### (i) Violent Boiling and Pressure Generation upon Contact of Molten Materials

##### (a) Pressure-generation Experiments by Dropping Molten Material into Coolant

Last Reported: ANL-7640, pp. 136-137 (Nov 1969).

The first experiment involving the dropping of molten  $\text{UO}_2$  into liquid sodium has been completed. For this experiment, 33.7 g of  $\text{UO}_2$  was heated to  $2940^\circ\text{C}$  in a tungsten crucible and dropped into  $230\text{ cm}^3$  sodium at  $200^\circ\text{C}$  (as shown in Fig. IV.A.1). Only 8.8 g of  $\text{UO}_2$  fell into the sodium before the  $\text{UO}_2$  remaining in the crucible froze. Therefore, the temperature of the  $\text{UO}_2$  contacting the sodium ranged from  $2940^\circ\text{C}$  at the start of the pour to  $2840^\circ\text{C}$  at the end. Continuous pressure measurements were obtained from transducers at the bottom of the sodium pot and in the gas space above the sodium. High-speed motion pictures were also taken of the event.

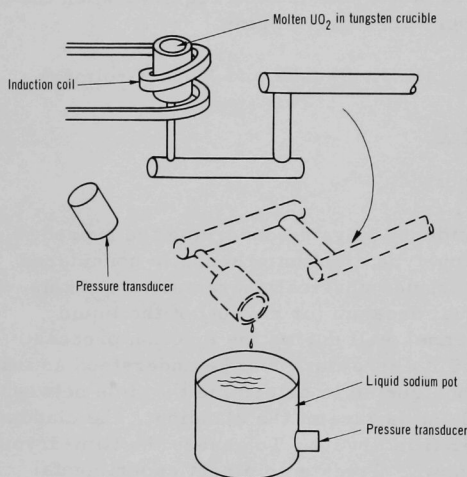


Fig. IV.A.1. Procedure for Pouring Inductively Melted  $\text{UO}_2$  into Molten Sodium

with cusped peaks and rounded minima. The highest pressure peak recorded had an amplitude of 81 psi and a half-width of 1 msec.

Except for two small fragments, all the  $\text{UO}_2$  (8.8 g) that had been dropped was found in the sodium pot after the experiment. As collected, the  $\text{UO}_2$  residue consisted of a few ( $\sim 10$ ) pieces that appeared to be quenched, unfragmented drops that accounted for approximately 60% of the  $\text{UO}_2$  dropped. The remainder of the sample was fragmented particles with a maximum size of 1 mm.

Four separate events can be identified on the film. First, a single drop of  $\text{UO}_2$  fell into the sodium, causing a relatively small eruption and generating enough vapor to obscure the succeeding events partially. About 0.1 sec later, a second, more violent, eruption occurred and expelled two small  $\text{UO}_2$  fragments. A third eruption, similar in magnitude to the second, occurred 0.1 sec later. About 0.3 sec after the third event, a thin stream of  $\text{UO}_2$  entered the sodium, causing a small eruption similar to the first.

Sufficient detail was obtained in the film to allow order-of-magnitude estimates to be made of the viscosity and surface tension of molten  $\text{UO}_2$  (10 cp for the viscosity and 1000 dynes/cm for the surface tension).

Additional experiments duplicating the first, but with improvements in instrumentation and procedure, are planned.

## B. Engineered Safety Features--Safety Features Technology-- Research and Development--Containment

### 1. Hydrodynamic Response to High-Energy Excursion (Y. W. Chang)

Last Reported: ANL-7640, pp. 138-140 (Nov 1969).

#### a. Automatic Rezoning of Code to Extend Excursion Treatment into Sodium-momentum Domain

The two methods developed as an intermediate step to extend the computation time (see ANL-7640, p. 139) have been studied. The single-line-vessel method works very satisfactorily. It eliminates the zone deformation at the steel and sodium interfaces, and, thus, permits the computation to be continued for a longer time. However, the nearest-neighbor-hydrodynamics method fails to perform its function. Numerical instability occurs at about 50 cycles of computation; the method is under further study.

As a first step for rezoning, the types of zone deformations that will be considered in the rezoning code must be defined. In two-dimensional Lagrangian hydrodynamics analysis, a quadrilateral can be deformed into either (1) a normal mesh, if all included interior angles are less than  $180^\circ$ , (2) a reentrant mesh, if one included interior angle exceeds  $180^\circ$ , (3) a schizoid mesh, if one mesh point crosses an opposite side and the mesh takes the form of two triangles (one of which has a negative area), or (4) an inverted mesh; if the deformation proceeds far enough, the net area of the mesh becomes negative. Since the rezoning code is used to prevent severe zone distortions, only the first two kinds of zone distortions will be considered in the rezoning code.



The rezoning code, divided into four parts, is being programmed. The first part of the code deals with quantities associated with new zones; the code will divide the region to be rezoned into new grids according to the instructions and provide storages for quantities that will be furnished later by the searching routine. The second part deals with quantities related to the deformed zones and furnished by the hydrodynamics code. In the third part, a searching routine, the deformed zone will be divided into 64 sub-quadrilaterals; the area, centroid, mass, energy, etc. of each subquadrilateral will be computed, then stored in the proper storage locations provided for new zones via searching routine. The fourth part of the code is an averaging routine; the mass and energy will be conserved in the averaging process.

b. Insertion of Heat Transfer into Codes

Not previously reported.

As the analysis of a postburst accident proceeds to longer times, heat-transfer effects become important. In the case of a gaseous core, for example, there would be a rapid energy exchange at the boundary between the "fire ball" and the surroundings. This would cause vaporization of the materials in contact with the "fire ball," especially sodium, and could result in a pressurization of the system that could cause failure of the primary containment after the initial shock wave passes. The process of energy exchange between the "fire ball" and its environs is undefined because of a lack of knowledge of the various heat-transfer properties. Elsewhere in the system, however, it should be possible to include convection and conduction effects. Rezoning and/or change of the coordinate system from Lagrangian to Eulerian will pose some difficulty in defining the boundaries between materials.

c. Transformation of Code Coordinates from Lagrangian to Eulerian Systems

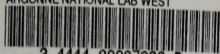
Last Reported: ANL-7618, p. 139 (Sept 1969).

The TRANSF computer code was used to make available the transformation of the Lagrangian solution at a given time as input to the Eulerian-coordinate solution. Although some revisions were made on the TRANSF code for the sake of efficiency, most of the effort was devoted to development of the Eulerian code.

A basic outline of the Eulerian code has been written and is being debugged. The code was named REXCO-P, to make reference to REXCO-H, the parent Lagrangian code. Guidelines used in writing the code were: (1) utilize as much as possible the outline provided for the



ARGONNE NATIONAL LAB WEST



3 4444 00007933 5

X

